RESEARCH ARTICLE

CrossMark

The Rare Earth Elements Potential of Greek Bauxite Active Mines in the Light of a Sustainable REE Demand

Platon N. Gamaletsos[1] · Athanasios Godelitsas[2] · Anestis Filippidis[3] · Yiannis Pontikes[4]

Abstract

More recent data of Greek bauxites from the Parnassos-Ghiona active mines prove that rare earth elements (REEs) occur mainly in the form of authigenic/diagenetic $LREE^{3+}$ carbonate and phosphate minerals (bastnäsite/parisite group and florencite). Bulk geochemistry of representative samples, from underground mines and open pits, showed an increased content in LREE (ΣLREE—from La to Gd—varying between 106 and 913 ppm; avg. ΣLREE = 321 ppm; $n = 17$), and lower HREE (ΣHREE—from Tb to Lu including Y—varying between 45 and 179 ppm; avg. ΣHREE = 95; $n = 17$). The overall REE concentration (ΣREE + Y+Sc) varies from 192 to 1109 ppm (avg. 463 ppm; $n = 17$). The most abundant REE is Ce (min: 67 ppm; max: 655 ppm; avg. 193 ppm; $n = 17$), exhibiting in general a positive geochemical anomaly (avg. Ce/Ce* -Ce^A-: 2.6), identical to the case of marine Fe–Mn-crust and terrestrial desert vanish, implying also that Ce^{4+} may exist either in REE-oxides and/or epigenetically sorbed in Fe-oxides. On the other hand, Nd content, which is more interesting for the industry, is lower (avg. 41 ppm; $n = 17$). The concentration of REEs is much higher in Fe-rich (red) bauxite, compared to Fe-depleted (white) bauxite (avg. ΣREE + Y+Sc = 569 ppm and 268 ppm, respectively). The new data presented herein show a rather lower REE potential of Parnassos-Ghiona bauxites, compared to previous literature, but similar values compared to karst-type bauxites of the globe. Although their REE concentration is higher compared to that of various geochemical reference materials (i.e., positive REE geochemical anomalies in comparison with chondrites, UCC, PAAS, NASC, and ES), it is vitally lower compared to REE resources being mined, such as REE–Fe–Nb–Th deposits. A trend similar to REE geochemical trend also stands for most of the trace elements that are present in Greek bauxites—mainly HFSE—except for LILE. Besides, Greek bauxite metallurgical residue's (red mud) REE content seems to be remarkably increased by almost two times compared to that of the Parnassos-Ghiona bauxite parent material. Scandium is another critical element. In the studied bauxites, it varies from 29 to 73 ppm (avg. 47 ppm; $n = 17$); it is typical for the Mediterranean and EU bauxites and laterites, but much lower compared to the exploitable Australian laterites. The Fe-rich samples contain higher concentrations of Sc compared to Fe-depleted (avg. 54 and 33 ppm, respectively). This means that common red Greek bauxite is rather more exploitable, with regard to Sc (and the rest REE), but not the white one (which is of high quality in terms of Al). Bulk geochemistry indicates that Sc is correlated to Fe but not to Zr, while microscale observations demonstrated the presence of fine-grained scandian-zircons. This is in line with a very recent study proving that Sc is mainly present in Fe-oxide minerals (mainly hematite and goethite) and zircons. Bulk geochemical Fe–Pb and Fe–As positive correlations are also verified among the associated trace elements. Finally, the investigation of the REE vertical distribution in a characteristic deposit of the B3 horizon (i.e., Pera Lakkos mine case

✉ Platon N. Gamaletsos
plagka@dtu.dk

[1] Center for Electron Nanoscopy, Technical University of Denmark, 2800 Kongens Lyngby, Denmark

[2] Department of Geology and Geoenvironment, National and Kapodistrian University of Athens, Zografou Campus, 15784 Athens, Greece

[3] Department of Geology, Aristotle University of Thessaloniki, 54124 Thessaloniki, Greece

[4] Department of Materials Engineering, KU Leuven, Kasteelpark Arenberg 44, 3001 Leuven, Belgium

 Springer

study), showed that the REE concentration is increased in the Fe-rich domain (lying above the footwall limestone), as well as in the coal layer interstratified between the Fe-depleted domain and the hanging wall limestone. However, it is revealed that the Ce/Ce* (Ce^A) is increased in the coal layer and is raised to the uppermost Fe-depleted domain, but not the lowermost Fe-rich bauxite domain. This might be attributed to the $Ce^{3+} \leftrightarrow Ce^{4+}$ and the LREE re-mobilization during the supergene/epigenetic processes.

Introduction

The research for new resources with substantial levels of Rare Earth Elements/REEs (i.e., REE group comprises of the 15 lanthanide elements including Sc and Y) is being set as high priority in the scientific field of the world and, especially, the European Union (EU), due to their exceptional high demand in industry and technology (e.g., [1–6 and references therein]). REEs are considered to be strategic metals [7] having a wide range of technological applications, such as REE (mainly Nd) in FeB magnets—increasingly being integrated into new technological applications (e.g., high-efficiency generators in wind turbines and motors in hybrid electric vehicles, due to the high demand for green energy)—metal alloys, and catalysts (e.g., [4, 8]).

So far, most of the global resources concern REE-Fe-Nb-Th deposits, ion-adsorption deposits, and placer deposits; all of them are located in Asia—such as the giant Bayan Obo deposit in China—and Russian Federation (e.g., [9–11]). Except for the aforementioned world-class deposits being mined, there is also a high potential concerning future exploration of terrestrial deposits, such as carbonatites and peralkaline to agpaitic rocks in North America, and especially in Nordic Countries (e.g., [12, 13]). A recent discovery of deep-sea rare earth yttrium (REY) containing muds in the Northern Pacific Ocean floor have been proposed as potential new rare earth metal resources [14, 15], whereas their future exploitation remains uncertain due to the obvious high smelting and lifting (mining) cost [15]. Apart from the REE potential of Nordic Countries (mainly Greenland and Sweden) in future exploitation inside the EU, the growing REE demand of European high-tech industry raises additional needs for alternative mineral resources, in which REE can be exploited as byproducts. This is fortified by the relative absence of actively mined REE deposits in the EU that signifies the supply risk of REE. The latter is magnified by the Chinese rare-earth export restrictions causing significant supply risks outside China [16]. Thus, a critical question is now posed if REE supplies will be able to meet REE demands in the EU presently securing a sustainable, reliable, and unhindered supply of these critical (clean)-technology strategic metals to many economies. As a result, in Europe an ongoing research regarding harvesting REEs from the existing base metal ores and mines is now of utmost importance for the mining/metallurgical industry, while new significant REE-containing promising deposits are revealed (e.g., [12, 17, 18]). To this trajectory, residual Al- and Ni-deposits, i.e., bauxites and laterites—located mainly in SE Europe—have been proposed (e.g., [17, 18]). It should be mentioned that, for the time being, only bauxite deposits from Greece, along with those from Hungary (the current study) and Italy (e.g., [19 and references therein]), can be considered as "internal" EU resources, whereas certain bauxite deposits from the Balkan peninsula with REE potential (such as the Nikšić bauxite deposit in Montenegro; the current study; and the literature [20]) are still out of the main EU trade.

Greece is the 12th largest bauxite mine producer worldwide, but also the largest in the EU with an annual production of 1800 thousand metric dry tons in 2017. Nowadays, the Greek bauxite reserves, which could be produced economically, are estimated to be approximately 250,000 thousand metric dry tons [21]. Most of the raw material is processed by the "Aluminium of Greece S.A." at its industrial complex at Aghios Nikolaos (Antikyra, Corinth gulf) for the production of alumina (800,000 metric dry tons in 2017) and metallic aluminum for use in the industry and constructions [21]. According to the U.S. Geological Survey [21], Greece is being considered to be the 16th alumina producer in the globe, and the 4th among the EU member-states. The Greek bauxites are currently mined in the Parnassos-Ghiona area (e.g., [22 and references therein]), where there is also a metallurgical plant for Al metal production, while there is no process in the Greek bauxite industry to extract REEs from the raw Al-ore. Thus, most of REEs are transferred in the bauxite metallurgical residue (the so-called red mud), along with certain actinides, such as Th (e.g., [23]). The exploitation of REEs from red mud is rather challenging, although there is evidence that REEs can be extracted easier directly from the raw Al-ore [23, 24]. Thus, the mineralogy and the geochemistry of REEs in Greek bauxites are rather critical. Previous studies indicated the presence of Th-bearing REE-minerals and detrital zircon grains fundamentally containing REE and actinides [24–31]. A concurrent publication to the current study also revealed that Sc is present in Fe-oxides (mainly hematite and goethite) and zircons [32]. Concerning the bulk REE geochemistry of Parnassos-

Ghiona bauxites, some data have sporadically been reported by previous authors [25, 30–47]. However, the REE geochemistry in Greek bauxites has not been systematically investigated, in comparison to relevant karst-type deposits from the Mediterranean (including Balkans), Irano-Himalayan, and East Asian bauxite belts. Therefore, the purpose of the current study is to demonstrate entirely new results of the Parnassos-Ghiona karst-type bauxite deposits (central Greece) in relation to the existing published data from Greek bauxites, as well as a comprehensive comparison with published data referred to karst-type bauxite deposits from Greece, Bosnia, Montenegro, Hungary, Bulgaria, Croatia, Romania, Italy, Turkey, Iran, and China (referred to Mediterranean, Irano-Himalayan, and East Asian bauxite belts; for the relevant literature, see the "Materials and Methods"). This paper to our knowledge is a first attempt to contribute to the future REE exploration and exploitation from base metal deposits, with an emphasis on the REE-containing bauxites, in the light of the sustainable REE demand in the EU and the globe (e.g., [5, 6 and references therein]). Moreover, it is worthy to mention that—among other REEs—Sc is of special interest due to its several high-tech promising applications, such as solid oxide fuel cells (SOFCs) and in Sc–Al alloys, due to specific qualifications (in aerospace industry and in other applications with high-performance demands, e.g., in 3D printing), as well as in ceramics, electronics, lighting, and TV and computer monitors [48]. According to a latest EU report (December 2017), Sc is among the critical raw materials [4]. This means that it has a high economic impact while also having a high supply risk. In this respect, the geochemical aspects of Sc and Y are also considered in the current study, except for the lanthanides series (La to Lu).

Materials and Methods

Samples and Preparation

This study draws on the REE geochemistry of Greek karst-type bauxites from the Parnassos-Ghiona mining area (central Greece). Even though three bauxite horizons can be distinguished in the Parnassos-Ghiona mining area, from bottom to the top: B1, B2, and B3 (e.g., [49, 50]), current active mining activity is taking place in the B2 and B3 horizons, only. Several abandoned mines without any significant economic importance are located in the lower B1 horizon. B1 was exploited several decades ago. The studied bauxite samples were collected from active underground mining sites and open pits of the three Greek mining companies ("Aluminium of Greece S.A.," and its subsidiary "Delphi-Distomon S.A.," as well as "S&B

Industrial Minerals S.A.," which has been recently consolidated by "Imerys S.A.," and "ELMIN Hellenic Mining Enterprises S.A.," whose bauxite division has been acquired by "Imerys S.A.") exploiting bauxite from the intermediate (B2) and the upper (B3) bauxitic horizons (see Supplementary Material; Fig. S1). The studied bauxite samples concern Fe-rich (i.e., typical low-grade; diasporic and boehmitic; red-brown in color) and Fe-depleted or "bleached" (i.e., high-grade; diasporic; white–gray in color) bauxites. The Fe-rich samples are located in the middle and the lower parts of the B2 and B3 bauxitic horizons, whereas the Fe-depleted samples are derived from the uppermost parts of the B3 bauxitic horizon. For comparison purposes, representative bauxite samples from active mines from Bosnia (Jajce bauxite deposit), Montenegro (Nikšić bauxite deposit), and Hungary (Halimba bauxite deposit), supplied by the "Ajkai Timföldgyár" alumina plant ("MAL Magyar Alumínium Zrt") were additionally investigated (see Supplementary Material; Fig. S2). In the case study of the Pera Lakkos underground mine (see Supplementary Material; Fig. S1), carbonate rock samples originating from the dark-to-black bituminous hanging wall and the ordinary white footwall limestones along with the Fe-rich/sulfide-bearing bauxite, Fe-depleted bauxite, and Fe-rich bauxite samples—which are vertically embedded between the footwall and the hanging wall carbonate platforms of the B3 horizon—were also investigated. Representative samples from a characteristic thin layer of coal [51, 52] interstratified between the dark-to-black bituminous hanging wall limestone and the Fe-depleted bauxite (sum of samples $n = 10$) were collected. In order to discuss the mobility and accumulation of trace elements including REE across and downward the entire Pera Lakkos mine profile, a composite sample of this coal was combusted to get fly ash (in fact to remove the organic part and separate the inorganic constituents) and investigated from a geochemical perspective.

The bauxite samples—used in the current study from Parnassos-Ghiona mines—are composite mining materials, created by following standard mixing procedures and sample splitters, by taking the appropriate number of specimens vertically at mining fronts. Mining companies exploiting industrial minerals, required to be used as commercial products, typically obtain such composite samples. Among a batch of numerous composite bauxite samples obtained from both underground mines and open pits of the companies, in order to explore REE in the current study, six samples were chosen, on the basis of variable REE-contents, from the Fe-depleted stock and, moreover, 11 from the Fe-rich stock (sum of samples $n = 17$). All the samples—both bauxites and limestones—were crushed to appropriate size, and a further portion was sliced by diamond wheel saw (Minitom/Struers) for preparation of polished (embedded into epoxy resin) and thin-

polished sections, and pulverized in agate mortar. Exceptionally, few selected fresh-cracked bauxite specimens—previously checked by stereomicroscope (i.e., bauxite geode)—were chosen to be studied by Scanning Electron Microscopy/SEM. In particular, fresh-surface microareas of the bauxite specimens were additionally examined by SEM for REE-bearing mineral intergrowths and microstructure observation (see text below). In that case, the specimens neither were ground/polished nor were embedded into epoxy resin (fresh-surface microareas). All samples were initially ground and polished properly by means of grinding machine (LaboPol-25/Struers) and polishing system (MultiPrep^{TM} System/Allied) to achieve efficient material removal and minimal surface damage. Silicon carbide (SiC) papers were used for grinding down to 15 μm and furthermore diamond lapping films for polishing down to 1 μm with water as lubricant. In order to minimize contamination due to preparation, all samples were finally bathed in ethanol using ultrasonic bath (model B2510/Branson).

Powder X-Ray Diffraction (PXRD) and Electron Microscopy (SEM–EDS/SEM–WDS)

The bulk mineralogical composition was determined by means of powder X-ray diffraction (PXRD) using a Bruker AXS D8 ADVANCE Diffractometer. Powder XRD patterns were recorded overnight (CuK_α radiation, dwell time of 8 s per 2θ step with a step of 0.02°). The identification of crystalline mineral phases was initially obtained using the database from ICDD (International Centre for Diffraction Data) and the EVA software (BRUKER AXS).

The mineralogy at the microscale was checked by SEM combined with Energy-Dispersive X-ray Spectroscopy (EDS) and Wavelength-Dispersive X-ray Spectroscopy (WDS). Initial SEM–EDS observations were obtained using a Jeol JSM 5600 SEM equipped with an ISIS 300 Oxford EDS detector. Analytical conditions were 20 kV accelerating voltage, 0.5 nA beam current, < 2 μm beam diameter and 20 s dwell time. In the case of the fresh-surface microareas, a dwell time of < 10 s was used to avoid sample damage due to e-beam and sample surface interaction.

In order to conduct qualitative SEM–EDS/SEM–WDS measurements, a FEI Quanta 200 FEG SEM equipped with EDS (Oxford Instruments 80 mm^2 X-Max silicon drift detector, MnK_α resolution at 124 eV) along with a FEI Inspect S equipped with EDS and WDS spectrometers (EDS: Oxford Instruments 50 mm^2 X-Max silicon drift detector, MnK_α resolution at 124 eV; WDS: Oxford Instruments INCA Wave 500, spectral resolution 2 eV) were used. Backscattered Electron Detector (BSED) was also utilized. The qualitative EDS/WDS combined analyses on the bauxite samples were performed at high-vacuum condition (using pressure at 10^{-4} Pa). Besides, the Fe-depleted bauxite samples were studied under low-vacuum condition (using pressure at 50 Pa and accelerating voltage at 15 keV; see text below) in order to avoid charging and potential damage. Fe-depleted samples are porous and charging phenomena easily come up. All bauxite samples were analyzed with an accelerating voltage at 20 kV, with an exception of the Fe-rich samples that were complementary investigated using a 30 kV in order to check the presence of high-X-ray-energy elements, such as YK_α, ZrK_α, ThL_α, and UL_α. All the studied samples were probed using a working distance at 10 mm, a beam current of 10 nA and a beam size of 3–10 μm (because of the small grain size of the REE-minerals) and a defocused beam to minimize any sample damage. In the case of WDS analyses, the counting times for REE were 20–40 s on peak and half of that on its background. Shorter times were used for other elements, whereas the live time of 10–60 s was used for the EDS acquisition. Synthetic oxides and natural minerals were utilized as WDS standards. In particular, calibration standards were Co, Cu, Ti, V, and Cr pure metals for the elements CoK_α, CuK_α, TiK_α, VK_α, and CrK_α, respectively. Moreover, corundum (Al_2O_3) for AlK_α, wollastonite ($CaSiO_3$) for CaK_α and SiK_α, orthoclase variety adular ($KAlSiO_3O_8$) for KK_α, periclase (MgO) for MgK_α, rhodonite ($MnSiO_3$) for MnK_α, hematite (Fe_2O_3) for FeK_α, pentlandite [$(Fe,Ni)_9S_8$] for NiK_α and SK_α, monazite [$(Ce,La,Y,Th)PO_4$] for PK_α, and fluorite (CaF_2) for FK_α; further, synthetic REEs and Y phosphates (i.e., LaP_5O_{14}, CeP_5O_{14}, NdP_5O_{14}, DyP_5O_{14}, and YP_5O_{14}) for LaL_α, CeL_α, NdL_β, DyL_α, and YL_α, respectively, were also used [53]. The acquisitions of EDS and WDS spectra, and their analyses, were performed using the AZtec and the INCA software packages. The microscale study was performed on carbon-coated (20-nm thickness) fresh-surface microareas, polished (embedded in epoxy resin), and polished, thin-section, samples, respectively.

X-Ray Fluorescence Spectrometry (XRF), ICP-Atomic Emission Spectrometry (ICP-OES), and Inductively Coupled Plasma Mass Spectrometry (ICP-MS)

Bulk geochemical analyses of the studied bauxite samples and the limestones from the Parnassos-Ghiona mining area (central Greece) were initially performed by XRF using a Philips (currently Malvern Panalytical) MagiX PRO equipment, with Rh Anode at 3.6 kW, and under experimental conditions presented in Table S1 (see Supplementary Material). Moreover, certain major and trace elements (including REE, except Sc analyzed by XRF) were further analyzed using a Perkin Elmer ICP-OES and a Perkin Elmer Sciex Elan 9000 ICP-MS following a $LiBO_2/LiB_4O_7$ fusion and HNO_3 digestion of a 0.2 g sample. It should be mentioned that REE values reported herein from La to Lu are

based on ICP-MS, whereas Y was analyzed by both methods. In the case of Y, it was found that XRF and ICP-MS measurements are adequately correlated—the same stands for some other elements such as Rb, Th, Pb, U, Nb, Sr, Zr, Ga, Co, Zn, Ni, and V (thus, avg. values were considered for those elements). The total C and S contents were determined, using a Leco analyzer, whereas L.O.I. was achieved on the basis of standard procedures. The chemical composition of investigated bauxite composite samples, in the case of ICP, was achieved using strict QA/QC procedures including, of course, three analytical replicates. Blanks (analytical and method), duplicates, and standard geological and synthetic reference materials provided a measure of background noise, accuracy, and precision. The QA/QC protocol incorporates a granite or quartz sample-prep blank(s) carried through all stages of preparation and analysis as the first sample(s) in the job, a pulp replicate (REP) to monitor analytical precision, a − 10 mesh reject duplicate (DUP) to monitor subsampling variation, a reagent blank (BLK) to measure background, and an aliquot of in-house Reference Materials and Certified Reference Materials (CRM) to monitor accuracy. The in-house Reference Materials were prepared and certified against internationally Certified Reference Materials (CRM), such as CANMET and USGS standards where possible, and they were externally verified at a minimum of three commercial laboratories. The QA/QC data, using four different Reference Materials (STD1, in-house Reference Material based on soil samples; STD2, in-house Reference Material, matrix of geological samples with additional elements spiked into the material; SDT3, in-house Reference Material, based on geological samples; and STD4, CRM from Ore Research & Exploration PTY Ltd. Australia for carbon and sulfur analyses), and appropriate blanks (BLK), are summarized in Table S2 (see Supplementary Material). Concentrations exceeding 5% of the lowest sample concentration or 5 times the detection limit for that element (whichever is higher) the blank reporting > DL were confirmed by re-analysis of the same solution. Elements concentrations of which exceeded 5 times the detection limit and did not repeat values within 10% were flagged and further investigated. In that case, solutions were re-run and, if confirmed, the pulp material was retrieved from the sample to inspect the material for homogeneity and fineness. The process for evaluating reject reruns is the same as for pulp reruns except that 30% is the acceptable tolerance. If reported concentrations are higher than expected values, contamination may have occurred. Preparation blanks were used to monitor contamination only. Concentration of preparation blanks greater than 50 times the sample concentration should be considered and rechecked by first re-analysis of a group of samples followed by re-weighing, if the contamination was confirmed.

Aiming at a systematical investigation the REE geochemistry of Parnassos-Ghiona bauxites, a comparison with relevant karst-type deposits from Mediterranean (including Balkans), Irano-Himalayan, and East Asian bauxite belts, was attempted. Thus, geochemical—spider—diagrams with values normalized, not only to typical geochemical reference values (Chondrites, Upper Continental Crust/UCC, Post Archean Australian Shale/PAAS, North America Shale Composite/NASC, European Shale/ES) but also to karst-type bauxites from the Mediterranean (MED) bauxite belt, have been used. The MED average values concern bulk chemical data from the current study (i.e., Bosnia, Montenegro, Hungary) and the literature [19, 20, 54–67] from the following countries, excluding those from Greece:

(i) Bosnia (Jajce deposit): the current study
(ii) Montenegro (Nikšić deposit): the current study and the literature [20]
(iii) Hungary (Halimba deposit): the current study
(iv) Bulgaria, Croatia, and Romania: literature [54 and references therein]
(v) Italy: literature [19, 55–64]
(vi) Turkey: literature [54, 65–67]

When the average of karst-type bauxites from Balkan countries is utilized in geochemical considerations, that includes the average from the bulk chemical data from Bosnian, Montenegrin, Bulgarian, Croatian and Romanian bauxites, together with Hungarian one (for the literature, see text above).

Finally, analogous spider diagrams were used in order to compare the bulk chemical composition of Greek bauxites between the data of the current study and existing values from the literature [27, 30–47, 68–70]:

(i) Average values of Parnassos-Ghiona bauxites without the data of the current study [30, 31, 33–47]
(ii) Average values of other Greek bauxites (i.e., excluding Parnassos-Ghiona published data) without the data of the current study [36, 37, 39, 40, 43, 68]
(iii) Average of all Greek bauxites (including Parnassos-Ghiona published data), without the data of the current study [27, 30, 31, 33–47, 68–70]

Results and Discussion

Mineralogy and REE Phases in Karst-Type Bauxite Deposits from Parnassos-Ghiona Mines

The studied Fe-depleted or "bleached" bauxites from the Parnassos-Ghiona mines (central Greece) appear as porous white–gray (high-grade) and they concern only diasporic

type, while the Fe-rich samples are massive, red-brown (typical low-grade), and they are present as diasporic and/or boehmitic type (see Supplementary Material; Fig. S1).

The presence of REE-bearing crystalline phases in the studied karst-type bauxite samples was initially investigated by means of PXRD. The PXRD patterns of representative Fe-rich diasporic and Fe-rich boehmitic bauxite samples as well as Fe-depleted or "bleached" diasporic sample are illustrated in Fig. S3 (see Supplementary Material). Results showed that REE or even REE-bearing crystalline phases are not detectable due to their low mineral volume in the studied materials. In contrast, AlOOH polymorphs (diaspore, boehmite), TiO_2 polymorphs (anatase, rutile), Fe-oxide/Fe-oxyhydroxide phases (mainly hematite, magnetite, and goethite) and clays (kaolin-group) are present in bulk in accordance with the literature (e.g., [22, 26, 71 and references therein]). It is worthy to note that the Fe-depleted or "bleached" bauxites usually contain diaspore, and TiO_2 polymorphs, i.e., abundant anatase and minor rutile (possibly detrital), at the macro/micro/nanoscale as it has been revealed recently [22]. Besides, Fe-depleted bauxites also contain fine grained scandian zircons (see text below) and peculiar Fe oxide nanominerals at the nanoscale exhibiting a maghemite-type composition [22]. According to the literature, in the case of the typical Fe-rich samples, except for the major solid crystalline phases (diaspore, boehmite, anatase and hematite), rutile (possibly detrital), clays (e.g., kaolin-group, etc.), gibbsite (γ-AlOOH), goethite and magnetite, as well as accessory crystalline phases, such as detrital zircons and chromites, are occasionally present [26, 36, 38–40, 72]. In the studied bauxite samples, rare earth minerals were not detected by PXRD, but were detected by SEM–EDS/WDS at the microscale (see text below).

In line with PXRD results, initial SEM observations proved that the major phases are Al-oxyhydroxides (diaspore/boehmite), Fe-oxides (mainly hematite), and Ti-oxides (anatase and rutile) dispersed into the diasporic matrix. In contrast to the latter, in some cases, Fe–Ti-oxides (predominantly determined as ilmenite), intergrown with Fe-oxides (hematite) can be rarely confirmed by SEM–EDS (see Supplementary Material; Fig. S4). Furthermore, qualitative SEM–EDS/WDS investigation proved that Fe-rich karst-type bauxites situated at the middle and the lower parts of the B2 and B3 bauxitic horizons of the Parnassos-Ghiona mining area (central Greece) contain detectable quantities of authigenic $LREE^{3+}$ fluorocarbonate minerals, such as bastnäsite/parisite group ([26, 73]; see Supplementary Material; Fig. S4 and Figs. 1 and 2). On the other hand, no REE-mineral phase has been observed to be accumulated at the Fe-depleted studied bauxites located at the uppermost parts of the B3 bauxitic horizon, except for

peculiar REE-containing zircons at the microscale (i.e., scandian zircons: see text below). In some cases, significant concentration of Th has been detected into $LREE^{3+}$ fluorocarbonate minerals (up to $\sim$ 2.5 wt% ThO_2 in the Fe-rich samples) at the microscale [26] (see Supplementary Material; Fig. S4). Previous microscopic studies about REE-phases in Greek bauxites have not reported the presence of Th in Nd-(hydroxyl)-bastnäsite [29], except Gamaletsos et al. [26] that revealed the existence of Th in LREE-minerals, as well as in Ti-oxides (mostly anatase) and detrital zircons. Besides, Th-containing Y-phosphates have not been clearly approved in line with the literature [26, 27]. It should also be emphasized that Th was not detected in AlOOH matrix or in any other Fe-, Ti- and Fe–Ti-phase of the Parnassos-Ghiona bauxites in accordance with previous studies [22, 26]. Besides, there are few isolated Ce–Al-hydroxyphosphate grains corresponding to florencite, in accordance with the literature [27] (see Fig. 3). The existence of "authigenic" LREE oxides (together with an unexplained kaolinite-associated REE phase), corresponding to cerianite-type phases, has been reported (e.g., [24 and references therein]) based on a single Raman spectrum [31], without showing further microanalytical details [24, 28, 31]. Unlike previous works showing the presence of monazite, rhabdophane, xenotime, and churchite [27, 30], the current study did not indicate the latter REE-phases. The presence of authigenic LREE-(hydroxyl)-bastnäsite and monazite REE-types in the Greek bauxites from the Marmara and Nissi localities, but not from the Parnassos-Ghiona active mining area, was proved [74] and has been summarized in a review [75 and references therein]. Finally, there are LREE phases that co-exist with detrital Fe–Ni-sulfides and, particularly, with pentlandite-type phases (see quantitative elemental maps b and c of Figs. 2 and 4). In that case, a primary mineral derived from mafic/ultramafic parent rocks, is actually surrounded by a secondary—authigenic/diagenetic—phase consisting of elements, i.e., REE, derived by other geological sources. Such Fe–Ni-bearing mineral phases with regard to the Parnassos-Ghiona bauxite ore deposits are demonstrated for the first time in the literature.

The presence of LREE-minerals has been described as the result of intense leaching processes that have been taken place in-situ [73 and references therein]. Leaching might drove to the mobilization of rare earth elements during bauxitization processes and finally to the in-situ enrichment of LREE and the formations of secondary authigenic LREE-minerals in karst-type bauxite deposits of Parnassos-Ghiona mines. It is proved herein that LREE-minerals can occur between iolites, bauxite cavities, and/or dispersed into the AlOOH matrix as micropore fillings either as irregular segregations or as nebular impregnations in line with the literature [73 and references therein].
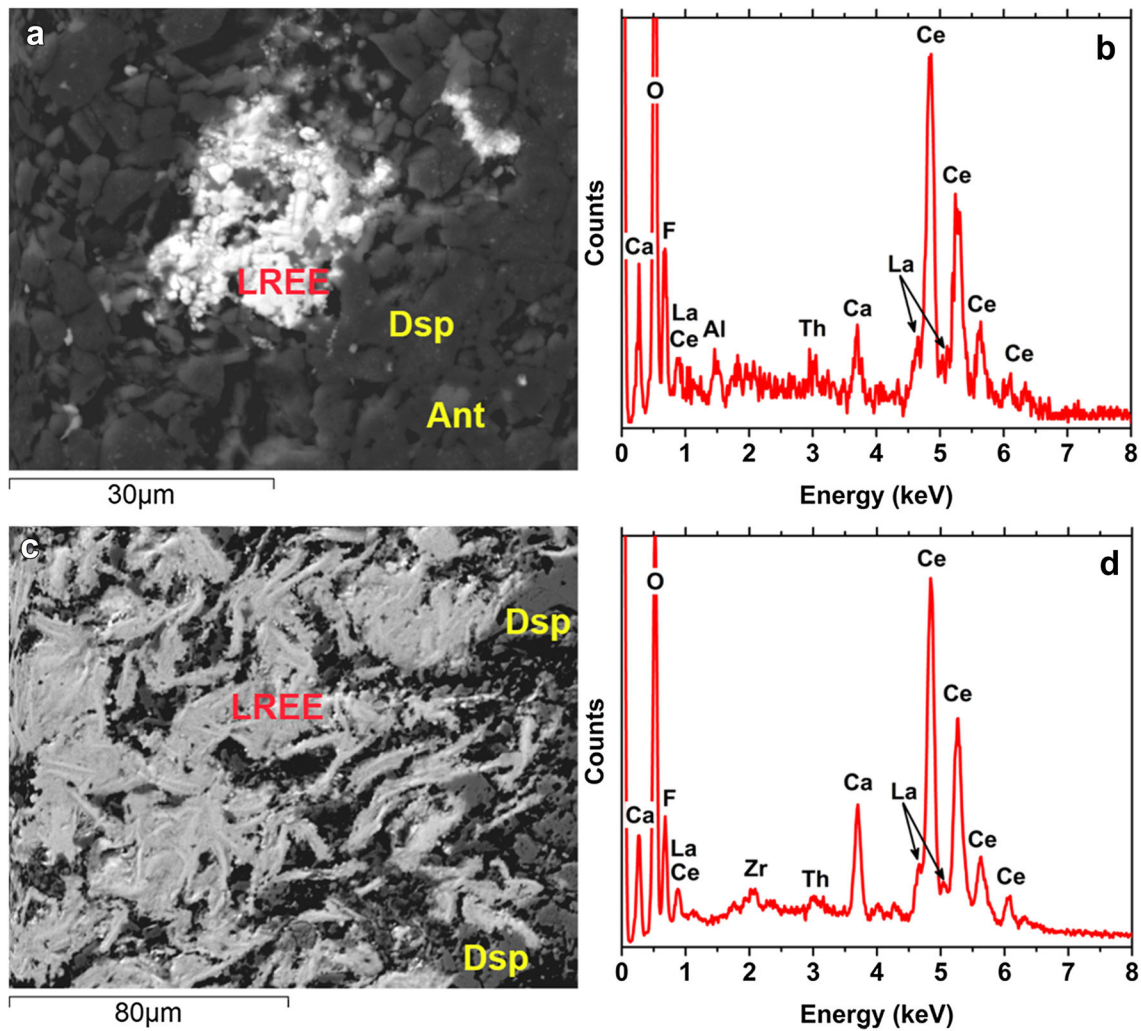
Fig. 1 SEM–EDS/–WDS data for LREE^{3+} fluorocarbonate minerals (mostly bastnäsite/parisite group: $(REE)^{3+}Ca^{2+}F(CO_3)_2$; e.g., [73]) of Parnassos-Ghiona bauxites. Al and Zr peaks at spectra (images **b** and **d**) are attributed to the contribution of diasporic matrix and submicro/nanosized zircons, respectively (see Fig. 5 and relevant text). *LREE* for LREE^{3+} fluorocarbonate minerals, *Dsp* for diaspore of the matrix, *Ant* for anatase (Color figure online)

Concerning Sc phases, there are no Sc minerals detected either by PXRD or SEM–EDS/SEM–WDS. However, Sc-bearing phases, and particularly several Sc-containing zircon—detrital—microcrystals have been detected in the studied Fe-depleted bauxites (Fig. 5). To the best of our knowledge, this is the first time in the literature—along with a study that only recently appeared (in fact, only weeks before the present work got released) but without further geochemical details [32]—that scandian zircons have been observed at the Alpine orogenetic system. Since scandian zircons have been observed in apatite-rich oolitic ironstones from Ordovician orogeny (Saint-Aubin-des-Châteaux, Armorican Massif, France) [76] and in P-Bi-Nb-Sc-U-F-rich zircons from the late-Variscan peraluminous Podlesí granite system (Czech Republic) [77], this is the third case in geological material in the literature. Nevertheless, Gramaccioli et al. [78] claimed the discovery of a highly scandian variety of zircon at Baveno (Italy), without reported data to support their findings. The authors mentioned that the similarity in the ionic radii between Sc^{3+} and Zr^{4+} + Hf^{3+}may explain the Sc incorporation in zircons. The length of the Sc-zircon grains can reach up to few tens of microns. According to microanalysis, Sc is incorporated in zircons of the Parnassos-Ghiona bauxite, in concentration up to 8200 ppm, higher than 7240 ppm determined elsewhere [32]. Apart from Sc, the fine grained scandian zircons contain significant amount of actinide elements (Th, U), Hf and HREE, such as Y and Yb (see images A, B and C of Fig. 5). Scandium is undetectable by SEM–EDS/SEM–WDS in the surrounding AlOOH matrix of the Sc-zircons (Fig. 5d). The latter is in contrast to very recent EPMA observations claiming that aluminum oxyhydroxide matrices contain ∼ 10 ppm of Sc [32]. It is well established that WDS can achieve detection limits (DL)

down to 100 ppm in exceptional cases, with 10 ppm in "ideal" conditions where there are no peak interferences and negligible matrix absorption. Moreover, many microscopic analysts claim that the WDS practical DL in the "real" conditions can reach $\sim$ 200 ppm (in the case of peak interferences) down to $\sim$ 100 ppm (in the case of non-peak interferences) (e.g., [79, 80]). Thus, the 10 ppm Sc accumulation in aluminum oxyhydroxide matrices fosters debate; there are two possibilities: the 10 ppm is spread uniformly throughout the studied matrices or most of that material has probably undetectable Sc amount (e.g., < 1 ppm), but a small volume fraction contains submicro/nanoscale phases that host Sc as major element. Consequently, especially in the case of severe interference of Sc and Ca peaks, a critical question is being raised: does the size of the interaction volume fit with the probed Sc-bearing submicro/nanoscale volume in the aluminum oxyhydroxide matrices?

Although it is revealed that Sc can be intercorrelated with zircons at the microscale in the case of the studied bauxites, the bulk geochemistry in Parnassos-Ghiona bauxites, however, shows no significant correlation of Sc with any other major or trace elements, except for Fe (see text below). This microscale study has been confirmed very
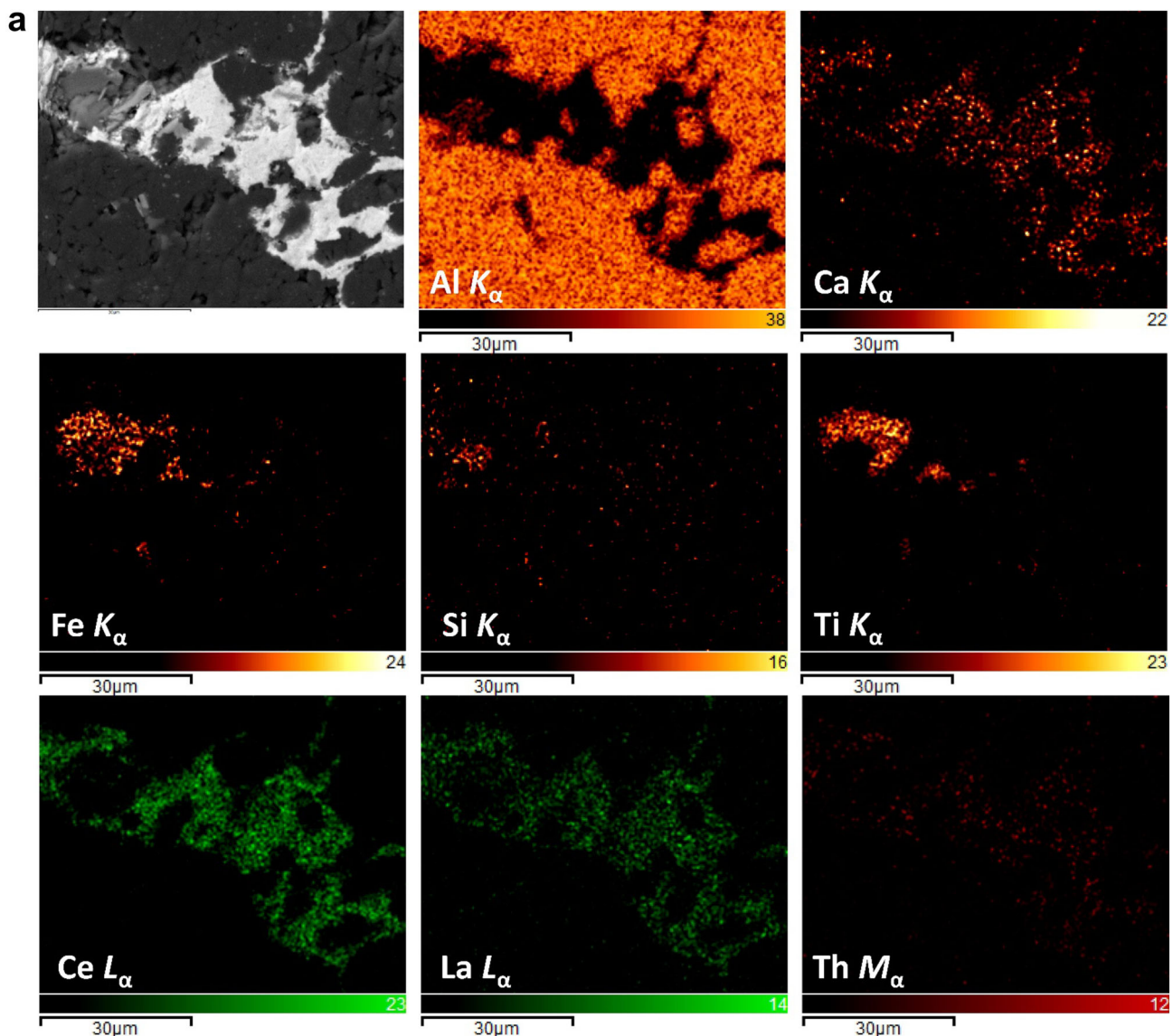

Fig. 2 SEM–EDS/–WDS elemental quantitative maps (at.%) concerning LREE^{3+} fluorocarbonate minerals of Parnassos-Ghiona bauxites (**a–c**). Ce and La have been illustrated as proxies for LREE. A representative REE-phase that contains Th (up to 2.5 wt% according to SEM–EDS/–WDS microanalysis) into the diasporic matrix (map **a**), while another REE-phase together with Fe–Ni-phase (maps **b** and **c**; map **C** concerns a separated map from an enlarged view of map **b** (red rectangular area) (Color figure online)
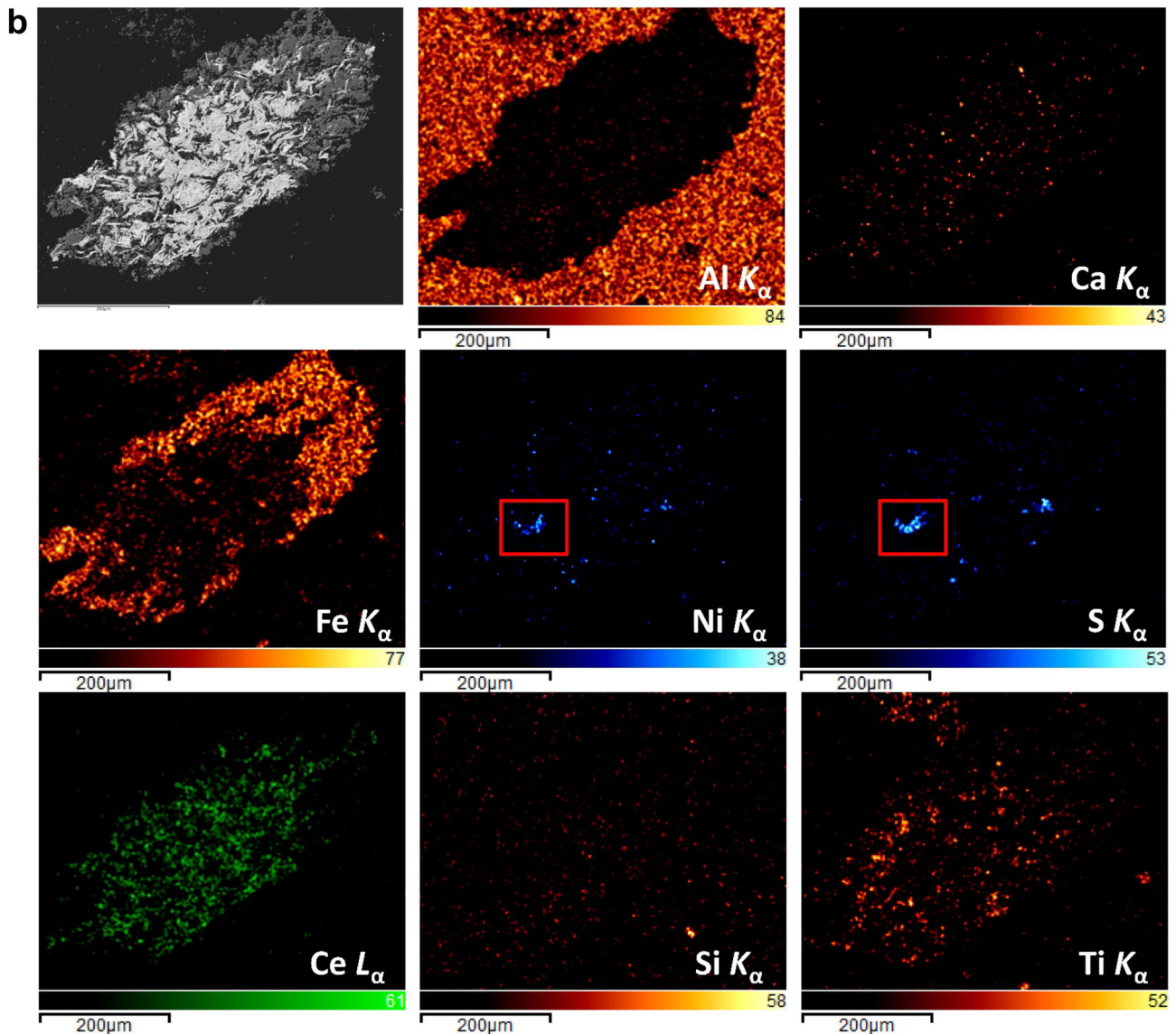
Fig. 2 continued

recently [32], while it is also in accordance with a recent publication that proved that the hosting phase of Sc is Fe-oxides in unusually high-grade Australian lateritic Sc ores [81]. According to Chassé et al. [81], most of Sc budget is adsorbed on goethite and the remaining Sc^{3+} substitutes for Fe^{3+} in the structure of hematite in Australian case study. Concerning karst-type bauxites from Italy, it has been suggested that Sc is generally controlled by Fe-oxyhydroxides and might be present as detrital Fe-rich minerals [19, 63].

In order to review the REE phases in the studied bauxites, taking into account the results of the current study and the existing literature, Table 1 is presented.

Trace Elements and REE Geochemistry of Karst-Type Bauxites from Parnassos-Ghiona Mines

The bulk chemical composition of the studied Fe-rich and Fe-depleted "bleached" bauxites from Parnassos-Ghiona mines has been yielded by means of XRF and ICP-OES/MS measurements (see Supplementary Material; Table S3). The Upper Continental Crust/UCC-normalized spider diagrams [82] have indicated an enrichment in High-Field Strength Elements (HFSE) such as REE, Ta, Nb, Zr, and Hf, with an exception of particular LREE (i.e., Sm, Eu, Pr, and Gd) in the case of Fe-depleted samples. Besides, both Fe-rich and Fe-depleted bauxites are enriched in
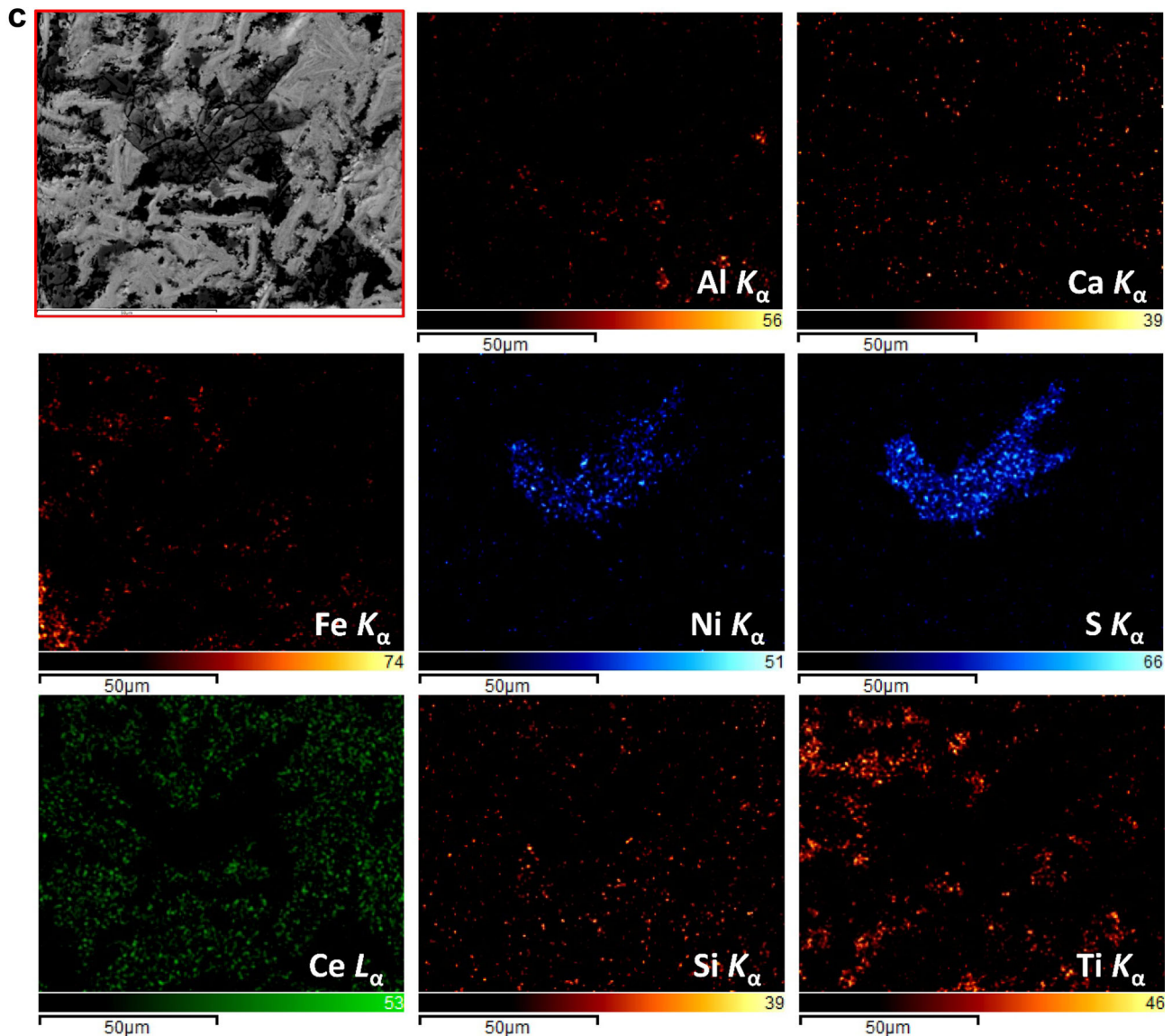
Fig. 2 continued

actinide elements (Th, U), as well as in most of the compatible elements compared to UCC [82]. In contrast, there is a depletion in Large Ion Lithophilic Elements (LILE, i.e., Cs, Rb, and K), as well in P, and Sr, and certain compatible elements such as Zn and Cu. While As, Pb, and Co are enriched in the Fe-rich bauxites, they are, however, relatively present with lower concentrations in the Fe-depleted bauxite samples (see upper image of Fig. 6 and Supplementary Material; Fig. S5). In particular, the studied Fe-rich bauxites are enriched in Pb (up to 123.9 ppm), As (up to 176.7 ppm), and Co (up to 98.9 ppm), compared to the Fe-depleted bauxites (Pb: from 1.3 to 4.35 ppm; As: from 0.39 to 0.5 ppm; Co: from 3.4 to 4.6 ppm), see Table S3 of Supplementary Material.

Based on bulk chemical analysis, it can be argued that there is a correlation between trace elements (see Supplementary Material; Figures S6–S8). Abroad positive correlation between Pb and Fe provides evidence that Pb might be contained in Fe-oxides and/or Fe-oxyhydroxides. It is known that Pb shows a strong affinity for hematite and, additionally, for goethite, during metal uptake (sorption) geochemical processes in aqueous environments (e.g., [83, 84]). Nevertheless, broad Pb–Si and Pb-K positive correlations and an apparent relationship between Pb and Mg, Ca have been observed, too. A broad inverse correlation of Pb with Al has been detected (see Supplementary Material; Fig. S6). These geochemical correlations might address a probable sorption of Pb in Al–Si–K-phases (e.g.,
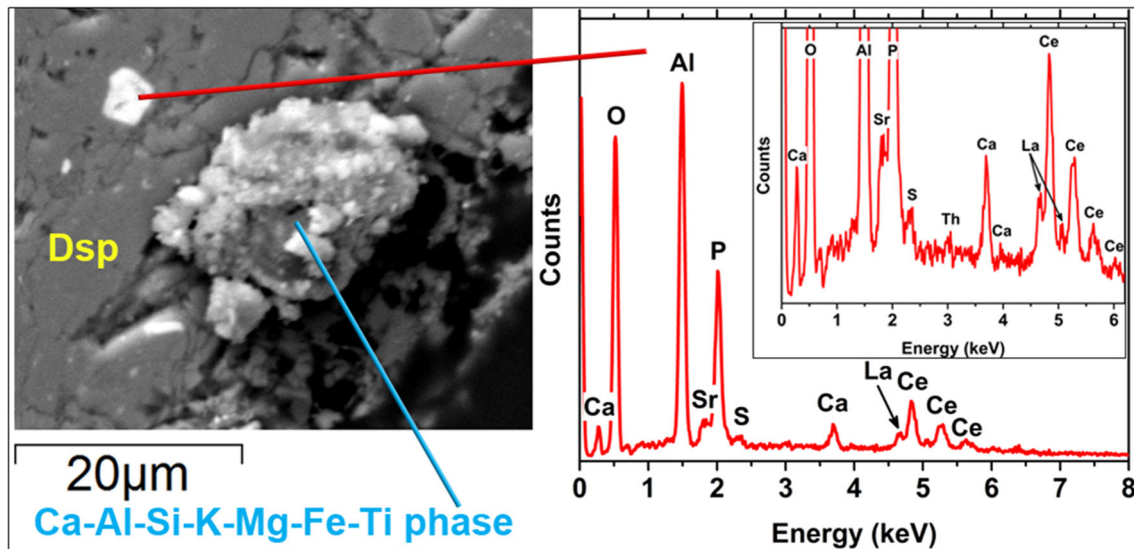
Fig. 3 SEM–EDS/–WDS data of florencite (Ce–Al-hydroxyphosphate) in the studied bauxite samples from Parnassos-Ghiona mine. *Dsp* diaspore (Color figure online)

clay-like phase) and that Pb is not connected with AlOOH phases. In a similar geochemical approach, As is probably related to Fe in bulk (see Supplementary Material; Fig. S7), and particularly it seems that it is incorporated into Fe–Cr–Ti in pisoliths in the form of arsenates (As^{5+}), as revealed by Synchrotron Radiation (SR) μ-XRF and As K-edge μ-XANES spectra (see Supplementary Material; Fig. S9). Apart from the rare earth elements, the general enrichment of Parnassos-Ghiona bauxites in certain HFSE including actinides (i.e., Nb, Ta, Th, U) is due to Ti-oxides (namely anatase), as it has been revealed by a combined Laser—and Synchrotron-based analytical investigation in microscale [26]. Taking into account the literature of all Greek bauxites on the subject studied herein [27, 30, 31, 33–47, 68–70], it is agreed that there are similar enrichment/depletion trends, though in some cases there are favorable concentrations of REE as well as As and Sb (see middle image of Fig. 6).

When the studied Fe-rich and Fe-depleted Parnassos-Ghiona bauxites are normalized to the average of karst-type bauxites from the Mediterranean bauxite belt [19, 20, 54–67], namely "MED-normalized" [19, 20, 54–67] (for the relevant literature, see also the "Materials and Methods"), significant enrichment in W, Mo, Co, Ni, Sb, and Hg was revealed (see Supplementary Material; Fig. S10). The same geochemical trends also stand for all Greek bauxites [27, 30, 31, 33–47, 68–70] (for the relevant literature, see also the "Materials and Methods"; lower image of Fig. 6). Based on geochemical binary diagrams, Co is broadly related to Cu and less correlated with Zn and Mg in the Parnassos-Ghiona bauxites (see Supplementary Material; upper image of Fig. S8). According to SEM–EDS investigation, Ni is present; at

least, in distinct Fe–Ni-sulfides corresponding to detrital pentlandite phases (see text above and Figs. 2 and 4).

Based on the binary correlation diagrams, there is a strong correlation of SiO$_2$ with distinct LILE such as K, Rb, Cs (and Ba). Potassium is most likely related to unidentified minor micro/nanosized silicate minerals (clays), which could also be true for Rb and Cs, as well as for Ca (see Supplementary Material; lower image of Fig. S8). The broad negative correlation between Al and Fe, especially in the case of Fe-depleted bauxites (see Supplementary Material; upper image of Fig. S11), indicates strong mobility of Fe while Al content is increased (e.g., [57, 59]). This reflects the intense leaching process that removed most of Fe content through late stages of entire bauxitization, resulting in the formation of the Fe-depleted or "bleached" bauxites. In particular, intense supergene/epigenetic processes drove to a final epigenetic Fe migration/epigenetic Fe bleaching related, most likely, to the formation of Fe-depleted bauxite in the uppermost part of the B3 horizon of Parnassos-Ghiona area (e.g., [85, 86]). The redistribution of Fe, and the segregation of Al and Fe, is a necessary process in bauxite formation because ferruginous minerals tend to contaminate the ore. High-quality bauxitic ores (i.e., Fe-depleted or "bleached") require that both Fe and Si be removed, but not alumina. The Fe mobilization from the "bleached" samples is also supported by its negligible presence—compared to its bulk concentration in the case of Fe-rich samples—into diaspore, which concerns in fact diaspore a distinct Fe^{3+}–Cr^{3+}–AlOOH low-T authigenic phase described for first time in literature [22]. The correlation of Al and Cr is not obvious in bulk geochemistry. It is only revealed in microscale and nanoscale study [22]. A strong correlation
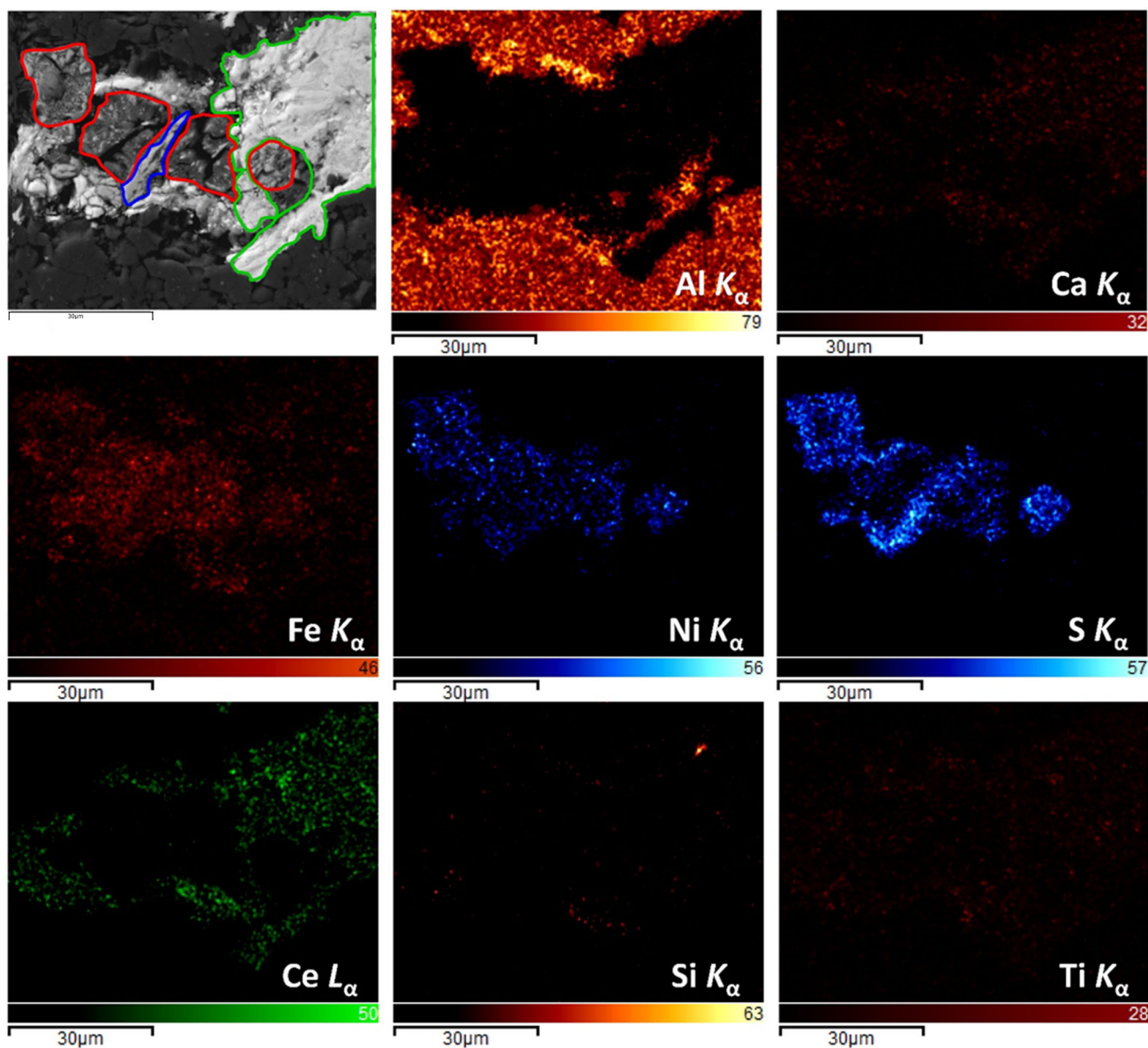
Fig. 4 SEM–EDS/–WDS elemental quantitative maps (at.%) of detrital Fe–Ni-sulfides (pentlandite-type phase) together with REE-phases into Parnassos-Ghiona bauxite. The occurrence of the Fe–Ni-sulfide might address a mafic/ultramafic parental affinity of the deposit (Color figure online)

is observed between Zr and Ti, Zr and Nb, and especially Zr-Hf implying the presence of Hf into detrital zircon crystals (see Supplementary Material; upper image of Fig. S12). Zr-Hf relationship is also observed in the case of the—detrital—scandian zircons as it has been discussed above (see text above and Fig. 5). Al and Ga are reasonably correlated broadly due to similarities in ionic radii and valence, but it can be concluded that Ga (avg. for all bauxites: 68.2 ppm) is apparently not correlated with Fe-phases as stands for Sc (see text below), Pb and As (see Supplementary Material; lower image of Fig. S12). That means, among all trace elements examined in the current study, Th and U (in the case of LREE fluorocarbonates and zircons) and Pb and As (in the case of possible Fe- and Sc-bearing phases; see text below), are actually related to REE. Thorium, is additionally related to the observed radioactivity in Parnassos-Ghiona bauxites and the bauxite metallurgical residue (red mud), occurring into anatase and nanoperovskite (e.g., [23, 26 and references therein]). Moreover, V, either as critical metal extracted as byproduct of other metal ores [87] or as potential hazardous element due to its involvement in red mud accident in Hungary [88], is an element of increased importance in aluminum mining and metallurgical industry. While binary geochemical diagrams showed that V seems to be related neither to Fe nor to any other metal in bulk, preliminary SR
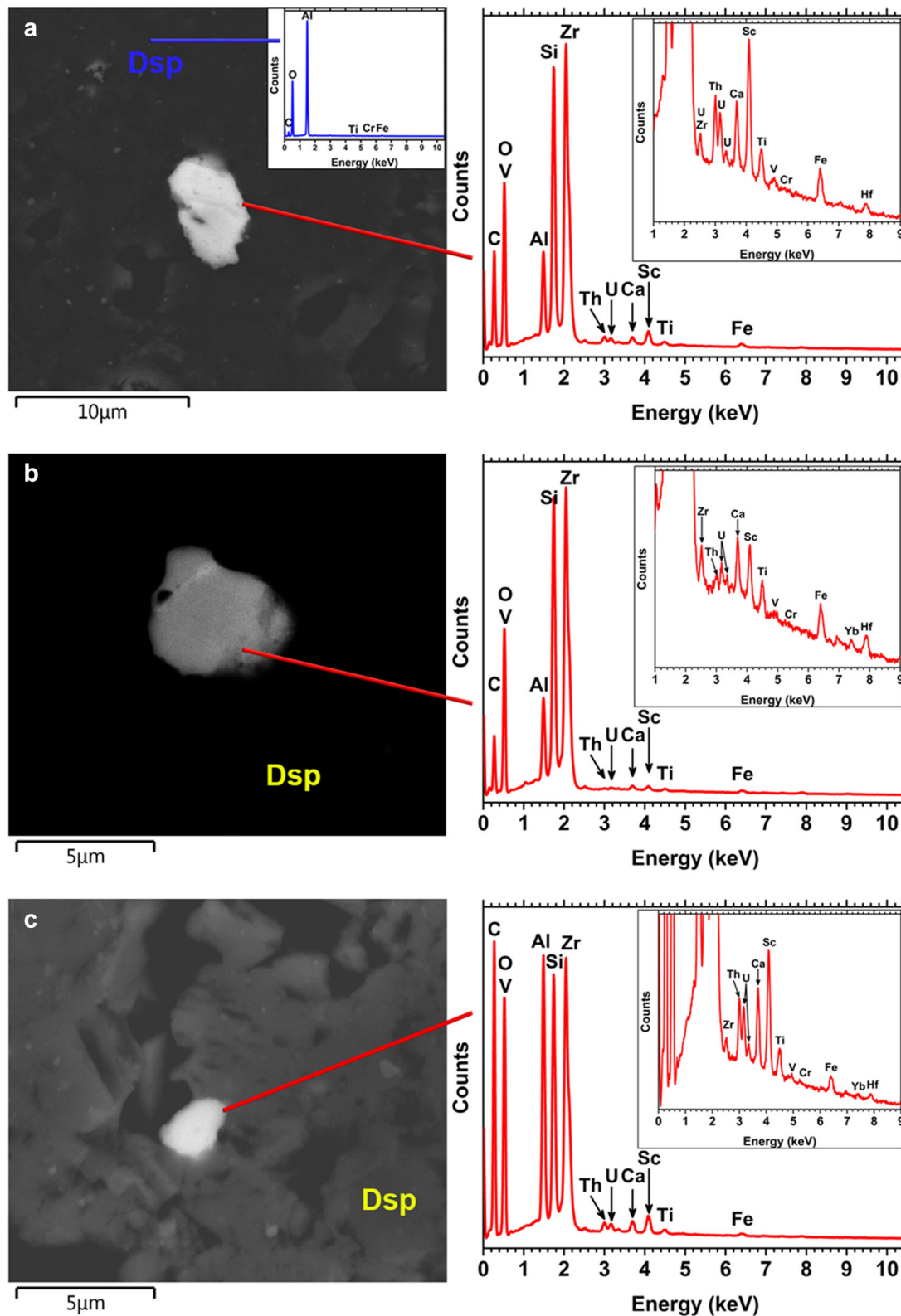
Fig. 5 SEM–EDS/SEM–WDS data of fine-grained Scandian zircons in the studied Fe-depleted (high-grade) karst-type bauxites from Parnassos-Ghiona mining area, Greece (**a–c**). A representative SEM-EDS point analysis obtained at the surrounding diasporic matrix of the Scandian zircon grains is additionally illustrated (see inset of SEM-BSED image **a**). In accordance with the literature [22, 25], diasporic matrix contains significant Fe, Ti, and Cr amounts. *Dsp* diaspore of the matrix (Color figure online)

Table 1 A summary of all the REE-bearing minerals in karst-type bauxites from the B2 and B3 bauxitic horizons of the Parnassos-Ghiona active mining area, central Greece (the current study and literature [24, 26–32]

REE-bearing phase	Source (literature)
LREE^{3+} fluorocarbonate (bastnäsite/parisite group) including Nd-(hydroxyl)-bastnäsite	Present study
	[26, 29]
LREE oxides or LREE carbonates/hydroxycarbonates	[24 and references therein], [28]
Ce–Al-hydroxyphosphates (florencite)	Present study
	[27]
Rhabdophane, Xenotime, Churchite	[27]
Monazite	[30]
Cerianite, Kaolinite-associated authigenic REE-phase	[31]
Scandian zircon	Present study
	[32]
Sc-bearing Fe-oxide phases (mainly hematite and goethite)	[32]

µ-XRF and µ-XAFS investigation indicated that high-valence V is mainly intercorrelated to Si, Ca and Mg in microareas between Fe–Cr-Ti pisoliths [25]. That means, there is no indication (as in the case of Th, U, Pb and As) of V correlation with REE. Moreover, the Parnassos-Ghiona bauxite samples, analyzed in the frame of the current study, seem to be enriched in W when compared to the average of bauxites from Italy, Turkey, Balkan countries and the Mediterranean bauxite belt [19, 20, 54–67] (for the relevant literature, see also the "Materials and Methods"). This also stands for all Greek bauxites [27, 30, 31, 33–47, 68–70] (for the relevant literature, see also the "Materials and Methods"; middle image of Fig. 6). In general, the bulk geochemical trends of the Greek bauxites are well comparable to karst-type bauxites of neighboring countries belonging to the Mediterranean bauxite belt [19, 20, 54–67] (see Tables S3 and S4 of Supplementary Material and upper image of Fig. 7). Moreover, the studied Parnassos-Ghiona bauxites (Greece) have been compared to Iranian karst-type bauxites belonging to Irano-Himalayan bauxite belt (i.e., Permo-Triassic [89–91] and Mesozoic bauxite deposits [92–97]; see middle image of Fig. 7) and to Chinese karst-type bauxites that belong to East Asian bauxite belt (i.e., Quaternary [98–100], Permian [99–103] and Cambrian bauxite deposits [104]; see lower image of Fig. 7). A geochemical comparison between karst-type bauxites from Iran and China with those from Parnassos-Ghiona mines reveals enrichment in Rb, K and Cd (in the case of Iranian) as well as in K, REE, Ni and V (in the case of Chinese). It should be noted that the relative depletion in K observed in Salento-type bauxite (i.e., Quaternary deposits [98–100]) from China is due to post-weathering surface processes.

Going into details of REE geochemistry of the studied Parnassos-Ghiona bauxites (the current study), the geochemical analyses (see Supplementary Material; Table S3)

of representative samples, from underground mines and open pits, revealed an increased content in LREE (ΣLREE—from La to Gd—varying from 106 to 913 ppm; avg. ΣLREE = 321 ppm; $n = 17$), and lower HREE (ΣHREE—from Tb to Lu including Y—varying between 45 and 179 ppm; avg. ΣHREE = 95; $n = 17$). The overall REE concentration (ΣREE + Y+Sc) varies from 192 to 1109 ppm (avg. 463 ppm; $n = 17$). The most abundant REE is Ce (min: 67 ppm; max: 655 ppm; avg. 193 ppm; $n = 17$). On the other hand, Nd, which is more important for the industry, is lower (avg. 41 ppm; $n = 17$). Unlike the Fe-depleted bauxites, it is evident that the Fe-rich types are preferentially enriched in REE. In particular, the Fe-rich bauxites contain an avg. ΣREE + Y+Sc = 569 ppm (avg. in Fe-depleted: 268 ppm). The REE concentrations in Fe-rich bauxites are elevated, simply due to higher content of REE minerals (of diagenetic and/or epigenetic origin), mostly LREE fluorocarbonates (compared to the few isolated Ce–Al-hydroxyphosphate grains, as indicated by the SEM–EDS investigation (see text above). Bulk geochemistry in Parnassos-Ghiona bauxites (the current study) shows an apparent positive correlation between Sc and Fe, while there is no negative correlation with Al. Unlike SEM–EDS/SEM–WDS data revealing that Sc is incorporated into zircons (see text above and Fig. 5), there is no apparent relation of Sc to any other major or trace element such as Zr in bulk (Fig. 8). A bulk positive Sc–V correlation in Parnassos-Ghiona bauxites (Greece) cannot be proved, even though Mongelli et al. [19] proposed it in the case of Italian karst bauxites. A comparison between the ΣREE values of the samples from different bauxitic horizons (i.e., B2 and B3), reveals that those from the B2 are significantly enriched in REE compared to samples from the B3 horizon (see Supplementary Material; Table S3). When both Fe-rich and Fe-depleted Greek bauxites are normalized to North America Shale Composite (NASC;

Fig. 6 *Upper image* UCC-normalized [82] spider diagram for the average of the Parnassos-Ghiona bauxites (the current study); *middle image* UCC-normalized [82] spider diagram for all Greek karst bauxites [27, 30, 31, 33–47, 68–70]; *lower image* Mediterranean bauxite belt MED-normalized [19, 20, 54–67] spider diagram for all Greek bauxites (current study and the literature [27, 30, 31, 33–47, 68–70]). For the relevant literature, see also the "Materials and Methods" (Color figure online)
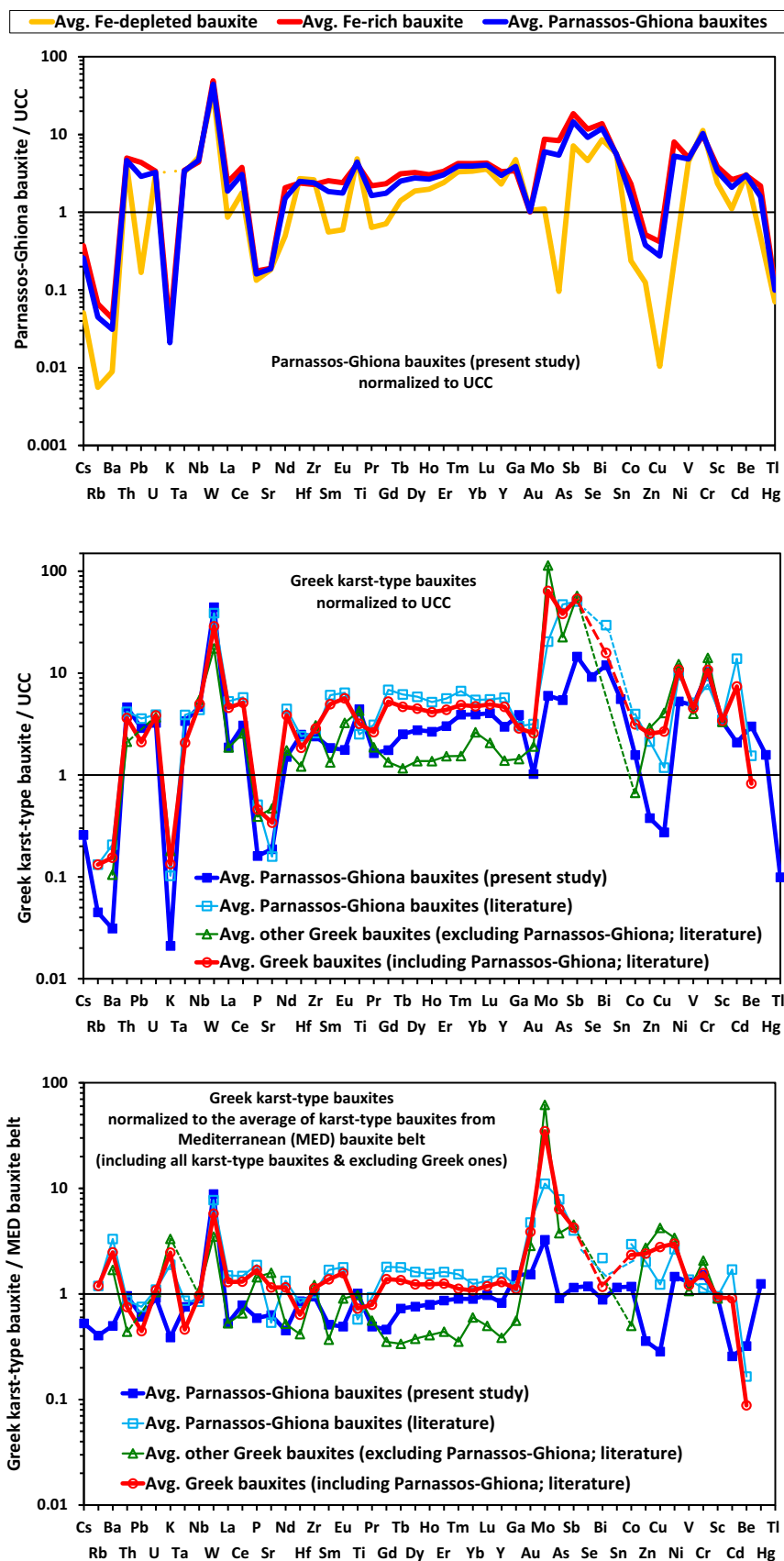
Fig. 7 *Upper image* UCC-normalized [82] spider diagrams for the average of the Parnassos-Ghiona bauxites (the current study) in comparison with the average of karst bauxites from Italy, Turkey, Balkan countries, and the Mediterranean (MED) bauxite belt [19, 20, 54–67]. For the relevant literature, see also the "Materials and Methods"; *middle and lower images* UCC-normalized [82] spider diagrams for the average of the Parnassos-Ghiona bauxites (the current study) compared to the average of karst-type bauxites from Iran (see *middle image*; Permo-Triassic bauxites [89–91] and Mesozoic bauxites: [92–97]), and to the average of karst-type bauxites from China (see *lower image*; Quaternary bauxites: [98–100] and Permian bauxites: [99–103] as well as Cambrian bauxites: [104]) (Color figure online)
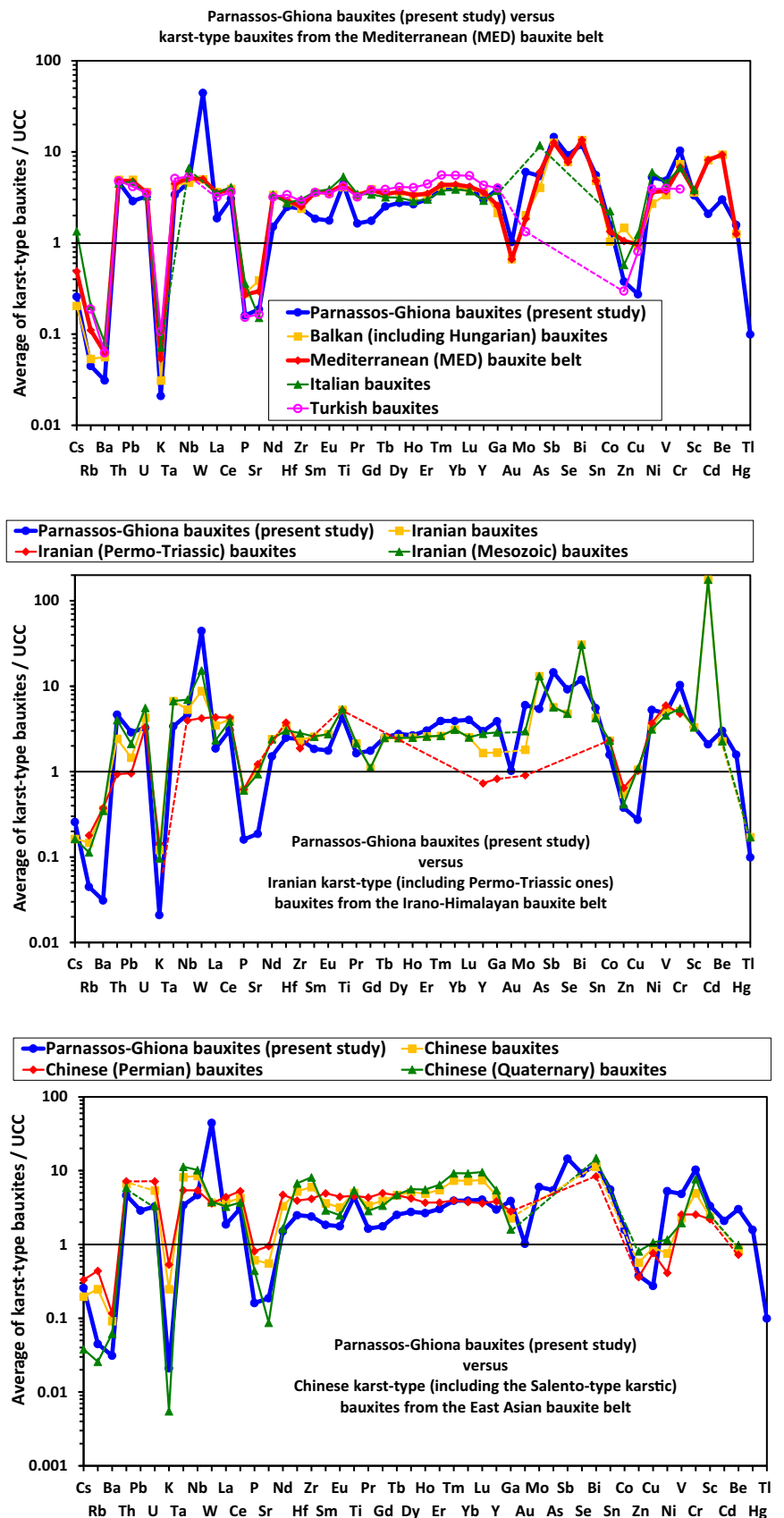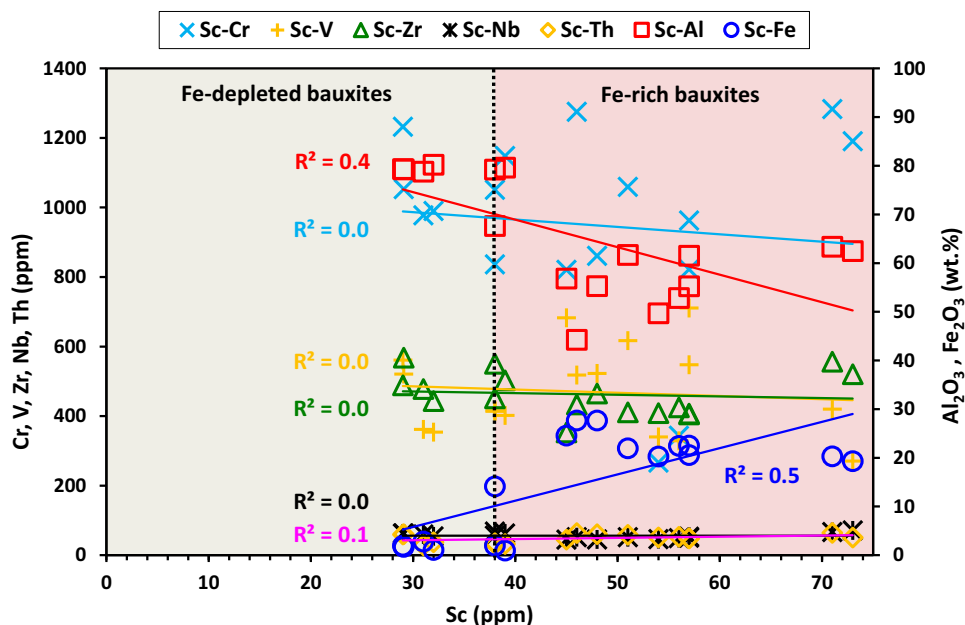
Fig. 8 Binary diagrams of Sc versus Al, Fe, Cr, V, Zr, Nb, and Th illustrating the correlation between scandium and major and trace elements for the Parnassos-Ghiona bauxites (the current study) (Color figure online)

[105]) there is an evident positive Ce geochemical anomaly, i.e., positive Ce^A (see Supplementary Material; Fig. S13). In the case of NASC-normalization [105], there is also a Gd positive anomaly (not evident in chondrite-normalization [106–113]; see text below) and a relative enrichment in HREE, especially in the case of Fe-depleted samples.

The chondrite-normalized diagrams [106–113], concerning REE in average, of the Fe-rich and the Fe-depleted bauxites are presented in Figures S14 and S15 (see Supplementary Material). These diagrams are also referred as Masuda-Coryell diagrams (e.g., [114]). In particular, for choosing the most proper set of chondrite-normalization values, selected average values of ordinary chondrites/OC [107–109, 113], and carbonaceous chondrites/CI [106, 112], as well as values reported by Korotev [110, 111]—who utilized the CI values from Anders and Grevesse [115] multiplied by 1.3596—were carefully used from an overall set of available published data [106–113, 115–122].This approach was based on comments by Rollinson [114] and suggestions by Korotev [123]. Furthermore, values from CI chondrites have been selectively chosen in order to be consistent with the average values of OC chondrites reported by Haskin et al. [107–109], and Wakita et al. [113]. Similar to the case of NASC-normalization [105] (see Supplementary Material; Fig. S13), there is an evident positive Ce/Ce* (Ce^A); besides there is also a rather negative Eu/Eu* (Eu^A). In both cases, the REE-normalized curves show similar geochemical trends.

As observed in the literature, analogous to the above approach, the "Masuda-Coryell" diagrams were produced

using average REE values for normalization different from that of the average abundance of REE in chondrites [106–113] (see Supplementary Material; Figures S14 and S15), such as the average abundance of REE in the European Shale/ES [120] (see Supplementary Material; Fig. S16), the Upper Continental Crust/UCC [82] (see Supplementary Material; Fig. S17), the Post-Archaean average Australian Sedimentary rock/PAAS [112, 125] (see Supplementary Material; Fig. S18) and, for the first time in the literature, the average abundance of REE in the Mediterranean bauxite belt (MED-normalized) excluding the Greek ones [19, 20, 54–67] (for the relevant literature, see also the "Materials and Methods"; see Supplementary Material; Fig. S19). Conclusively, similar to the case of NASC-normalization [105] (see Supplementary Material; Fig. S13) and chondrite-normalization [106–113] (see Supplementary Material; Figures S14 and S15), an evident positive Ce^A can be observed in the "Masuda-Coryell" diagrams for the studied Parnassos-Ghiona bauxite when are normalized to ES [124] (see Supplementary Material; Fig. S16), to UCC [82] (see Supplementary Material; Fig. S17), to PAAS [112, 125] (see Supplementary Material; Fig. S18) or even to Mediterranean bauxite belt [19, 20, 54–67] (see Supplementary Material; Fig. S19). On the other hand, contrary to the similar negative Eu^A for the case of chondrite normalization [106–113], in all the other cases there is no considerable Eu anomaly. Finally, one can say that the REE-normalized curves show similar geochemical trends, especially in the cases of NASC [105], ES [124], UCC [82], PAAS [112, 125] and MED [19, 20, 54–67] normalizations. An apparent HREE enrichment is notable when the studied Parnassos-Ghiona bauxites are normalized with the average

REE values of ES [120], UCC [82] and PAAS [112, 125]. The robust similarities of all the above "Masuda-Coryell" diagrams are illustrated in Fig. 9. The same geochemical trends (Fig. 10) also stand for the Parnassos-Ghiona bauxites (the current study) and, also for all Greek bauxites [27, 30, 31, 33–47, 68–70] (for the relevant literature, see also the "Materials and Methods") when their REE values are normalized to the average abundance of REE in the chondrite [106–113], PAAS [112, 125], and Mediterranean bauxite belt [19, 20, 54–67] (for the relevant literature, see also the "Materials and Methods"). An apparent positive Eu^A is observed only in the case of bauxites from other areas of Greece (namely "other Greek bauxites"), excluding Parnassos-Ghiona published data [36, 37, 39, 40, 43, 68] (for the relevant literature, see also the "Materials and Methods"; see Fig. 10).

According to the findings of the current study, the most abundant REE is Ce (min: 67 ppm; max: 655 ppm; avg. 193 ppm; $n = 17$), exhibiting, as mentioned, a general positive geochemical anomaly (avg. Ce/Ce* or Ce^A: 2.6; see Fig. 11), analogous to the case of marine Fe–Mn-crust [122–127], marine Fe–Mn-nodules [128, 132, 133], terrestrial desert Fe–Mn varnish [134], Brazilian lateritic bauxite [135], xenoliths [136] and Greek bauxite metallurgical residue/red mud (e.g., [23]), implying also that Ce^{4+} may exist either in REE-oxides and/or epigenetically sorbed in Fe-oxides [134–136]. On the other hand, in the case of Middle Proterozoic Fe-REE-Nb-Th deposit of Bayan Obo (e.g., [11]), which is the world's largest REE resource, though there is a typically enormous enrichment in LREE relative to HREE (occurring as REE fluorocarbonate minerals and monazite into dolomite marbles), there

is neither apparent positive nor negative Ce^A (see Fig. 11). This strong LREE enrichment may be attributed to a very low degree ($< 1\%$) of partial melting of parental magmas derived from a source, enriched in incompatible elements (including REE), from subcontinental upper mantle [137 and references therein]. In general, the reference granite [138, 139] and the majority of igneous REE deposits, including carbonatites and Bayan Obo deposit, do not significantly show evidence of neither positive nor negative Ce/Ce* (Ce^A) when normalized to primitive mantle [137 and references therein]. Nevertheless, the studied Parnassos-Ghiona bauxites exhibit significant positive Ce^A, which is calculated using the equation suggested by German and Elderfield [140], when normalized to any reference material as it is mentioned above (chondrite [106–113], NASC [105], PAAS [112, 125], ES [124], UCC [82] and the average of Mediterranean bauxite belt [19, 20, 54–67]; see Figs. 9 and 10 and Supplementary Material; Figs. S13–S19). However, it is worthy to note that karst-type bauxites from Parnassos-Ghiona area and other areas of Greece based on previous studies [27, 30, 31, 33–47, 68–70] (for the relevant literature, see also the "Materials and Methods") do not exhibit similar intense positive Ce^A, while they seem to be relatively enriched in REE when they are compared with the Parnassos-Ghiona bauxites of the current study (Fig. 10). Moreover, when seawater [141] is normalized to NASC [101] (see upper image of Fig. 11) and/or to chondrite (see lower image of Fig. 11) exhibits a well-known negative Ce/Ce* (Ce^A). It has long been suggested that the negative Ce^A in seawater reflects the oxidation of soluble Ce^{3+} to insoluble Ce^{4+}, which can be then removed as Ce(OH)$_4$ [142, 143 and references

Fig. 9 Comparison of all the "Masuda-Coryell" diagrams for the Parnassos-Ghiona bauxites (the current study) showing the strong similarities between them (Color figure online)
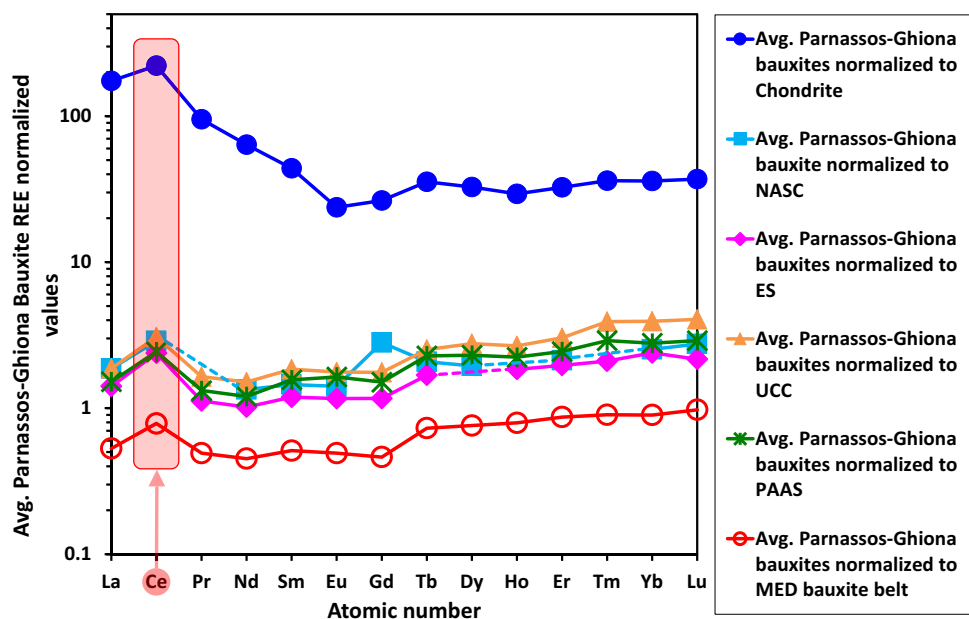
Fig. 10 REE abundances normalized to chondrite ([106–113]; upper image), to PAAS ([112, 125]; middle image), and to Mediterranean (MED) bauxite belt excluding Greek ones ([19, 20, 54–67]; lower image) for the Parnassos-Ghiona bauxites (the current study), as well as for all Greek bauxites (the current study and literature [27, 30, 31, 33–47, 68–70]). For the relevant literature, see also the "Materials and Methods" (Color figure online)
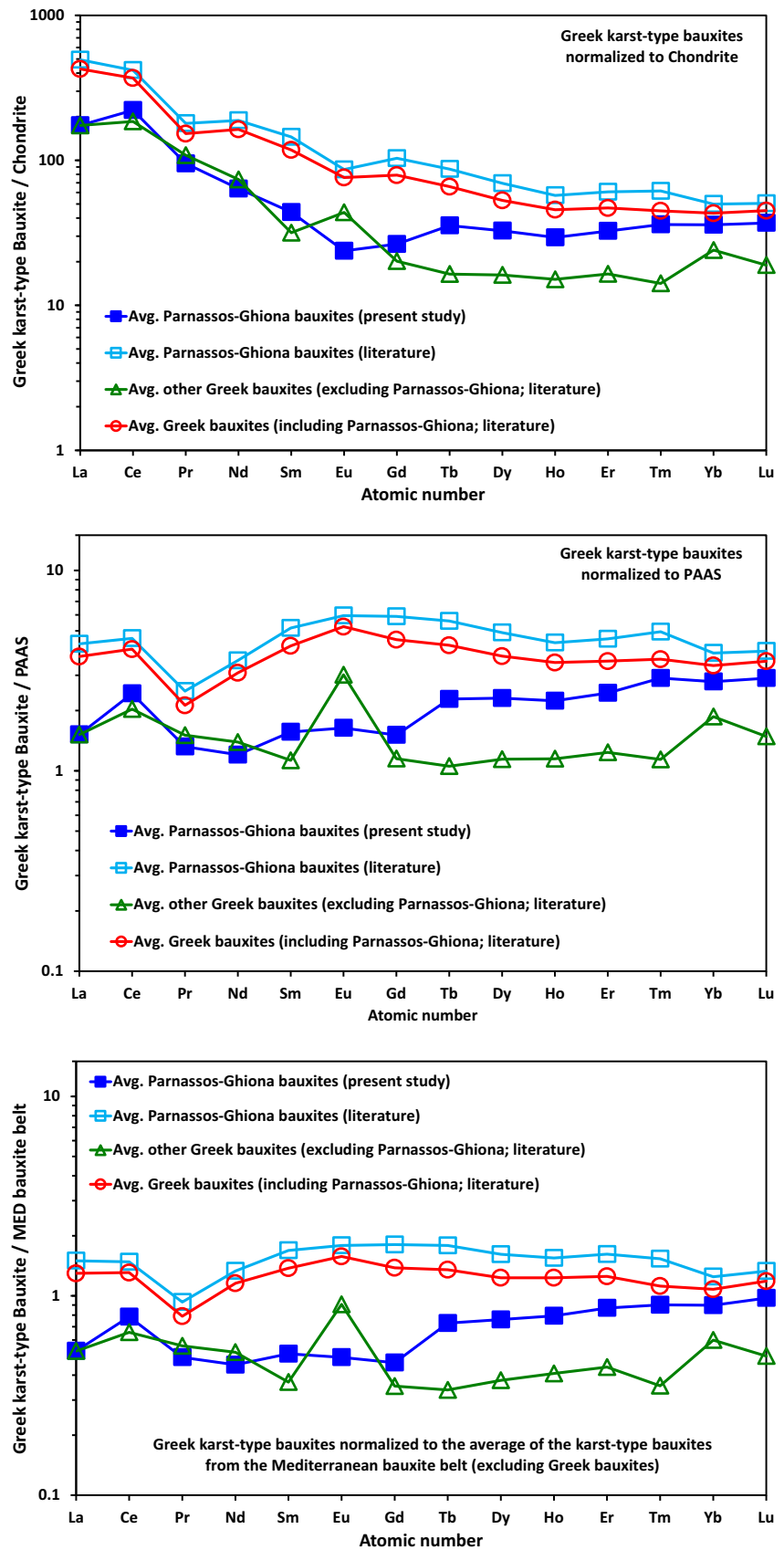
Fig. 11 Ce, Eu, and Gd anomalies (positive anomalies are highlighted by transparent light red color; negative anomalies are highlighted by transparent light green color) of the Parnassos-Ghiona bauxites (the current study) compared with the Ce, Eu, and Gd anomalies of various geological materials, such as granite [138, 139], Fe–Mn-nodules [128, 132, 133], Fe–Mn-crust [126–131], Brazilian lateritic bauxite [135], desert varnish [134], Bayan Obo REE deposit [11], and xenoliths [136], including seawater [141] (see inset image). All REE values have been normalized to NASC (except Pr, Ho, and Tm; [105]; see upper image) and, furthermore, to chondrite [106–113] (see lower image). A representative REE concentration from Greek bauxite metallurgical residue (the so-called Red Mud/RM) is illustrated for comparison purpose [23] (Color figure online)
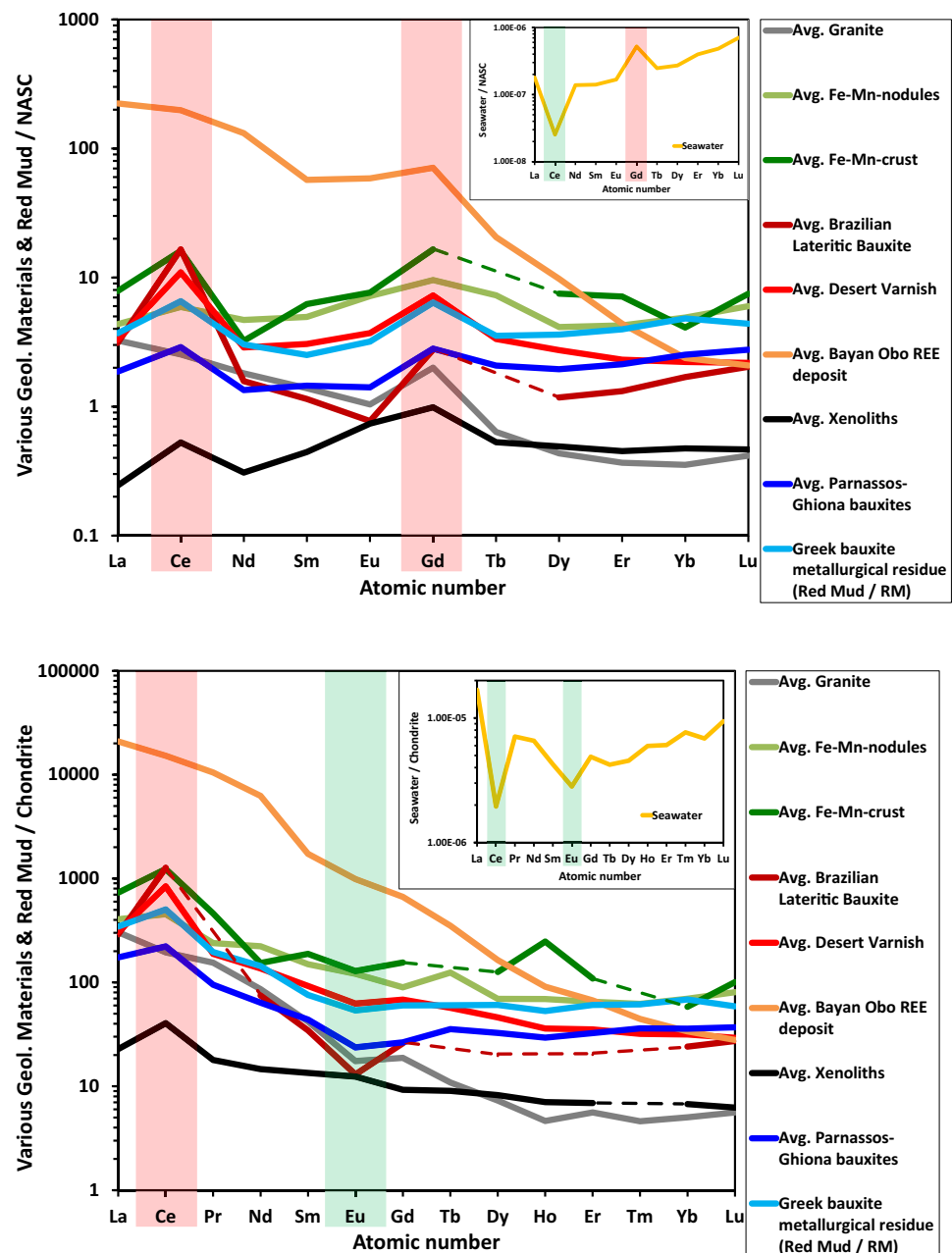
therein]). Besides, Ce^{4+} can be incorporated into deep-sea sediments, and preferentially, as mentioned, into Fe–Mn-nodules and Fe–Mn-crusts, exhibiting a characteristic positive Ce^A [126–133, 144] (see Fig. 11). Nevertheless, a strong positive Ce^A is also observed, in zircon crystals where Ce^{3+} substitutes in Zr^{4+} sites resulting in a charge deficiency [145]. In order to ensure that zircon maintains charge neutrality, incorporation of trivalent REE is thought to involve the so-called "xenotime" substitution ($Zr^{4+} + Si^{4+} \rightarrow REE^{3+} + P^{5+}$), requiring a pentavalent element like P^{5+} substituting for Si^{4+} [146 and references therein].

Finally, the REE concentration of Greek red mud [23] seems to be similar to that of Fe–Mn-oxyhydroxide desert varnish, following almost the same pattern, reaching the HREE values of Fe–Mn-nodules. Moreover, when the REE values of Parnassos-Ghiona bauxite (i.e., the Al-ore parent material for the production of alumina by the "Aluminium of Greece S.A.") are compared with the Greek red mud (final metallurgical residue of the company at its processing plant for Al metal production; see Supplementary Material; Fig. S1), they both exhibit similar trend, whereas a remarkable REE enrichment of the red mud by almost two times is observed (Fig. 11). This enrichment can be explained by the bulk absence of the Al-oxyhydroxide

phases (diaspore and/or boehmite that contain also some Fe and Cr but not REE [22]) from the Greek red mud [23], which are almost removed during the Bayer process. Thus, the remaining oxide phases in the red mud are relatively enriched in REE. Indeed, the presence of REEs in red mud is expected to be mainly in the form of oxides rather as fluorocarbonates existing in Parnassos-Ghiona bauxite (e.g., [23]). It is worthy to mention that the company ("Aluminium of Greece S.A.") uses a mixture of bauxite ores for its alumina production, such as a variety of karst-type bauxites from both the Parnassos-Ghiona mining area and from other bauxite mining localities around the globe. Nevertheless, karst-type bauxite ores from Parnassos-Ghiona mining area represent the larger proportion of that mixture.

The Case Study of Pera Lakkos Underground Mine

In the frame of the current study, a specific mining site situated into the Cretaceous upper bauxitic horizon (B3) was studied. In particular, the REE and the associated trace elements differential mobility as well as their distribution in-between the interstratified bauxitic, coal and carbonate layers along the profile, at the mining front of the Pera Lakkos active underground mine were geochemically investigated. In this case study, both typical Fe-rich and Fe-depleted bauxites, embedded between dark-to-black bituminous hanging wall limestone and the ordinary white footwall limestone, occur (see Supplementary Material; images b and c of Fig. S1 and Fig. S20). In addition, there are local intercalations of Fe-rich/sulfide-bearing bauxite into the Fe-depleted bauxitic domain [38, 39], overlaid by a rare Cretaceous coal layer with maximum thickness 35–40 cm (see Supplementary Material; Fig. S20; [52]). They are present as individual fragments at the uppermost part of the mining front situated beneath the contact between the thin layer of coal and the B3 bauxitic horizon ([51, 52]; see Supplementary Material; Fig. S20).

The bulk chemical compositions of dark (ALM0306_PL1_DLS2) to black (ALM0306_PL1_DLS1) bituminous hanging wall limestone and the ordinary white footwall limestone (ALM0306_PL1_WLS), as well as the composition of the coal (ALM0807_PL1_COAL) interstratified between the bauxite ore and the hanging wall limestone at Pera Lakkos underground mine are presented in Tables S5 and S6 (see Supplementary Material). For comparison purposes, the chemical composition of the flying ash of the coal (ALM0807_PL1_ASH) is also presented (see Supplementary Material; Table S6). The bulk chemical compositions (with regard to the trace elements budget) of the geological materials composing the Pera Lakkos, normalized to UCC [82], are presented in Fig. S21

(see Supplementary Material). It is obvious that both hanging wall and footwall limestones contain relatively low concentrations of trace elements. On the other hand, hanging wall limestone is slightly enriched in Sr, Mo, Se, Cd, whereas footwall limestone differs from the latter, as is relative depleted in Sr, and Mo comparing to UCC [82]. Spathi [147] who analyzed footwall limestones for Pb, Cr, Cu, Co, and Sr reported similar observation. It is noteworthy to mention that Fe-rich/sulfide-bearing bauxite are highly enriched in As, and Sb, less enriched in metals (such as Ni, V, Cr, Pb, Co, Sn, and Hg) and, also, in actinides (Th and U). These sulfur-bearing bauxitic fragments are relative enriched in Sc, Zr, Ti, Ta, Nb, and REE. Furthermore, comparing the UCC-normalized spider diagrams [82] of Fe-depleted and Fe-rich bauxites, significant enrichment and depletion in selected elements can be confirmed. Hence, Fe-depleted bauxite is depleted in As, Sm, and Eu. Additionally, both bauxitic types are enriched in Th, U, REE, and Ti, whereas are depleted in Pb. Moreover, the coal is highly enriched in Se, U, Mo, As, Sb, Ni, REE and Hg. Similar observations have been reported by Kalaitzidis et al. [52] for most of the elements, though there is no mention for elevated content of Se, REE and Hg. Moreover, the relevant flying ash, representing the "inorganic" part of the material, is exceptionally enriched in U, Mo, REE, Ni and Cr. That means that these elements—in either case—are concentrated in the above geological material.

According to the PXRD diagrams (not shown herein) the studied footwall and hanging wall limestones contain only calcite as major crystalline phase, whereas most of the trace elements must be associated to detrital and authigenic crystalline phases—revealed by SEM–EDS after acid dissolution of the carbonate part—such as chromite, magnetite, zircon, rutile, clays, goethite, and pyrite forming characteristic sedimentary framboids (see Supplementary Material; Figures S22 and S23). The presence of characteristic framboids and/or relevant pseudomorphs into the dark and black hanging wall limestones (see Supplementary Material; Fig. S23), along with the Fe-rich/sulfide-bearing fragments in the uppermost parts of the profile [38, 39] (see Supplementary Material; Fig. S20), indicates potential anoxic palaeo-environment and diagenetic/epigenetic depositional stage during the bauxitization [52].

The REE chondrite-normalized [106–113] diagrams for all geological materials for the Pera Lakkos profile are presented in Fig. S24 (see Supplementary Material). It is more than evident that there is a remarkable variation in the Ce/Ce* (Ce anomaly/Ce^A) from negative to positive values and back, declining from hanging wall limestones to coal and bauxites, toward the footwall limestone (Ce^A: 0.44 - > 0.49 - > 4.18 - > 1.70 - > 3.10 - > 1.18 - > 0.68). The Ce anomalies in marine limestones could indicate palaeo-redox conditions in palaeo-oceans, and particularly in Tethys

(e.g., [142]). According to the above authors, Tethyan middle-Triassic limestone in China yielded a Ce^A of 0.53 when U/Th ratio was found to be 2.6. In the case of the Parnassos-Ghiona B3 horizon Tethyan Cretaceous limestones, the hanging wall samples show Ce^A close to Chinese Triassic, but much higher U/Th ratios, in the range 11–20, and therefore Ce^A values should be carefully considered [142]. On the other hand, the footwall limestones exhibits $Ce^A = 0.68$ and low U/Th = 2. Regarding Fe-depleted and Fe-rich bauxite occurring in Pera Lakkos underground mine, it is also rather hard to conclude on the palaeo-redox conditions by using various redox-sensitive elements such as U, As, Mo and V, and geochemical parameters such as Ce/Ce*, U/Th and V/V + Ni (e.g., [138, 148, 149]; see Fig. 12). According to Mazumdar et al. [150] positive Ce^A in early Cambrian chert-phosphorite assemblages indicate anoxic palaeo-conditions. If this is true for Cretaceous bauxites, Ce must exist in

reduced state (Ce^{3+}); in fact, this growing claim is strongly supported by the current study of bauxites in microscale showing Ce^{3+} fluorocarbonate minerals (see text above). The precipitation of such phases in the karst-type bauxites also requires alkaline conditions [100]. Mongelli et al. [61] have also discussed about oxic–anoxic conditions in bauxites based on Ce^A, but for an open pit with periodic fluctuation of the groundwater table in an overall rising trend. Concerning the Pera Lakkos bauxite ore deposit, it is rather tricky to conclude whether precipitation of REE fluorocarbonates took place during diagenesis (when crystals of diaspore and/or boehmite together with primary Fe- and Ti-oxides were grown) or in the course of further supergene/epigenetic processes. Besides, the ΣREE value in the bauxite ore body of B3 horizon is profoundly increased from the Fe-depleted domain toward to the Fe-rich domain downward to the lowermost parts of the profile (Fig. 12). Nevertheless, it should be noted that the
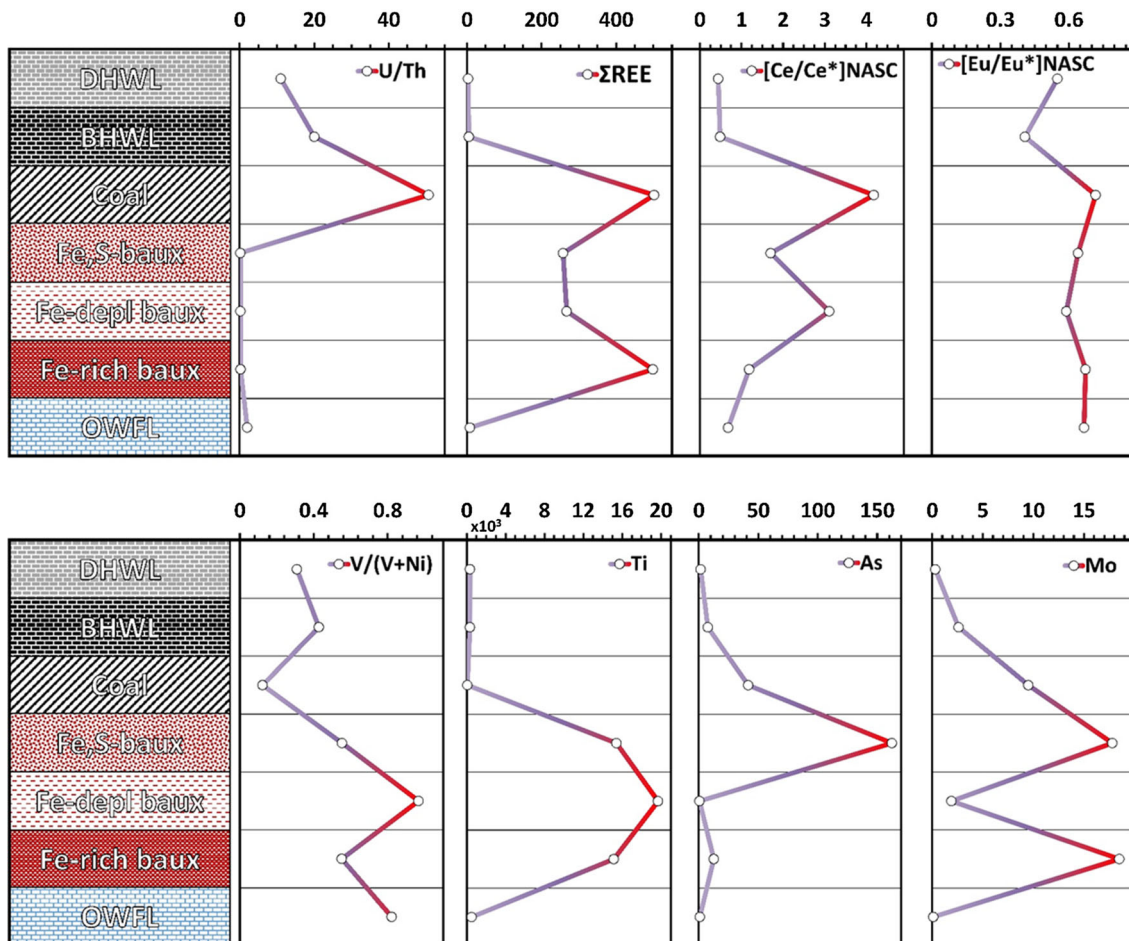

Fig. 12 Elemental and geochemical parameters in geological materials across the mining front of Pera Lakkos underground mine. From top to bottom: dark hanging wall limestone (DHWL); black hanging wall limestone (BHWL); coal layer (COAL); Fe-rich/sulfide-bearing bauxite (Fe, S-baux); Fe-depleted bauxite (Fe-depl baux); Fe-rich bauxite (Fe-rich baux); ordinary white footwall limestone (OWFL) (Color figure online)

enrichment of the studied bauxites of the Pera Lakkos underground mine in REE has been recorded in all mass of the ore body; thus, it is not necessarily related to the neighborhood of footwall limestone, where potential alkaline conditions (the so-called alkaline barrier after suggestion by Valeton et al. [85] and Skarpelis et al. [151]) might have occurred during that enrichment. Regarding the vertical distribution of REE in a characteristic deposit of the B3 horizon, it may be concluded that the $Ce/Ce*$ (Ce^A) is not high for the lowermost Fe-rich bauxite domain, but rather for the uppermost Fe-depleted domain and for the coal layer, possibly due to $Ce^{3+} \leftrightarrow Ce^{4+}$ and LREE re-mobilization during supergene/epigenetic processes.

Finally, it could be mentioned that the natural enrichment of the REE budget downward to the lowermost parts of the profile, that took place upon REE mobility under diagenetic or, even, supergene/epigenetic—acidic—conditions, can be explained by previous lab experiments concerning leachability and extraction of REE from karst-type bauxite from Parnassos-Ghiona mines [23, 24].

Conclusions

The main conclusions, concerning the REE—and associated trace elements—geochemistry in karst-type bauxites from the Parnassos-Ghiona mines (central Greece), are summarized below:

- Greek karst-type bauxites from Parnassos-Ghiona mines are relatively enriched in REE (avg. ΣREE + Y+Sc = 463 ppm) and particularly in LREE (avg. ΣLREE = 321 ppm; Ce = 193 ppm; avg. Nd = 41), whereas the HREE concentration is much lower. Together with REE, bauxites are also enriched in other HFSE (such as Th, U, Ta, Nb, Zr, and Hf), and in some compatible elements (such as Ni, V, and Cr), while they are characteristically depleted in LILE (Cs, Rb, and K). It should be noted that the REE potential of bauxites is much lower compared to that of Greek red mud (ΣREE + Y+Sc = 976 ppm; Ce = 439 ppm; Nd = 92 ppm).
- The REE occur mostly as authigenic/diagenetic $LREE^{3+}$ fluorocarbonate minerals, whereas Ce may also exist in the form of Ce^{4+} either in LREE-actinide oxides and/or epigenetically sorbed in Fe-oxides. Notably bauxites, along with Fe–Mn-oxyhydroxide desert varnish and Brazilian laterite, are among the terrestrial geological materials showing distinctively positive $Ce/Ce*$ (Ce^A) anomaly. This also stands for the Greek bauxite metallurgical residue, i.e., red mud.
- The REE concentrations are in line with new data concerning karst-type bauxites from Mediterranean

bauxite belt and published data about karst-type bauxites from the globe (Irano-Himalayan and East Asian bauxite belt). Besides, the REE values of Greek bauxite metallurgical residue (red mud) are remarkably increased by almost two times compared to those of Greek industrial bauxite, similar to those of Fe–Mn-oxyhydroxide desert varnish, reaching the HREE values of Fe–Mn-nodules. However, it should be mentioned that the REE potential is considerably lower in comparison with the current REE resources (REE-Fe-Nb-Th deposits or even carbonatites and peralkaline to agpaitic rocks containing REE in terms of thousand ppm—wt%—levels).
- The Sc concentration (avg. Sc = 47 ppm; occurring in scandian—detrital—zircons and possibly in Fe-oxides) is typical for Mediterranean and EU bauxites and laterites, but significantly lower compared to Australian Sc-bearing laterite deposits (containing 434 ppm) and lower than the concentration of Greek red mud (Sc = 114 ppm).
- Apart from Th that is present in REE fluorocarbonates, and Zr and Hf that are present in zircons, there are other trace elements associated to REEs. In particular, Pb and As are associated to Sc and also seem to be related to Fe-oxides (mostly in the case of Fe-rich samples where Fe-oxides are abundant). Concerning arsenic, Synchrotron-based data have indicated that it is mainly related to Fe–Ti-Cr pisoliths in the form of arsenates (As^{5+}), and not to sulfides in the form of As^{3+}. At the same time, Ga is not related to Fe-phases, but mostly to Al-phases, i.e., diaspore and/or boehmite.
- The Pera Lakkos bauxite mine case study showed that REE are concentrated mainly in the lowermost Fe-rich domain and also in the coal layer overlaying the deposit. However, it seems that supergene/epigenetic processes have re-mobilized LREE, and particularly Ce exhibiting a $Ce/Ce*$ (Ce^A) enrichment—except coal—in the uppermost Fe-depleted domain.

Compliance with Ethical Standards

Conflict of interest The authors state that there is no conflict of interest.

References

1. Arndt NT, Fontboté L, Hedenquist JW, Kesler SE, Thompson JFH, Wood DG (2017) Future global mineral resources. Geochem Perspect 6(1):1–171
2. Chakhmouradian AR, Smith MP, Kynicky J (2015) From "strategic" tungsten to "green" neodymium: a century of critical metals at a glance. Ore Geol Rev 64:455–458
3. Wall F, Rollat A, Pell RS (2017) Responsible sourcing of critical metals. Elements 13:313–318
4. Mathieux F, Ardente F, Bobba S, Nuss P, Blengini G, Alves Dias P, Blagoeva D, Torres De Matos C, Wittmer D, Pavel C, Hamor T, Saveyn H, Gawlik B, Orveillon G, Huygens D, Garbarino E, Tzimas E, Bouraoui F, Solar S (2017) Critical raw materials and the circular economy—background report. JRC Science-for-policy Report, EUR 28832 EN, Publications Office of the European Union, Luxembourg. ISBN: 978-92-79-74282-8. https://doi.org/10.2760/378123JRC108710
5. Binnemans K, Jones PT (2015) Rare earths and the balance problem. J Sustain Metall 1:29–38
6. Binnemans K, Jones PT, Müller T, Yurramendi L (2018) Rare earths and the balance problem. J Sustain Metall 4:126–146
7. British Geological Survey (2015) Supply risk list for chemical elements or element groups, which are of economic value. www.bgs.ac.uk/downloads/start.cfm?id=3075
8. Hatch GP (2012) Dynamics in the global market for rare earths. Elements 8:341–346
9. Jordens A, Cheng YP, Waters KE (2013) A review of the beneficiation of rare earth element bearing minerals. Min. Engineer 41:97–114
10. Kanazawa Y, Kamitani M (2006) Rare earth minerals and resources in the world. J Alloys Compd 408–412:1339–1343
11. Ling M-X, Liu Y-L, Williams IS, Teng F-Z, Yang X-Y, Ding X, Wei G-J, Xie L-H, Deng W-F, Sun W-D (2013) Formation of the world's largest REE deposit through protracted fluxing of carbonatite by subduction-derived fluids. Sci Rep 3(1776):1–8
12. Smith MP, Moore K, Kavecsánszki D, Finch AA, Kynicky J, Wall F (2016) From mantle to critical zone: a review of large and giant sized deposits of the rare earth elements. Geochem Front 7:315–334
13. Steenfelt A, Kolb J, Thrane K (2016) Metallogeny of South Greenland: a review of geological evolution, mineral occurrences and geochemical exploration data. Ore Geol Rev 77:194–245
14. Kato Y, Fujinaga K, Nakamura K, Takaya Y, Kitamura K, Ohta J, Toda R, Nakashima T, Iwamori H (2013) Deep-sea mud in the Pacific Ocean as a potential resource for rare-earth elements. Nat Geosci 4:535–539
15. Takaya Y, Yasukawa K, Kawasaki T, Fujinaga K, Ohta J, Usui Y, Nakamura K, Kimura J-I, Chang Q, Hamada M, Dodbiba G, Nozaki T, Iijima K, Morisawa T, Kuwahara T, Ishida Y, Ichimura T, Kitazume M, Fujita T, Kato Y (2018) The tremendous potential of deep sea mud as a source of rare-earth elements. Sci Rep 8(5763):1–8
16. Mancheri NA (2015) World trade in rare earths, Chinese export restrictions, and implications. Resour Policy 46:262–271
17. Deady EA, Mouchos E, Goodenouch K, Willianson BJ, Wall F (2016) A review of the potential for rare-earth element resources from European red muds: examples from Seydişehir, Turkey and Parnassus-Giona. Greece. Min Mag 80(1):43–61
18. Goodenough KM, Schilling J, Jonsson E, Kalvig P, Charles N, Tuduri J, Deady EA, Sadeghi M, Schiellerup H, Müller A, Bertrand G, Arvanitidis N, Eliopoulos DG, Shaw RA, Thrane K, Keulen N (2016) Europe's rare earth element resource potential: an overview of REE metallogenetic provinces and their geodynamic setting. Ore Geol Rev 72:838–856
19. Mongelli G, Boni M, Oggiano G, Mameli P, Sinisi R, Buccione R, Mondillo N (2017) Critical metals distribution in Tethyan karst bauxite: the cretaceous Italian ores. Ore Geol Rev 86:526–536
20. Radusinović S, Jelenković R, Pačevski A, Simić V, Božović D, Holclajtner-Antunović I, Životić D (2017) Content and mode of occurrences of rare earth elements in the Zagrad karstic bauxite deposit (Nikšić area, Montenegro). Ore Geol Rev 80:406–428
21. U.S. Geological Survey (2018) Bauxite and alumina, statistics and information. http://minerals.usgs.gov/minerals/pubs/commodity/bauxite
22. Gamaletsos PN, Godelitsas A, Kasama T, Church NS, Douvalis AP, Göttlicher J, Steininger R, Boubnov A, Pontikes Y, Tzamos E, Bakas T, Filippidis A (2017) Nano-mineralogy and -geochemistry of high-grade diasporic karst-type bauxite from Parnassos-Ghiona mines, Greece. Ore Geol Rev 84:228–244
23. Gamaletsos PN, Godelitsas A, Kasama T, Kuzmin A, Lagos M, Mertzimekis TJ, Göttlicher J, Steininger R, Xanthos S, Pontikes Y, Angelopoulos GN, Zarkadas C, Komelkov A, Tzamos E, Filippidis A (2016) The role of nano-perovskite in the negligible thorium release in seawater from Greek bauxite residue (red mud). Sci Rep 6(21737):1–13
24. Mouchos E, Wall F, Williamson BJ, Palumbo-Roe B (2016) Easily leachable rare earth element phases in the Parnassos-Ghiona bauxite deposits, Greece. Bull Geol Soc Greece 50(4):1952–1958
25. Gamaletsos P (2014) Mineralogy and geochemistry of bauxites from Parnassos-Ghiona mines and the impact on the origin of the deposits. Unpublished PhD thesis. National and Kapodistrian University of Athens, Athens, pp 1–361. http://hdl.handle.net/10442/hedi/42199
26. Gamaletsos P, Godelitsas A, Mertzimekis TJ, Göttlicher J, Steininger R, Xanthos S, Berndt J, Klemme S, Kuzmin A, Bárdossy G (2011) Thorium partitioning in Greek industrial bauxite investigated by synchrotron radiation and laser-ablation techniques. Nucl Instrum Methods Phys Res B 269:3067–3073
27. Laskou M, Andreou G (2003) Rare earth element distribution and REE-minerals from the Parnassos-Ghiona bauxite deposits, Greece. In: Eliopoulos D et al (eds) Mineral exploration and sustainable development: proceedings of the 7th biennial SGA-SEG meeting 2003, Athens, Greece, 24–28 August 2003.

Millpress, Rotterdam, The Netherlands, pp 89–92. ISBN: 90-77017-77-1

28. Mouchos E, Wall F, Williamson B (2017) High-Ce REE minerals in the Parnassus-Giona bauxite deposits, Greece. Appl Earth Sci 126:82–83

29. Ochsenkühn-Petropoulou M, Ochsenkühn KM (1995) Rare earth minerals found in Greek Bauxites by SEM and EPMA. Eur Microsc Anal 49:13–14

30. Papastavrou S, Perdikatsis V (1987) U-Th and REE concentrations in bauxites and new aspects about the origin of bauxites in the Iti-mountains (C. Greece). In: Janković S (ed) Mineral deposits of the Tethyan Eurasian Metallogenic Belt between the Alps and the Pamirs. UNESCO/IGCP Project No 169: Geotectonic Evolution and Metallogeny of Mediterranean and SW Asia Department of Mineral Exploration, Faculty of Mining and Geology, Belgrade University, Belgrade, pp 111–118

31. Vind J, Malfliet A, Blanpain B, Tsakiridis PE, Tkaczyk AH, Vassiliadou V, Panias D (2018) Rare earth element phases in bauxite residue. Minerals 8(77):1–32

32. Vind J, Malfliet A, Bonomi C, Paiste P, Sajó IE, Blanpain B, Tkaczyk AH, Vassiliadou V, Panias D (2018) Rare earth element phases in bauxite residue. Miner Eng 123:35–38

33. Arp T (1985) Geologische Kartierung des Gebietes um Tithronion im Kallidromongebirge, Mittelgriechenland und petrographische Bearbeitung des Karstbauxites (b1). Unpublished PhD thesis. University of Hamburg, Hamburg, pp 1–213

34. Biermann M (1983) Zur mineralogie, geochemie und genese des karstbauxites (B3 – horizont) an der Grenze Unter-Oberkreide in Mittelgriechenland: Unpublished PhD thesis. University of Hamburg, Hamburg, pp 1–134

35. Eliopoulos DG, Economou-Eliopoulos M (2010) Arsenic distribution in laterite deposits of the Balkan Peninsula. In: Proceedings of XIX congress of the Carpathian Balkan Geological Association, Greece, 23–26 September 2010, vol 100. Scientific Annals, School of Geology, Aristotle University of Thessaloniki, pp 325–332

36. Laskou M (1991) Concentrations of rare earths in Greek bauxites. Acta Geol Hung 34:395–404

37. Laskou M (2001) Chromite in karst bauxites, bauxitic laterites and bauxitic clays of Greece. In: Piestrzyński A et al (eds) Mineral deposits at the beginning of the 21st century, Proceedings of the 6th Biennial SGA-SEG Meeting 2001, Krakow, Poland, 26–29 August 2001. Swets & Zeitlingen Publishers, Lisse, pp 1091–1094. ISBN: 90-2651-846-3

38. Laskou M, Economou-Eliopoulos M (2007) The role of microorganisms on the mineralogical and geochemical characteristics of the Parnassos-Ghiona bauxite deposits, Greece. J Geochem Explor 93:67–77

39. Laskou M, Economou-Eliopoulos M (2013) Bio-mineralization and potential biogeochemical processes in bauxite deposits: genetic and ore quality significance. Miner Petrol 107:471–486

40. Laskou M, Economou-Eliopoulos M, Mitsis I (2011) Bauxite ore as an energy source for bacteria driving iron-leaching and bio-mineralization. Hell J Geosci 45:163–173

41. Maksimović Z, Papastamatiou J (1973) Distribution d'oligoélements dans les gisements de bauxite de la Grèce centrale. Symp. ICSOBA, Nice, pp 33–46

42. Ochsenkühn KM, Parissakis G (1977) Quantitative Untersuchungen von Bauxiten Zentralgriechenlands mittels Atomabosrptionsspectroscopie und Flemmenatomemission. Microchim Acta 1:447–457

43. Ochsenkühn-Petropulu M, Lyberopulu Th, Parissakis G (1995) Selective separation and determination of scandium from yttrium and lanthanides in red mud by a combined ion exchange/solvent extraction method. Anal Chim Acta 315(1–2):231–237

44. Ochsenkühn-Petropoulou M, Ochsenkühn KM, Luck J (1991) Comparison of inductively coupled plasma mass spectrometry with inductively coupled plasma atomic emission spectrometry and instrumental neutron activation analysis for the determination of rare earth elements in Greek bauxites. Spectrochim Acta 46:51–65

45. Ochsenkühn-Petropulu M, Lyberopulu Th, Parissakis G (1994) Direct determination of lanthanides, yttrium and scandium in bauxites and red mud from alumina production. Anal Chim Acta 296(3):305–313

46. Papassiopi N, Vaxevanidou K, Paspaliaris I (2010) Effectiveness of iron reducing bacteria for the removal of iron from bauxite ores. Miner Eng 23:25–31

47. Retzmann K (1986) Zur mineralogie, geochemie und genese des karstbauxites (B2-horizont) an der Grenze Jura/Kreide in Mittelgriechenland. Unpublished PhD thesis. University of Hamburg, Hamburg, pp 11–146

48. Marquis EA, Seidman DN, Dunand DC (2002) Creep of precipitation-strengthened Al(Sc) alloys. In: Mishra RS, Earthman JC, Raj SV (eds) Creep deformation: fundamentals and applications. TMS Annual Meeting, Seattle, Washington, 17–21 February 2002, pp 299–308

49. Bárdossy G (1982) Karst bauxites: bauxite deposits on carbonate rocks: Developments in Economic Geology 14. Elsevier, Amsterdam, pp 1–441

50. Valeton I (1972) Bauxites. Elsevier, Amsterdam, pp 1–226

51. Gamaletsos P, Godelitsas A, Dotsika E, Tzamos E, Göttlicher J, Filippidis A (2013) Geological sources of As in the environment of Greece: a review. In: Scozzari A, Dotsika E (eds) The volume "Threats to the quality of groundwater resources: prevention and control". Springer's review series "The handbook of environmental chemistry", pp 77–113. https://doi.org/10.1007/698_2013_230

52. Kalaitzidis S, Siavalas G, Skarpelis N, Araujo CV, Christanis K (2010) Late Cretaceous coal overlying karstic bauxite deposits in the Parnassus-Ghiona unit, Central Greece: coal characteristics and depositional environment. Int J Coal Geol 81:211–226

53. Jarosewich E, Boatner LA (1991) Rare earth element reference samples for electron microprobe analyses. Geostand Newsl 15:397–399

54. Özlü N (1983) Trace-element content of "karst bauxites" and their parent rocks in the Mediterranean belt. Miner Depos 18:469–476

55. Boni M, Rollinson G, Mondillo N, Balassone G, Santoro L (2013) Quantitative mineralogical characterization of karst bauxite deposits in the southern Apennines, Italy. Econ Geol 108:813–833

56. Buccione R, Mongelli G, Sinisi R, Boni M (2016) Relationship between geometric parameters and compositional data: a new approach to karst bauxites exploration. J Geochem Explor 169:192–201

57. MacLean WH, Bonavia FF, Sanna G (1997) Argillite debris converted to bauxite during karst weathering: evidence from immobile element geochemistry at the Olmedo Deposit, Sardinia. Miner Depos 32:607–616

58. Mameli P, Mongelli G, Oggiano G, Dinelli E (2007) Geological, geochemical and mineralogical features of some bauxite deposits from Nurra (Western Sardinia, Italy): insights on conditions of formation and parental affinity. Int J Earth Sci (Geol Rundsch) 96:887–902

59. Mondillo N, Balassone G, Boni M, Rollinson G (2011) Karst bauxites in the Campania Apennines (southern Italy): a new approach. Period Miner 80(3):407–432

60. Mongelli G (1997) Ce-anomalies in the textural components of Upper Cretaceous karst bauxites from the Apulian carbonate platform (southern Italy). Chem Geol 140:69–76

61. Mongelli G, Boni M, Buccione R, Sinisi R (2014) Geochemistry of the Apulian karst bauxites (southern Italy): chemical fractionation and parental affinities. Ore Geol Rev 63:9–21

62. Mongelli G, Buccione R, Sinisi P (2015) Genesis of autochthonous and allochthonous Apulian karst bauxites (Southern Italy): climate constraints. Sediment Geol 325:168–176

63. Mongelli G, Buccione R, Gueguen E, Langone A, Sinisi R (2016) Geochemistry of the apulian allochthonous karst bauxite, Southern Italy: distribution of critical elements and constraints on Late Cretaceous Peri-Tethyan palaeogeography. Ore Geol Rev 77:246–259

64. Putzolu F, Papa AP, Mondillo N, Boni M, Balassone G, Mormone A (2018) Geochemical characterization of bauxite deposits from the Abruzzi Mining District (Italy). Minerals 8(298):1–24

65. Hanilçi N (2013) Geological and geochemical evolution of the Bolkardaği bauxite deposits, Karaman, Turkey: transformation from shale to bauxite. J Geochem Explor 133:118–137

66. Karadağ MM, Küpeli Ş, Arýk F, Ayhan A, Zedef V, Döyen A (2009) Rare earth element (REE) geochemistry and genetic implications of the Mortaş bauxite deposit (Seydişehir/Konya—southern Turkey). Chemie Erde 69:143–159

67. Öztürk H, Hein JR, Hanilçi N (2002) Genesis of the Doğankuzu and Mortaş bauxite deposits, Taurides, Turkey: separation of Al, Fe, and Mn and implications for passive margin metallogeny. Econ Geol 97:1063–1077

68. Papastamatiou J, Maksimovic Z (1970) Contribution to the study of genesis of Greek bauxites: chemical and mineralogical composition of Mandra II bauxite deposits. Ann Inst Geol Publ Hung 3:391–402

69. Kiskyras D (1960) Die mineralogische Zusammensetzung der griechischen Bauxite in Abhängigkeit von der Tektonik. J Mineral Geochem (Former: Neues Jahrb Mineral Abhandl) 94:662–680

70. Laskou M, Economou M (1991) Platinum group elements and gold concentrations in Greek bauxites. Geol Balcan 21:65–77

71. Gamaletsos P, Godelitsas A, Chatzitheodoridis E, Kostopoulos D (2007) Laser micro-Raman investigation of Greek bauxites from the Parnassos-Ghiona active mining area. Bull Geol Soc Greece 40:736–746

72. Perdikatsis V (1992) Quantitative mineralogical analysis of bauxites by X-ray diffraction with the Rietveld method. Acta Geol Hung 35:447–457

73. Grice JD, Maisonneuve V, Leblanc M (2007) Natural and synthetic fluoride carbonates. Chem Rev 107:114–132

74. Maksimović Z, Pantó G (1991) Contribution to the geochemistry of the rare earth elements in the karst-bauxite deposits of Yugoslavia and Greece. Geoderma 51:93–109

75. Maksimović Z, Pantó G (1996) Authigenic rare earth minerals in karst-bauxites and karstic nickel deposits. In: Jones AP, Wall F, Williams CT (eds) Rare earth minerals: Chemistry, origin and ore deposits. Chapman & Hill, London, pp 257–279

76. Moëlo Y, Lulzac Y, Rouer O, Palvadeau P, Gloaguen É, Léone P (2002) Scandium mineralogy: pretulite with scandian zircon and zenotime-(Y) within an apatite-rich oolitic ironstone from Saint-Aubin-Des-Châteaux, Armorican massif, France. Can Mineral 40:1657–1673

77. Breiter K, Förster H-J, Škoda R (2006) Extreme P-, Bi-, Nb-, Sc-, U- and F-rich zircon from fractionated perphosphorous granites: the peraluminous Podlesí granite system, Czech Republic. Lithos 88:15–34

78. Gramaccioli CM, Diella V, Demartin F (2000) The formation of scandium minerals as an example of the role of complexes in the geochemistry of rare earths and HFS elements. Eur J Mineral 12:795–808

79. Goldstein J, Newbury DE, Joy DC, Lyman CE, Echlin P, Lifshin E, Sawyer L, Michael JR (2003) Scanning electron microscopy and X-ray microanalysis, 3rd edn. Springer, New York, pp 1–689. https://doi.org/10.1007/978-1-4615-0215-9

80. Goldstein J, Newbury DE, Michael JR, Ritchie NWM, Scott JHJ, Joy DC (2018) Scanning electron microscopy and X-ray microanalysis, 4th edn. Springer, New York, pp 1–550. https://doi.org/10.1007/978-1-4939-6676-9

81. Chassé M, Griffin WL, O'Reilly SY, Calas G (2016) Scandium speciation in a world-class lateritic deposit. Geochem Perspect 3:105–114

82. Rudnick R, Gao S (2003) Composition of the continental crust. In: Holland HD, Turekian KK (eds) Treatise on geochemistry, vol 3. Elsevier–Pergamon, Oxford, pp 1–64

83. Ostergren JD, Bargar JR, Brown GE Jr, Parks GA (1999) Combined EXAFS and FTIR investigation of sulfate and carbonate effects on Pb(ll) sorption to goethite (α-FeOOH). J Synchrotron Radiat 6:645–647

84. O'Reilly SE, Hochella MF Jr (2003) Lead sorption efficiencies of natural and synthetic Mn and Fe-oxides. Geochim Cosmochim Acta 67(23):4471–4487

85. Valeton I, Biermann M, Reche R, Rosenberg F (1987) Genesis of nickel laterites and bauxites in Greece during the Jurassic and the Cretaceous and their relation to ultrabasic rocks. Ore Geol Rev 2:359–404

86. Valeton I (1994) Element concentration and formation of ore deposits by weathering. CATENA 21:99–129

87. Mudd GM, Jowitt SM, Werner TT (2017) The world's by-product and critical metal resources part I: uncertainties, current reporting practices, implications and grounds for optimism. Ore Geol Rev 86:924–938

88. Burke IT, Peacock CL, Lockwood CL, Stewart DI, Mortimer RJG, Ward MB, Renforth P, Gruiz K, Mayes WM (2013) Behavior of aluminum, arsenic and vanadium during the neutralization of red mud leachate by HCl, gypsum, or seawater. Environ Sci Technol 47:6527–6535

89. Abedini A, Calagari AA, Azizi MR (2018) The tetrad-effect in rare earth elements distribution patterns of titanium-rich bauxites: evidence from the Kanigorgeh deposit, NW Iran. J Geochem Explor 186:129–142

90. Calagari AA, Abenini A (2007) Geochemical investigations on Permo-Triassic bauxite horizon at Kanisheeteh, east of Bukan, West-Azarbaidjan, Iran. J Geochem Explor 94:1–18

91. Khosravi M, Abedini A, Alipour S, Mongelli G (2017) The Darzi-Vali bauxite deposit, West-Azarbaidjan Province, Iran: critical metals distribution and parental affinities. J Afr Earth Sci 129:960–972

92. Ahmadnejad F, Zamanian H, Taghipour B, Zarasvandi A, Buccione R, Ellahi SS (2017) Mineralogical and geochemical evolution of the Bidgol bauxite deposit, Zagros Mountain Belt, Iran: implications for ore genesis, rare earth elements fractionation and parental affinity. Ore Geol Rev 86:755–783

93. Rafiei B, Mollai H, Ghorbani M (2008) The genesis of Late Triassic allochthonous karst-type bauxite deposits of the Kisejin area, Ab-e-Garm district, Iran. N Jb Geol Paläont Abh 250(2):217–231

94. Zamanian H, Ahmadnejad F, Zarasvandi A (2016) Mineralogical and geochemical investigations of the Mombi bauxite deposit, Zagros Mountains, Iran. Chem Erde Geochem 76:13–37

95. Zarasvandi A, Charchi A, Carranza EJM, Alizadeh B (2008) Karst bauxite deposits in the Zagros Mountain Belt, Iran. Ore Geol Rev 34:521–532

96. Esmaeily D, Rahimpour-Bonab H, Esna-Ashari A, Kananian A (2010) Petrography and geochemistry of the Jajarm karst bauxite ore deposit, NE Iran: implications for source rock material and ore genesis. Turk J Earth Sci 19:267–284

97. Zarasvandi A, Carranza EJM, Ellahi SS (2012) Geological, geochemical, and mineralogical characteristics of the Mandan and Deh-now bauxite deposits, Zagros Fold Belt, Iran. Ore Geol Rev 48:125–138

98. Liu X, Wang Q, Deng J, Zhang Q, Sun S, Meng J (2010) Mineralogical and geochemical investigations of the Dajia Salento-type bauxite deposits, western Guangxi, China. J Geochem Explor 105:137–152

99. Liu X, Wang Q, Zhang Q, Zhang Y, Li Y (2016) Genesis of REE minerals in the karstic bauxite in western Guangxi, China, and its constraints on the deposit formation conditions. Ore Geol Rev 75:100–115

100. Wang Q, Deng J, Liu X, Zhang Q, Sun S, Jiang C, Zhou F (2010) Discovery of the REE minerals and its geological significance in the Quyang bauxite deposit, West Guangxi, China. J Asian Earth Sci 39:701–712

101. Li Z, Din J, Liao C, Yin F, LǔT, Cheng L, Li J (2013) Discovery of the REE minerals in the Wulong-Nanchuan bauxite deposits, Chongqing, China: insights on conditions of formation and processes. J Geochem Explor 133:88–102

102. Liu X, Wang Q, Feng Y, Li Z, Cai S (2013) Genesis of the Guangou karstic bauxite deposit in western Henan, China. Ore Geol Rev 55:162–185

103. Wang Q, Liu X, Yan C, Cai S, Li Z, Wang Y, Zhao J, Li G (2012) Mineralogical and geochemical studies of boron-rich bauxite ore deposits in the Songqi region, SW Henan, China. Ore Geol Rev 48:258–270

104. Ling K-Y, Zhu X-Q, Tang H-S, Wang Z-G, Yan H-W, Han T, Chen W-Y (2015) Mineralogical characteristics of the karstic bauxite deposits in the Xiuwen ore belt, Central Guizhou Province, Southwest China. Ore Geol Rev 65:84–96

105. Gromet LP, Dymek RF, Haskin LA, Korotev RL (1984) The "North American shale composite": its compilation, major and trace element characteristics. Geochim Cosmochim Acta 48:2469–2482

106. Boynton WV (1985) Cosmochemistry of the rare earth elements: Meteorite studies, In: Henderson P (ed) Rare earth element geochemistry. Developments in geochemistry, vol 2, Elsevier, Amsterdam, pp 115–152

107. Haskin LA, Haskin MA, Frey FA, Wildman TR (1968) Relative and absolute terrestrial abundances of the rare earths. In: Ahrens LH (ed) Origin and distribution of the elements, vol 1. Pergamon, Oxford, pp 889–911

108. Haskin LA, Wildeman TR, Haskin MA (1968) An accurate procedure for the determination of the rare earths by neutron activation. J Radioanal Chem 1:337–348

109. Haskin LA, Helmke PA, Paster TP, Allen RO (1971) Rare earths in meteoritic, terrestrial, and lunar matter. In: Brunfelt A, Steinnes E (eds) Activation analysis in geochemistry and cosmochemistry. Universitetsforlaget, Oslo, Proc. NATO Conf. on Activation Analysis in Geochemistry, pp 201–218

110. Korotev RL (1996) A self-consistent compilation of elemental concentration data for 93 geochemical reference samples. Geostand Newsl 20:217–245

111. Korotev RL (1996) On the relationship between the Apollo 16 ancient regolith breccias and feldspathic fragmental breccias, and the composition of the prebasin crust in the Central Highlands of the Moon. Meteor Planet Sci 31:403–412

112. Taylor SR, McClennan SM (1985) The continental crust: Its composition and evolution. Blackwell, Oxford, pp 1–312

113. Wakita H, Rey P, Schmitt RA (1971) Elemental abundances of major, minor, and trace elements in Apollo 11 lunar rocks, soil and core samples. In: Proceedings of the Apollo 11 lunar science conference, pp 1685–1717

114. Rollinson H (1993) Using geochemical data; evaluation, presentation, interpretation. Pearson Education Limited, Great Britain, pp 1–352. ISBN: 9-780582-067011

115. Anders E, Grevesse N (1989) Abundances of the elements: meteoritic and solar. Geochim Cosmochim Acta 53:197–214

116. Anders E, Ebihara M (1982) Solar-system abundances of the elements. Geochim Cosmochim Acta 46:2363–2380

117. Evensen NM, Hamilton PJ, O'Nions RK (1978) Rare-earth abundances in chondritic meteorites. Geochim Cosmochim Acta 42:1199–1212

118. Laul JC (1979) Neutron activation analysis of geologic materials. At Energy Rev 17:603–695

119. Masuda A, Nakamura N, Tanaka T (1973) Fine structure of mutually normalized rare-earth patterns of chondrites. Geochim Cosmochim Acta 37:239–248

120. McDonough WF, Sun S-S (1995) Composition of the Earth. Chem Geol 120:223–253

121. Nakamura N (1974) Determination of REE, Ba, Fe, Mg, Na, and K in carbonaceous and ordinary chondrites. Geochim Cosmochim Acta 38:757–775

122. Palme H (1988) Chemical abundances in meteorites. In: Klare G (ed) Reviews in modern astronomy. Springer, Berlin, pp 28–51

123. Korotev RL (2010) "Rare Earth Plots" and the concentrations of rare earth elements (REE) in chondritic meteorites. http://meteorites.wustl.edu/goodstuff/ree-chon.htm. Accessed Feb 2010

124. Haskin MA, Haskin LA (1966) Rare earths in European shales: a redetermination. Science 154:507–509

125. McClennan SM (1989) Rare earth elements in sedimentary rocks: influence of provenance and sedimentary processes. In: Lipin BR, McKay GA (eds) Geochemistry and mineralogy of rare earth elements. Reviews in Mineralogy, vol 21, Mineralogical Society of America, Washington, DC, pp 169–200

126. Aplin AC (1984) Rare earth element geochemistry of Central Pacific ferromanganese encrustations. Earth Planet Sci Lett 71:13–22

127. De Carlo EH, McMurtry GM (1992) Rare earth element geochemistry of ferromanganese crusts from the Hawaiian archipelago, Central Pacific. Chem Geol 95:235–250

128. Elderfield H, Graves MJ (1981) Negative cerium anomalies in the rare earth element patterns of oceanic ferromanganese nodules. Earth Planet Sci Lett 55:163–170

129. Hein JR, Koschinsky A, Bau M, Manheim FT, Kang JK, Roberts L (2000) Cobalt rich ferromanganese crusts in the Pacific. In: Cronan DS (ed) Handbook of marine mineral deposits. CRC Press NY, Mar Sci Ser, pp 239–280

130. Rajani RP, Banakar VK, Parthiban G, Mudholkar AV, Chodankar AR (2005) Compositional variation and genesis of ferromanganese crusts of the Afanasiy-Nikitin Seamount, Equatorial Indian Ocean. J Earth Syst Sci 114(1):51–61

131. Wen X, De Carlo EH, Li YH (1997) Interelement relation-ship in ferromanganese crusts from the Central Pacific Ocean. Their implications for crust genesis. Mar Geol 136:277–297

132. Ohta A, Ishii S, Sakakibara M, Mizuno A, Kawabe I (1999) Systematic correlation of the Ce anomaly with the Co/(Ni + Cu) ratio and Y fractionation from Ho in distinct types of Pacific deep-sea nodules. Geochem J 33:399–417

133. Piper DZ (1974) Rare earth elements in ferromanganese nodules and other marine phases. Geochim Cosmochim Acta 38:1007–1022

134. Thiagarajan N, Aeolus Lee C-T (2004) Trace-element evidence for the origin of desert varnish by direct aqueous atmospheric deposition. Earth Planet Sci Lett 224:131–141

135. Boulangé B, Colin F (1994) Rare earth element mobility during conversion of nepheline syenite into lateritic bauxite at Passa Quatro, Minais Gerais, Brazil. Appl Geochem 9:701–711

136. Zou H, McKeegan KD, Xu X, Zindler A (2004) Fe–Al-rich tridymite-hercynite xenoliths with positive cerium anomalies: preserved lateritic paleosols and implications for Miocene climate. Chem Geol 207:101–116

137. Chakhmouradian AR, Zaitsev AN (2012) Rare earth mineralization in igneous rocks: sources and processes. Elements 8:347–353

138. Mason B, Moore CB (1982) Principles of geochemistry. Wiley, New York, pp 1–344. ISBN: 0-471-57522-4

139. Krauskopf KB, Bird DK (1994) Introduction to geochemistry. McGraw-Hill International Editions, New York, pp 1–667. ISBN: 0-07-035820-6

140. German CR, Elderfield H (1990) Application of the Ce anomaly as a paleoredox indicator: the ground rules. Paleoceanography 5:823–833

141. Li Y-H (1991) Distribution patterns of the elements in the ocean: a synthesis. Geochim Cosmochim Acta 55:3223–3240

142. Liu Y-G, Miah MRU, Schmitt RA (1988) Cerium: a chemical tracer for paleo-oceanic redox conditions. Geochim Cosmochim Acta 52:1361–1371

143. Piepgras DJ, Jacobsen SB (1992) The behavior of rare earth elements in seawater: precise determination of variations in the North Pacific water column. Geochim Cosmochim Acta 56:1851–1862

144. Murphy K, Dymond J (1984) Rare earth elements fluxes and geochemical budget in the eastern equatorial Pacific. Nature 307:444–447

145. Grimes CB, John BE, Kelemen PB, Mazdab FK, Wooden JL, Cheadle MJ, Hanghøj K, Schwartz JJ (2007) Trace element chemistry of zircons from oceanic crust: a method for distinguishing detrital zircon provenance. Geology 35(7):643–646

146. Hanchar JM, Van Wenstrenen W (2007) Rare earth element behavior in zircon-melt systems. Elements 3:37–42

147. Spathi A (1972) Distribution of trace elements in the bauxite bearing limestones of the Parnassos-Ghiona area. Bull Geol Soc Greece 9(2):177–205

148. Hatch JR, Leventhal JS (1992) Relationship between inferred redox potential of the depositional environment and geochemistry of the Upper Pennsylvanian (Missourian) Stark Shale Member of the Dennis Limestone, Wabaunsee County, Kansas, U.S.A. Chem Geol 99:65–82

149. Jones B, Manning DAC (1994) Comparison of geochemical indices used for the interpretation of palaeoredox conditions in ancient mudstones. Chem Geol 111:111–129

150. Mazumdar A, Banerjee DM, Schidlowski M, Balaram V (1999) Rare-earth elements and Stable Isotope Geochemistry of early Cambrian chert-phosphorite assemblages from the Lower Tal Formation of the Krol Belt (Lesser Himalaya, India). Chem Geol 156:275–297

151. Skarpelis N, Perlikos P, Gale N, Gale-Stos S (1989) Rare earth elements and gold in lateritic derived sedimentary nickeliferous iron ores: the Marmeiko deposit, Beotia, continental Greece. Bull Geol Soc Greece 26:121–128

The rare earth elements potential of Greek bauxite active mines in the light of a sustainable REE demand

Platon N. Gamaletsos [a*], Athanasios Godelitsas [b], Anestis Filippidis [c], Yiannis Pontikes [d]

[a] Center for Electron Nanoscopy, Technical University of Denmark, 2800 Kongens Lyngby, Denmark

[b] Department of Geology and Geoenvironment, National and Kapodistrian University of Athens, Zografou Campus, 15784 Athens, Greece

[c] Department of Geology, Aristotle University of Thessaloniki, 54124 Thessaloniki, Greece

[d] KU Leuven, Department of Materials Engineering, Kasteelpark Arenberg 44, 3001 Leuven, Belgium

SUPPLEMENTARY MATERIAL

This supplement contains:

1. Supplementary Tables (6)

2. Supplementary Figures (24)

3. Supplementary References (46)

[*]Corresponding author: plagka@dtu.dk (Platon N. Gamaletsos)

Materials and Methods

Synchrotron Radiation micro-X-ray Fluorescence (SR μ-XRF) measurements. The synchrotron radiation (SR) micro-X-ray Fluorescence (μ-XRF) elemental maps were obtained using polished sections of the bauxite samples in the X-ray beamline of the Laboratory for Environmental Studies (SUL-X) of ANKA Synchrotron Radiation Facility, KIT, Germany, e.g. [1]. The data has been analysis and processed using the IGOR Pro software package (WaveMetrics, Inc., Lake Oswego, OR, USA). In the case of As, the Synchrotron study aimed in element distribution and speciation (As^{3+}, As^{5+}) in areas of the Fe-rich bauxite samples previously mapped by SR μ-XRF. Spectra were measured at the As K-edge (11,867 eV). Natural minerals of known As oxidation state, such as arsenopyrite (FeAsS), orpiment (As_2S_3), and arsenates (i.e., annabergite: $Ni_3(AsO_4)_2.8H_2O$ and scorodite: $FeAsO_4.2H_2O$), as well as synthetic As^{3+} compounds, such as As_2O_3 (arsenolite) and $NaAsO_2$ (sodium meta-arsenite) were used as reference materials. Spectral data were analyzed the ATHENA software package [2].

Supplementary Tables

Table S1: The QA/QC data for bulk XRF analyses. Concentration were depicted from Govindaraju (1989) [3].

Detection limits and error analysis of the trace element calibration
(routine program)

XRF equipment: MagiX PRO Philips (currently PANalytical B.V.)

Rh Anode at 3.6 kW
Preparation: undiluted powdered pressed pellets

Element	Average Concentration	RMS	LLD	Measuring Time Peak Peak	Maximum Concentration of calibration	RMSrel
	(ppm)	*(ppm)*	*(ppm)*	*(sec)*	*(ppm)*	*(%)*
Sc	32	1.6	2.7	40	60	5.0
V	317	8.1	6.1	40	600	2.6
Cr	289	6.8	5.3	30	400	2.4
Co	45	2.1	2.2	20	70	4.7
Ni	121	3.5	3.7	18	300	2.9
Cu	100	2.9	1.6	10	400	2.9
Zn	224	3.6	1.1	6	500	1.6
Ga	39	1	1	6	70	2.6
Rb	152	3.7	1.2	12	600	2.4
Sr	403	5.4	1.5	12	1500	1.3
Y	184	1.6	1.3	8	200	0.9
Zr	780	11	0.9	8	1200	1.4
Nb	110	1.3	1.1	10	300	1.2
Ba	800	22	10.5	40	2500	2.8
Pb	39	2.2	2.7	20	5000	5.6
Th	18.5	1.6	1.7	40	400	8.6
U	4.6	1.1	1.1	40	150	23.9

$$\mathrm{RMS} \;=\; \frac{1}{n-1} \times \sqrt{\sum_{i=1}^{N} \left(X_i - \overline{X}\right)^2} \qquad \textbf{(root mean square)}$$

$$\mathrm{LLD} = \frac{n\sqrt{2}}{s} \times \sqrt{\frac{r_b}{t_b}} \qquad \textbf{(lower limit of detection)}$$

Used Standards:

BIR-1	W-2	RGM-1	MAG-1	STM-1	SCO-1	DNC-1
SY-2	QLO-1	SGR-1	G-2	W-1	BCR-1	GSN
GSS-3	SO-4	AGV-1	BR	GSP-1	DR-N	BE-N
BHVO-1	NIM-G	NIM-S	SDC-1	JG-2	JB-2	AN-G
GSS-2	GSS-4	GSR-1	GSR-6	GSD-02	GSD-08	GSD-09
GSD-12	GSS-5	GSS-6	GSS-1	GSR-4	BCR-32	NBS278
NBS688	BX-N	AC-E	BM	NIST2710	SGD-1a	SG-1a
LKSD-4	JR-2	GXR-6	JR-1	JB-3		

Concentrations from Govindaraju (1989)

Table S2: The QA/QC data concerning bulk chemical analyses of the studied bauxite samples by ICP-OES, ICP-MS, and Leco analyzer.

Analyte	SiO$_2$	Al$_2$O$_3$	Fe$_2$O$_3$	MgO	CaO	Na$_2$O	K$_2$O	TiO$_2$	P$_2$O$_5$	MnO	Cr$_2$O$_3$	Sc	Ba	Co
Unit	%	%	%	%	%	%	%	%	%	%	%	ppm	ppm	ppm
MDL	0.01	0.01	0.04	0.01	0.01	0.01	0.01	0.01	0.01	0.01	0.002	1	1	0.2
STD1	58.25	14.08	7.58	3.33	6.34	3.68	2.13	0.69	0.82	0.39	0.545	25	499	26.2
STD1	58.12	14.09	7.62	3.34	6.36	3.68	2.15	0.69	0.83	0.39	0.546	25	497	26.7
STD1 Expected	58.47	14.23	7.67	3.35	6.42	3.71	2.17	0.69	0.83	0.39	0.55	25	514	26.2
BLK (Blank)	<0.01	<0.01	<0.04	<0.01	<0.01	<0.01	<0.01	<0.01	<0.01	<0.01	<0.002	<1	<1	<0.2

Analyte	Cs	Ga	Hf	Nb	Rb	Sn	Sr	Ta	Th	U	V	W	Zr	Y
Unit	ppm	ppm	ppm	ppm	ppm	ppm	ppm	ppm	ppm	ppm	ppm	ppm	ppm	ppm
MDL	0.1	0.5	0.1	0.1	0.1	1	0.5	0.1	0.2	0.1	8	0.5	0.1	0.1
STD1	6.7	17.1	9.3	20.5	27.8	15	398.4	6.8	9.9	16	200	14.5	278.3	30.5
STD1	6.5	17	9.5	20.4	27.5	14	398.7	6.8	9.7	16	200	14.6	278.1	30.5
STD1 Expected	7.1	17.6	9.8	21.3	28.7	15	407.4	7.4	9.9	16.4	200	14.8	280	31
BLK (Blank)	<0.1	<0.5	<0.1	<0.1	<0.1	<1	<0.5	<0.1	<0.2	<0.1	<8	<0.5	<0.1	<0.1

Analyte	La	Ce	Pr	Nd	Sm	Eu	Gd	Tb	Dy	Ho	Er	Tm	Yb	Lu
Unit	ppm	ppm	ppm	ppm	ppm	ppm	ppm	ppm	ppm	ppm	ppm	ppm	ppm	ppm
MDL	0.1	0.1	0.02	0.3	0.05	0.02	0.05	0.01	0.05	0.02	0.03	0.01	0.05	0.01
STD1	11.7	27.1	3.3	13.5	2.89	0.85	2.82	0.5	2.86	0.59	1.72	0.27	1.72	0.27
STD1	12	27.4	3.3	13.5	2.82	0.85	2.82	0.49	2.83	0.6	1.71	0.24	1.68	0.26
STD1 Expected	12.3	27.1	3.45	14	3	0.89	2.93	0.53	3	0.62	1.84	0.27	1.79	0.27
BLK (Blank)	<0.1	<0.1	<0.02	<0.3	<0.05	<0.02	<0.05	<0.01	<0.05	<0.02	<0.03	<0.01	<0.05	<0.01

Analyte	Mo	Cu	Pb	Zn	Ni	As	Cd	Sb	Bi	Ag	Au	Hg	Tl	Se
Unit	ppm	ppm	ppm	ppm	ppm	ppm	ppm	ppm	ppm	ppm	ppb	ppm	ppm	ppm
MDL	0.1	0.1	0.1	1	0.1	0.5	0.1	0.1	0.1	0.1	0.5	0.01	0.1	0.5
STD2	20.8	105.5	72.6	407	58.5	54.2	6.4	5	5	0.9	63.4	0.18	4.3	4
STD2 Expected	20.5	109	70.6	411	56	48.2	6.4	4.6	4.5	0.9	70	0.2	4.2	3.5
STD3	1.1	607.1	18.9	123	295.1	3.6	0.1	0.2	0.2	0.3	41.2	0.02	<0.1	0.6
SDT3 Expected	0.9	600	19	119	281	4.2	0.09	0.13	0.18	0.3	43	0.03	0.07	0.54
BLK (Blank)	<0.1	<0.1	<0.1	<1	<0.1	<0.5	<0.1	<0.1	<0.1	<0.1	<0.5	<0.01	<0.1	<0.5

Analyte	C	S
Unit	%	%
MDL	0.02	0.02
STD4	0.17	18.85
SDT4 Expected	0.16	18
BLK (Blank)	<0.02	<0.02

Table S3: Major and trace element concentrations (including Eu/Eu*, Ce/Ce*, La/Sm, La/Yb and Gd/Yb values [4-21]) in the studied bauxites from Parnassos-Ghiona active mining area. Commonly, the elements comprise the LREE and HREE groups are arbitrary defined [4-6].

Sample	ALM0306_PL1_BIW	ALM0306_BIW	ALM0306_PL1_WB	ALM0306_PL1_BS2	ELM0206_SK_B1a	ELM0206_SK_B1b	ELM0206_SK_B2	ALM0306_PL1_B1
Description	Fe-depleted	Fe-depleted	Fe-depleted	Fe-depleted	Fe-depleted	Fe-depleted	Fe-rich	Fe-rich
	B3 horizon	B3 horizon	B3 horizon	B3 horizon	B3 horizon	B3 horizon	B3 horizon	B3 horizon
	High-grade	High-grade	High-grade	High-grade	High-grade	High-grade	Low-grade	Low-grade
	Diasporic	Diasporic	Diasporic	Diasporic	Diasporic	Diasporic	Diasporic	Diasporic
	White-grey	White-grey	White-grey	White-grey	White-grey	White-grey	Red-brown	Red-brown
wt.%								
SiO_2	0.08	0.17	0.2	0.14	0.32	0.28	0.34	1.95
Al_2O_3	79.24	78.79	79.22	79.31	79.62	80.22	67.64	61.53
$Fe_2O_3(T)$	1.71	2.81	1.98	1.95	0.95	1.08	14.12	20.58
MnO	bdl	bdl	bdl	bdl	bdl	bdl	bdl	0.01
MgO	0.11	0.12	0.12	0.12	0.13	0.13	0.13	0.16
CaO	bdl	0.01	0.02	0.02	0.04	0.03	0.04	0.02
Na_2O	bdl	bdl	bdl	bdl	bdl	bdl	bdl	bdl
K_2O	bdl	bdl	bdl	bdl	bdl	bdl	bdl	bdl
TiO_2	3.35	2.92	3.42	3.09	3.26	2.67	2.78	2.69
P_2O_5	0.01	0.02	0.02	0.02	0.03	0.02	0.05	0.01
Cr_2O_3	0.14	0.12	0.10	0.15	0.14	0.12	0.14	0.12
LOI	14.91	14.84	14.70	14.91	15.06	15.15	14.59	12.39
Total	99.55	99.80	99.78	99.71	99.55	99.70	99.83	99.46
ppm								
Be	4.5	6	9	4	6	9	5	8
Sc	29.1	31	38	29	39	32	38	57
V	521	362	414	561	402	354	415	548
Cu	0.05	0.1	0.6	0.2	0.3	0.5	2.2	5.4
Co	4.1	4	4.3	4.6	4.2	3.4	10.1	40.7
Ni	37	7.3	2.3	11.5	4.4	2.0	20.7	1076
Zn	24.6	7	6	4.5	5	3	4.5	52
Ga	84.2	80.1	83.5	86.3	82.2	84.9	72.1	68.3
As	0.5	0.49	0.45	0.5	0.44	0.39	30.2	0.7
Se	bdl	0.5	0.5	0.5	0.5	0.5	0.5	0.5
Rb	0.25	0.5	0.5	0.5	0.5	0.5	0.5	0.5
Sr	31.8	54.3	46.2	45.8	98.1	74	56.9	24.5
Y	31.2	47.8	88.4	30.7	49.2	43.4	33.4	67.2
Zr	568.1	478.2	550.6	488.4	502.8	443.4	451.1	404.8
Nb	62.3	59.5	68	62.3	62.5	54	56.2	53
Mo	0.6	0.5	2.4	2.7	0.8	0.3	6.7	3
Ag	bdl	bdl	bdl	bdl	bdl	bdl	bdl	bdl
Cd	0.1	0.1	0.1	0.1	0.1	0.1	0.1	0.1
Sn	11.9	13	15	11	10	11	11	12
Sb	4.9	3.1	2.8	4.1	1.6	0.7	2	7.6
Cs	1	0.1	0.1	0.1	0.1	0.1	0.1	0.1
Ba	4.7	8.3	5.9	5.1	4.4	5.1	5.7	24.5
Hf	14.35	13.9	15.9	13.9	14.8	13.5	13.4	12.3
Ta	2.88	2.9	3.1	3	3	2.7	3.3	3.2
W	51.3	33.4	47.3	48.6	37.8	37.1	88.9	94.5
Hg	0.04	0.02	0.02	0.05	0.01	0.01	0.02	0.02
Tl	bdl	0.07	0.08	0.07	0.1	0.06	0.09	0.1
Pb	4.35	3.8	2.1	1.3	2.7	2.9	6	64.1
Bi	0.53	1.4	1.7	1	2.8	0.8	2.6	2.4
La	6.1	36.1	46.9	7.9	38.8	25	12.3	32
Ce	106.1	153.5	118.5	124.6	101.8	66.9	80.9	216.1
Pr	1.75	5.92	7.63	2.14	6.07	3.68	2.09	6.41
Nd	6.3	16.8	20	7.7	17.5	11.4	6.4	21.7
Sm	2.32	2.84	3.84	1.65	2.86	2.22	1.4	6.33
Eu	0.41	0.58	0.97	0.38	0.71	0.53	0.37	1.65
Gd	2.03	2.44	4.95	1.65	3.24	2.76	2.05	7.36
Tb	0.68	0.83	1.96	0.58	1.04	0.81	0.69	2.44
Dy	4.73	6.31	15.6	4.34	7.4	5.47	4.74	16.59
Ho	1.05	1.5	3.63	0.92	1.59	1.19	1.04	3.7
Er	3.49	5.22	12.29	3.07	5.17	3.95	3.26	11.33
Tm	0.59	0.99	2.21	0.58	0.91	0.69	0.56	1.68
Yb	3.05	7.12	15.59	3.85	6.33	4.57	4.01	10.33
Lu	0.68	1.13	2.49	0.62	1.01	0.77	0.63	1.65
Th	60.5	28.6	34.4	59.6	32.2	37.5	32.9	48.3
U	9.33	8.1	11.1	10.8	6.2	4	5.1	10.5
ppb								
Au	2.6	2.4	2	0.5	1.2	0.8	0	1.6
ppm								
ΣLREE [1]	125	218	203	146	171	112	106	292
ΣHREE [1]	45	71	142	45	73	61	48	115
ΣREE [1]	199	320	383	220	283	205	192	463
$[Eu/Eu*]_{ch}$	0.56	0.66	0.69	0.70	0.72	0.66	0.67	0.74
$[Ce/Ce*]_{ch}$	7.87	2.17	1.30	7.20	1.34	1.37	3.31	3.28
$[Eu/Eu*]_{ch}$ [2]	0.57	0.68	0.69	0.71	0.72	0.66	0.67	0.74
$[Eu/Eu*]_{NASC}$ [2]	0.58	0.68	0.69	0.71	0.72	0.66	0.67	0.75
$[Eu/Eu*]_{NASC}$	0.54	0.64	0.59	0.65	0.64	0.57	0.56	0.66
$[Ce/Ce*]_{NASC}$	7.94	2.39	1.44	7.32	1.48	1.51	3.62	3.49
$[La/Sm]_{ch}$	1.55	7.55	7.25	2.84	8.06	6.69	5.22	3.00
$[La/Sm]_{NASC}$	0.50	2.44	2.35	0.92	2.61	2.17	1.69	0.97
$[La/Yb]_{ch}$	1.31	3.33	1.98	1.35	4.03	3.60	2.02	2.04
$[La/Yb]_{NASC}$	0.20	0.51	0.30	0.21	0.61	0.55	0.31	0.31
$[Gd/Yb]_{ch}$	0.55	0.28	0.26	0.35	0.42	0.50	0.42	0.59
$[Gd/Yb]_{NASC}$	0.83	0.43	0.40	0.53	0.64	0.75	0.64	0.89

Table S3: Continuing

Sample	ALM0306_PL1_B3	ALM0306_PL1_B4	ELM0206_DV_B1	SAB0306_ASV	ALM0306_PL1_B2	ELM0206_KV_B1	ELM0206_2H1	SAB0306_SKR	ALM0306_PL1_BS1
Description	Fe-rich	Fe-rich	Fe-rich	Fe-rich	Fe-rich	Fe-rich	Fe-rich	Fe-rich	Fe-rich & S-bearing
	B3 horizon	B3 horizon	B2 horizon	B3 horizon	B3 horizon	B2 horizon	B2 horizon	B2 horizon	B3 horizon
	Low-grade	Low-grade	Low-grade	Low-grade	Low-grade	Low-grade	Low-grade	Low-grade	Low-grade
	Diasporic	Diasporic	Diasporic	Diasporic	Boehmitic	Boehmitic	Boehmitic	Boehmitic	Boehmitic
	Red brown	Red brown	Red brown	Red brown	Red brown	Red brown	Red brown	Red brown	Red-grey
wt.%									
SiO_2	0.75	0.4	1.96	0.50	6.1	13.9	8.57	8.94	1.63
Al_2O_3	61.70	56.84	62.49	63.36	55.25	49.70	44.25	52.83	55.28
$Fe_2O_3(T)$	21.95	24.57	19.30	20.29	22.52	20.28	27.66	22.45	27.66
MnO	0.01	bdl	0.01	0.01	0.02	0.08	bdl	0.42	0.02
MgO	0.11	0.1	0.2	0.1	0.3	0.4	0.2	0.39	0.08
CaO	0.08	0.10	0.02	0.05	0.09	0.13	0.21	0.11	0.02
Na_2O	bdl	bdl	bdl	bdl	bdl	bdl	bdl	bdl	bdl
K_2O	bdl	0.01	bdl	bdl	0.16	0.35	0.2	0.21	0.07
TiO_2	2.63	2.29	3.44	3.36	2.49	2.23	2.58	2.41	2.57
P_2O_5	0.02	0.03	0.01	0.01	0.01	0.04	0.06	0.04	0.01
Cr_2O_3	0.13	0.10	0.14	0.16	0.11	0.03	0.17	0.05	0.13
LOI	12.18	15.07	11.96	12.19	12.16	11.93	15.61	11.96	10.18
Total	99.56	99.51	99.53	100.03	99.21	99.07	99.51	99.81	97.64
ppm									
Be	9	6	5	5	10	4	5	7	5
Sc	51	45	73	71	57	54	46	56	48
V	617	683	271	420	711	340	518	329	523
Cu	6	1	4.8	3	29.6	17.6	3.5	54.6	1.1
Co	18.4	6.1	57.7	26.3	70.8	27	32.9	98.9	50.7
Ni	479	112	1142	188	412	58	144	103	423
Zn	27	17	11	4	46	81	8	126	4
Ga	65.5	48.4	59.5	60.1	58.4	62.5	58	63	43.1
As	1.2	43.5	0	0.5	5	11.5	176.7	9.6	162.3
Se	0.5	0.5	0.5	0.5	0.5	0.5	3.5	0.5	3.6
Rb	0.5	0.5	0.5	0.8	6.5	28	4	16.5	1.5
Sr	44.6	29.2	13.2	23.9	34.2	76.4	271.7	69.4	24.7
Y	71.2	35	89.2	68	96.2	89.8	53.4	126.5	43
Zr	410.8	353.3	520.4	556.4	407.3	408.7	433.4	425.1	465.2
Nb	51.6	44.9	71.1	66.3	50.2	46	51.9	48.7	45.3
Mo	3.6	64.8	0.9	0.7	2.6	1.1	2.7	1.4	17.8
Ag	bdl	bdl	bdl	bdl	bdl	bdl	bdl	bdl	bdl
Cd	0.2	0.3	0.1	0.1	0.1	0.3	0.3	0.9	0.1
Sn	12	8	17	15	11	11	8	11	11
Sb	8.9	22.5	0.6	4.8	12.5	1.9	2.8	2.4	15.9
Cs	0.1	0.1	0.1	0.1	2.8	9.4	0.6	6.4	0.2
Ba	18.6	19.8	9.1	16.7	44.5	74.2	7.8	62.3	15.5
Hf	12.3	10.6	14.7	16.1	11.4	11.7	12.8	12.4	10.8
Ta	3.1	2.7	3.7	3.6	3.1	2.8	3.2	2.9	2.8
W	50.5	57.4	66.5	133.8	19	13	62.2	28.9	28.8
Hg	0.01	0.77	0.01	0.01	0.01	0.02	0.16	0.02	0.15
Tl	0.1	0.2	0.08	0.1	0.1	0.1	0.07	0.1	0.1
Pb	72.6	28	49.6	72.2	107.2	111	123.9	116.1	67.6
Bi	2.2	1.4	1.8	2.7	2.3	1.8	2.6	2.1	2.4
La	82.7	23.7	106	52.2	140.1	167.1	45.9	140.5	22.7
Ce	99.1	99.9	655	350.5	251.4	286.4	203.4	291.6	83.5
Pr	12.1	7.45	25.13	9.83	36.8	23.27	12.97	28.89	6.07
Nd	35.2	29.3	90.8	33.3	136.1	79.2	49.1	109.8	22.5
Sm	7.82	6.77	19.29	7.57	29.94	14.64	9.69	23.37	4.96
Eu	1.9	1.35	3.75	1.63	5.82	2.7	1.61	4.57	1.1
Gd	9.14	5.39	12.74	6.72	20.42	9.94	5.49	18.44	4.77
Tb	2.76	1.19	2.39	1.85	4.37	2.19	1.36	3.66	1.22
Dy	18.33	6.4	12.08	10.85	22.88	12.32	8.7	19.22	7.37
Ho	3.87	1.2	2.26	2.23	4.16	2.5	1.68	3.69	1.44
Er	12.52	3.6	6.84	6.85	12.24	7.78	5.53	10.98	4.36
Tm	2.03	0.6	1.14	1.14	2.06	1.31	0.98	1.75	0.76
Yb	13.02	4.04	7.84	7.92	13.25	9	7.08	11.71	4.91
Lu	2.12	0.64	1.22	1.23	2.05	1.4	1.11	1.82	0.78
Th	58.8	44.9	50.7	64	48.4	51	63.7	53	60.4
U	11.3	12.4	8.8	7.8	10	5.7	11.2	6.7	10.7
ppb									
Au	0.5	3.5	bdl	1.3	6.8	bdl	0.7	1.3	0.9
ppm									
ΣLREE [1]	248	174	913	462	621	583	328	617	146
ΣHREE [1]	126	53	123	100	157	126	80	179	64
ΣREE [1]	425	272	1109	633	835	764	454	853	257
$[Eu/Eu*]_{ch}$	0.69	0.67	0.69	0.69	0.69	0.65	0.62	0.65	0.69
$[Ce/Ce*]_{ch}$	0.62	1.82	2.89	3.29	0.82	0.87	1.98	0.99	1.67
$[Eu/Eu*]_{ch}$ [2]	0.69	0.69	0.74	0.70	0.73	0.69	0.68	0.68	
$[Eu/Eu*]_{NASC}$ [2]	0.69	0.69	0.74	0.71	0.73	0.69	0.68	0.68	
$[Eu/Eu*]_{NASC}$	0.61	0.66	0.72	0.66	0.71	0.67	0.67	0.65	0.64
$[Ce/Ce*]_{NASC}$	0.68	1.80	2.99	3.52	0.83	0.96	1.99	1.03	1.70
$[La/Sm]_{ch}$	6.28	2.08	3.26	4.10	2.78	6.78	2.81	3.57	
$[La/Sm]_{NASC}$	2.03	0.67	1.06	1.33	0.90	2.19	0.91	1.16	
$[La/Yb]_{ch}$	4.18	3.86	8.89	4.33	6.95	12.21	4.26	7.89	3.04
$[La/Yb]_{NASC}$	0.64	0.59	1.35	0.66	1.06	1.86	0.65	1.20	0.46
$[Gd/Yb]_{ch}$	0.58	1.10	1.34	0.70	1.27	0.91	0.64	1.30	0.80
$[Gd/Yb]_{NASC}$	0.87	1.66	2.02	1.06	1.92	1.38	0.97	1.96	1.21

Note:
bdl: below detection limit
Eu/Eu* = [2* ($Eu_{measured}$ / Eu_n)] / [($Sm_{measured}$ / Sm_n) + ($Gd_{measured}$ / Gd_n)]; after: Liu et al. (2013) [7].
Ce/Ce* = [3* ($Ce_{measured}$ / Ce_n)] / [($La_{measured}$ / La_n) + ($Nd_{measured}$ / Nd_n)]; after: German & Elderfield (1990) [8].

[1] The ΣLREE group includes the lanthanide elements from La through Gd (5, 6); The ΣHREE group includes the lanthanide elements from Tb through Lu, including Y (5, 6); The ΣREE group comprises of the 15 lanthanide elements including Sc, and Y (5, 6).

[2] In this case, Eu anomaly has been quantified using the equation: Eu/Eu* = [Eu_n / √(Sm_n · Gd_n)] after Mongelli et al. (2014) [9]; Chondrite values are depicted using the average chondrite values [10-17].

** NASC values are from Gromet et al. (1984) [18].

*** Chondrite values [10-17] are the average of selected average values of ordinary chondrites / OC [11-13, 17], and carbonaceous chondrites / CI [10, 16] as well as of values reported by Korotev (1996a & 1996b) [14, 15] -who utilized the CI values from Anders and Grevesse (1989) [19] multiplied by 1.3596. This approach is based on comments by Rollinson (1993) [20] and suggestions by Korotev (2010) [21]. The values of CI chondrites have been selectively chosen in order to be consistent with the average values of OC chondrites [11-13, 17].

Table S4: New analytical data concerning representative bauxite samples from active mines of Balkan countries (i.e., Bosnia, and Montenegro) and Hungary, supplied by the Ajkai Timföldgyár alumina plant (MAL Magyar Alumínium Zrt) after György Bárdossy† personal communication (see: **Supplementary Data; Fig. S2**).

Sample code Country	MAL-Jajce Bosnia	MAL-Halimba Hungary	MAL-Niksic Montenegro	Sample code Country	MAL-Jajce Bosnia	MAL-Halimba Hungary	MAL-Niksic Montenegro
Unit wt.%	*data*	*data*	*data*	*Unit* ppm	*data*	*data*	*data*
SiO_2	0.92	5.83	6.42	Ag	0	1.7	0
Al_2O_3	58.57	52.77	57.14	Cd	0.2	0.2	1.8
$Fe_2O_3(T)$	25.12	21.8	19.84	Sn	12	12	11
MnO	0.02	0.13	0.12	Sb	3.9	9.5	1.8
MgO	0.05	0.17	0.23	Cs	0.3	0.2	2.5
CaO	0.35	2.05	0.21	Ba	10	18	42
Na_2O	0.01	0.07	0.02	Hf	15.7	15.2	13.8
K_2O	0	0.06	0.2	Ta	3.9	3.3	4.4
TiO_2	2.67	2.59	2.75	W	5.5	5.8	6.6
P_2O_5	0	0.12	0.05	Hg	0.04	0.06	0.09
Cr_2O_3	0.08	0.06	0.06	Tl	0	0	0
LOI	11.9	14	12.6	Pb	70.8	65.8	94.9
Total	99.69	99.65	99.64	Bi	2.8	1	2.7
				La	112.1	77.8	153.1
ppm				Ce	287.2	126.2	330.8
Be	7	3	5	Pr	27.3	13.7	30.3
Sc	63	44	64	Nd	107.7	49	117.1
V	324	805	284	Sm	20.04	7.75	22.83
Cu	4	8.2	38.7	Eu	4.26	1.72	4.62
Co	16.2	24.1	20	Gd	19.32	7.78	19.97
Ni	128	70	115	Tb	2.84	1.34	2.99
Zn	7	10	98	Dy	15.47	9.16	17.9
Ga	45.1	52	47.7	Ho	2.82	1.91	3.47
As	37.5	16.5	4.3	Er	7.5	5.8	9.67
Se	0.8	0.6	0.7	Tm	1.15	0.91	1.68
Rb	0.2	1.3	11.7	Yb	7.86	5.75	11.37
Sr	43.9	120	83.4	Lu	1.13	0.91	1.55
Y	52.9	54.6	100.2	Th	61.3	46.6	48.3
Zr	519.5	580.5	543.1	U	6.7	15.4	7.5
Nb	48.3	51.4	56.7	*ppb*			
Mo	0.9	5.4	0.5	Au	0	1.1	1.9

Table S5: Major and trace element concentrations of the black (ALM0306_PL1_DLS1) to dark (ALM0306_PL1_DLS2) bituminous hanging wall limestone and the ordinary white footwall limestone (ALM0306_PL1_WLS).

Sample code	ALM0306_PL1_WLS	ALM0306_PL1_DLS1	ALM0306_PL1_DLS2	Sample code	ALM0306_PL1_WLS	ALM0306_PL1_DLS1	ALM0306_PL1_DLS2
Description	*Footwall Limestone White*	*Hanging wall Limestone Black*	*Hanging wall Limestone Dark*		*Footwall Limestone White*	*Hanging wall Limestone Black*	*Hanging wall Limestone Dark*
Mine Locality	**Pera Lakkos**	**Pera Lakkos**	**Pera Lakkos**	**Mine Locality**	**Pera Lakkos**	**Pera Lakkos**	**Pera Lakkos**
Unit *wt.%*	*data*		*data*	*Unit* *ppm*	*data*		*data*
SiO$_2$	0.11	0.04	0.08	Ag	bdl	bdl	bdl
Al$_2$O$_3$	0.53	0.11	0.08	Cd	0.3	0.1	0.1
Fe$_2$O$_3$(T)	0.07	0.39	0.08	Sn	1	1	1
MnO	0.01	0.01	0.01	Sb	0.1	0.2	0.1
MgO	0.11	1.06	1.47	Cs	0.1	0.1	0.1
CaO	55.69	54.06	53.52	Ba	1.6	5.4	2
Na$_2$O	0.02	0.02	0.02	Hf	0.5	0.5	0.5
K$_2$O	bdl	bdl	bdl	Ta	0.1	0.1	0.1
TiO$_2$	0.06	0.04	0.04	W	11.2	16.6	6
P$_2$O$_5$	-	-	-	Hg	0.01	0.02	0.01
Cr$_2$O$_3$	-	-	-	Tl	0.09	0.1	0.1
LOI	43.17	44.09	44.18	Pb	0.6	0.4	0.1
Total	99.77	99.82	99.48	Bi	0.1	0.1	0.1
				La	1.8	1.3	0.9
ppm				Ce	2.2	1.2	0.7
Be	1	1	1	Pr	0.27	0.19	0.08
Sc	-	-	-	Nd	0.9	0.8	0.4
V	6	23	5	Sm	0.19	0.11	0.06
Cu	0.1	0.2	0.1	Eu	0.05	0.02	0.02
Co	3.5	2.7	1.4	Gd	0.22	0.15	0.12
Ni	1.3	30.8	11.2	Tb	0.03	0.02	0.01
Zn	3	1	1	Dy	0.19	0.1	0.05
Ga	0.5	0.5	0.5	Ho	0.04	0.02	0.02
As	0.8	7.5	1.5	Er	0.07	0.05	0.03
Se	0.5	0.7	0.6	Tm	0.02	0.01	0.02
Rb	0.6	0.7	0.5	Yb	0.09	0.05	0.05
Sr	48.3	517	617.8	Lu	0.02	0.01	0.01
Y	1.6	0.8	0.5	Th	0.2	0.1	0.1
Zr	4.6	0.9	0.7	U	0.4	2	1.1
Nb	0.6	0.5	0.5	*ppb*			
Mo	0.1	2.6	0.3	Au	0.6	0.5	0.5

Table S6: Major and trace element concentrations of the coal (ALM0807_PL1_COAL) interstratified between the bauxite ore and the hanging wall limestone at Pera Lakkos underground mine. The bulk chemical composition of the flying ash (ALM0807_PL1_ASH) of coal is also depicted for comparison reasons.

Sample code	ALM0807_PL1_COAL	ALM0807_PL1_ASH	Sample code	ALM0807_PL1_COAL	ALM0807_PL1_ASH
Description	*Coal*	*Flying Ash*	Description	*Coal*	*Flying Ash*
Mine Locality	**Pera Lakkos**	**Pera Lakkos**	Mine Locality	**Pera Lakkos**	**Pera Lakkos**
Unit	*data*	*data*	*Unit*	*data*	*data*
wt.%			ppm		
SiO_2	0.22	30.85	Mo	9.5	62.7
Al_2O_3	0.67	33.93	Ag	bdl	0.9
$Fe_2O_3(T)$	1.45	22.01	Cd	bdl	bdl
MnO	bdl	0.01	Sn	bdl	5
MgO	0.09	1.02	Sb	3	1.7
CaO	0.27	2.92	Cs	0.2	21.5
Na_2O	0.02	1.88	Ba	2	175
K_2O	0.01	1.49	Hf	0.3	8.5
TiO_2	0.01	1.45	Ta	0	2.3
P_2O_5	0.01	0.08	W	bdl	4.1
Cr_2O_3	bdl	0.07	Hg	0.31	0.01
LOI	96.6	3.4	Tl	bdl	0.7
Total	99.35	99.114	Pb	0.9	9.6
TOT/C	78.37	0.1	Bi	bdl	0.3
TOT/S	5.62	0.48	La	23.4	293.5
			Ce	289.9	1531
ppm			Pr	11.63	73.63
Be	2	13	Nd	48.7	282
Sc	16	38	Sm	12.56	44.89
V	36	338	Eu	3.17	8.96
Cu	1.5	13.3	Gd	12.39	40.21
Co	2.7	35	Tb	1.99	4.71
Ni	257.1	488.3	Dy	10.82	23.92
Zn	7	3	Ho	2.18	4.5
Ga	8.6	74.8	Er	5.83	11.22
As	41.5	36.4	Tm	0.8	1.45
Se	3	bdl	Yb	4.73	8.64
Rb	1.1	80.5	Lu	0.62	1.12
Sr	166.9	799.7	Th	0.6	28.1
Y	57.3	226.7	U	30.4	135.1
Zr	8.7	285.6	*ppb*		
Nb	0.3	31.3	Au	bdl	10

Supplementary Figures

Figure S1: The "Aluminium of Greece S.A." processing plant in Agios Nikolaos area, Antikyra bay, Gulf of Corinth (**a**); general view of the underground works leading to the mining front (**b**); underground mining front at Pera Lakkos mine where the Fe-rich and Fe-depleted karst-type bauxites (together with footwall & hanging wall limestones; modified after Gamaletsos et al. 2017 [22]) were sampled (**c**); representative Fe-depleted (high-grade) white-grey bauxite from underground mine (**d**); representative Fe-rich (low-grade) red-brown bauxite sample from underground mine (**e**); characteristic open pit of "Imerys S.A.", where bauxite samples were also taken in the frame of the present study (**f**).
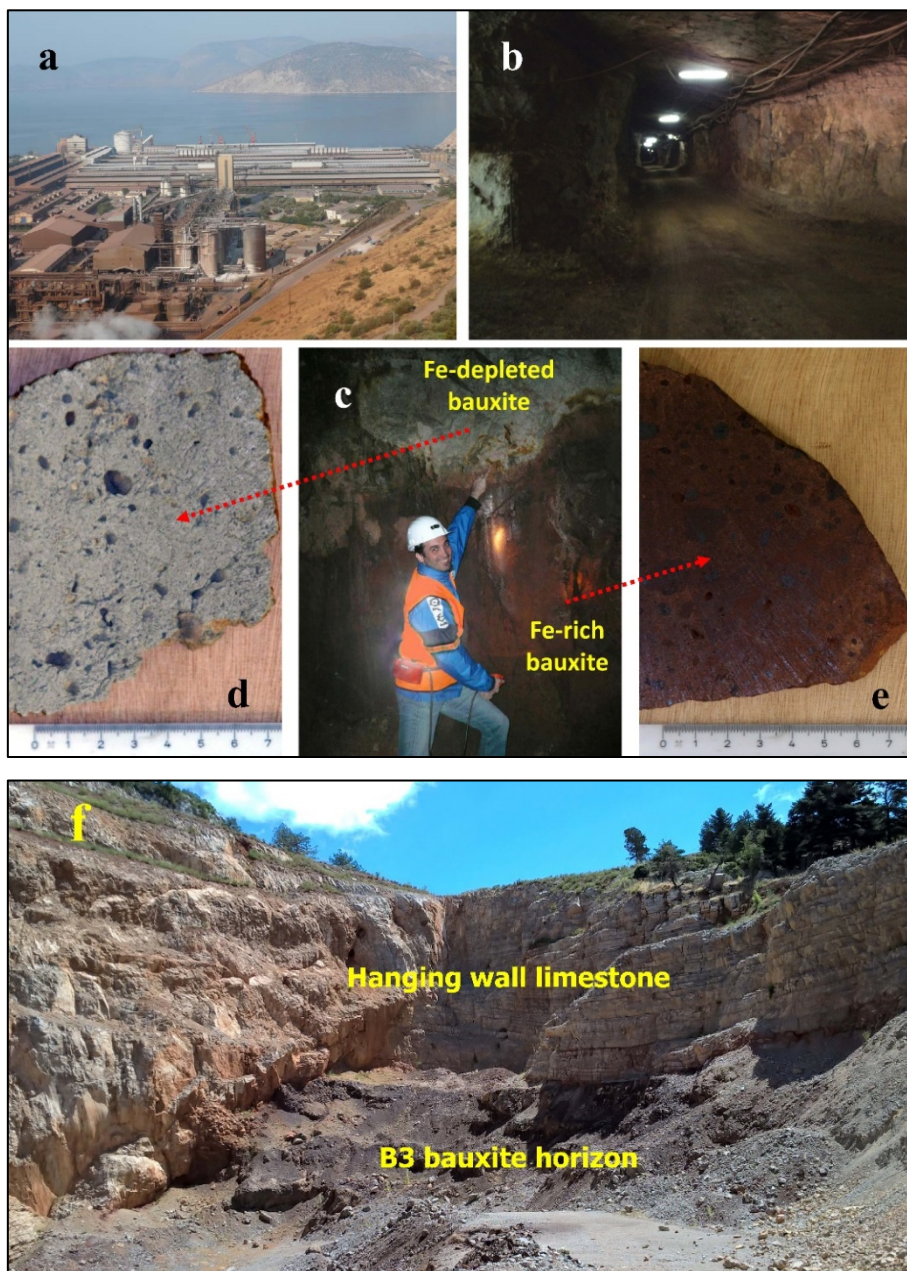
Figure S2: Representative karst-type bauxite samples provided by the "Ajkai Timföldgyár" alumina plant ("MAL Magyar Alumínium Zrt") from Balkan countries, such as Bosnia (Jajce deposit) and Montenegro (Nikšić deposit) and Hungary (Halimba deposit) used for comparison reasons.

Figure S3: PXRD patterns of representative Fe-depleted diasporic (black lower pattern: ①), Fe-rich diasporic (red middle pattern: ②) and Fe-rich boehmitic (red upper pattern: ③) bauxite samples from Parnassos-Ghiona active mining area; kaolin-group (kaolinite), boehmite, goethite, diaspore, anatase, rutile, hematite, and magnetite strongest reflections at 2θ (d in Å): 12.37 (7.15), 14.48 (6.11), 21.37 (4.16), 22.26 (3.99), 25.35 (3.51), 27.50 (3.24), 33.27 (2.69), and 35.46 (2.53), respectively.
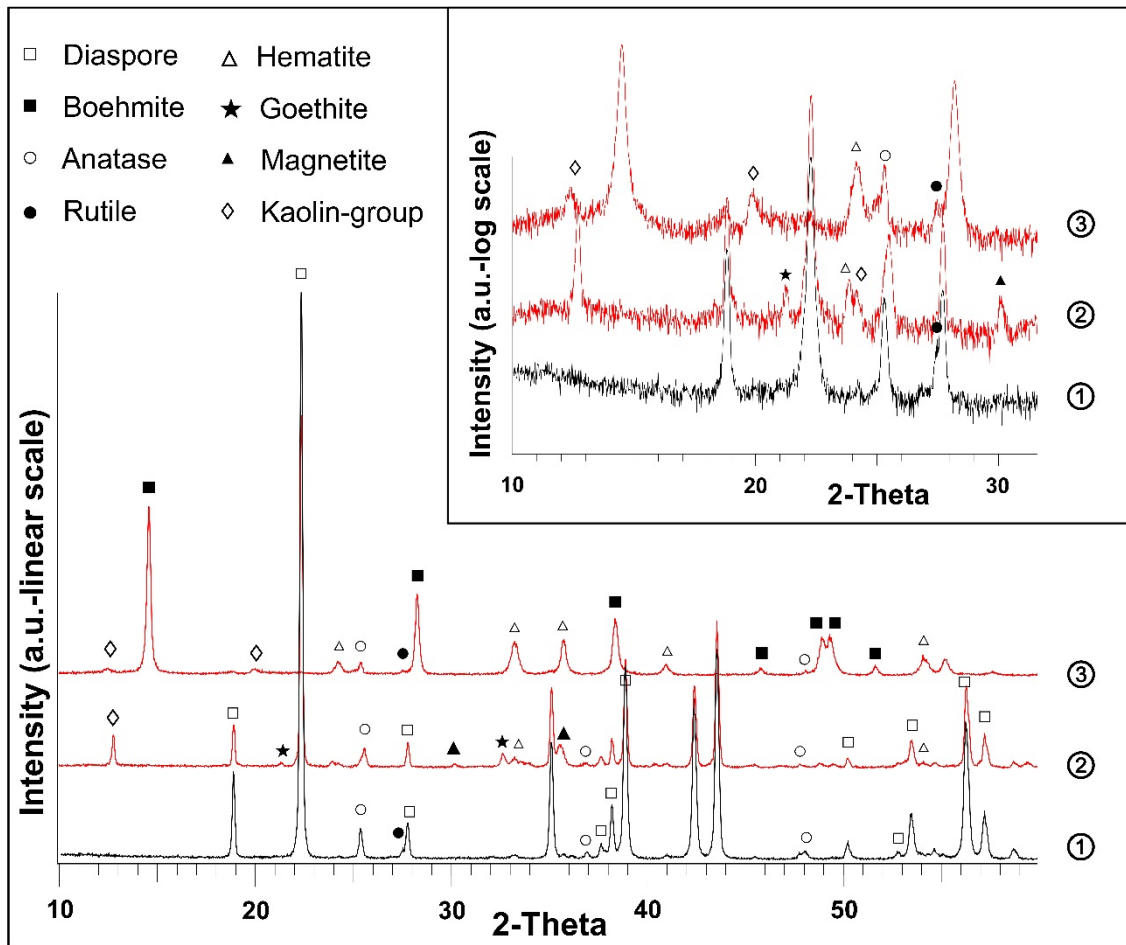
Figure S4: SEM-EDS/-WDS observations of Th-containing LREE^{3+} fluorocarbonate (mostly bastnäsite-/parisite-group: (REE)$^{3+}$Ca^{2+}F(CO$_3$)$_2$; e.g., [23]) mineral overgrown onto a spinel of a fresh-cracked specimen (bauxite geode) of a studied Fe-rich sample (modified after Gamaletsos et al., 2011 [24]). Three peaks at 0.67 keV, at 3.7 keV and at 4.65 keV are due to FK_α, CaK_α and LaL_α respectively. A peak at 1.48 keV is ascribed to AlK_α either from the spinel or from the diaspore grain beneath and in-between the REE,Th-containing grains, respectively. Abbreviations: "Dsp" for diaspore; "Spl" for spinel; "Hem" for hematite; "Ilm" for Ilmenite.
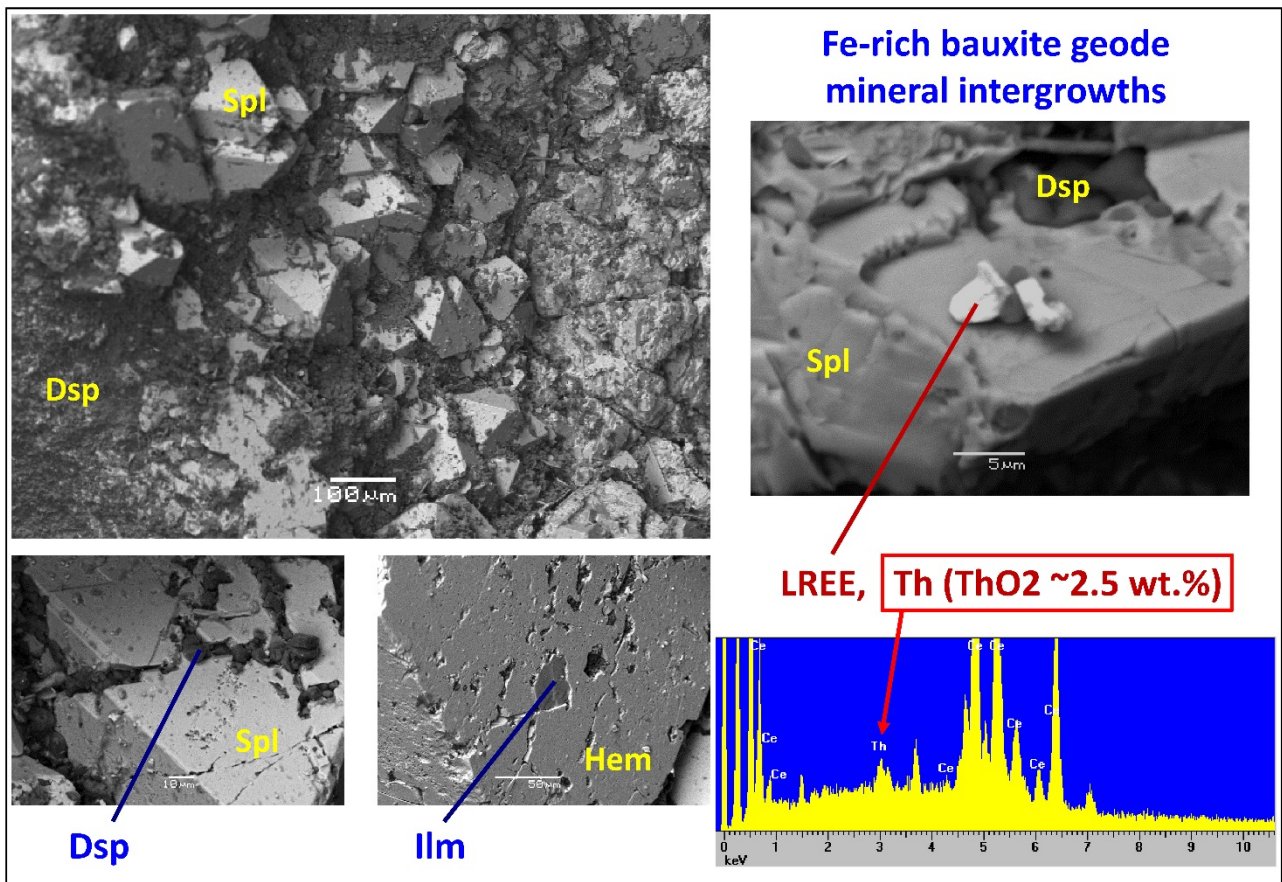
Figure S5: UCC-normalized [25] spider diagrams for the studied Fe-rich (upper image) and Fe-depleted karst-type bauxite samples (lower image) from the Parnassos-Ghiona mining area. Transparent light green background: depletion of average values; transparent light red background: enrichment of average values.
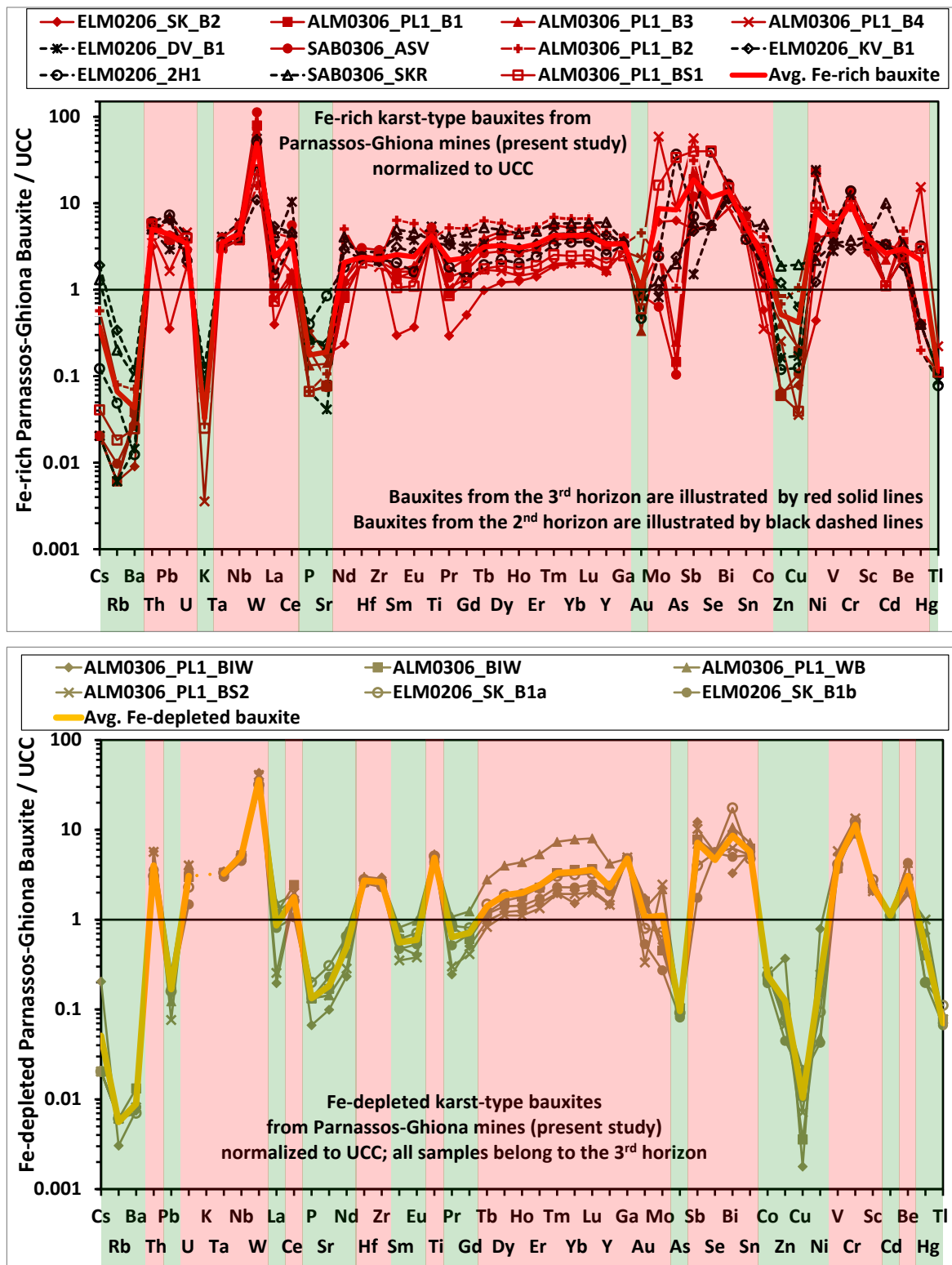
Figure S6: Binary diagrams showing the bulk correlation between Pb and other elements, such as Pb-Fe (upper image) as well as Pb-Al, Pb-Si, Pb-K, Pb-Ca and Pb-Mg (lower image) for the studied Parnassos-Ghiona bauxites.
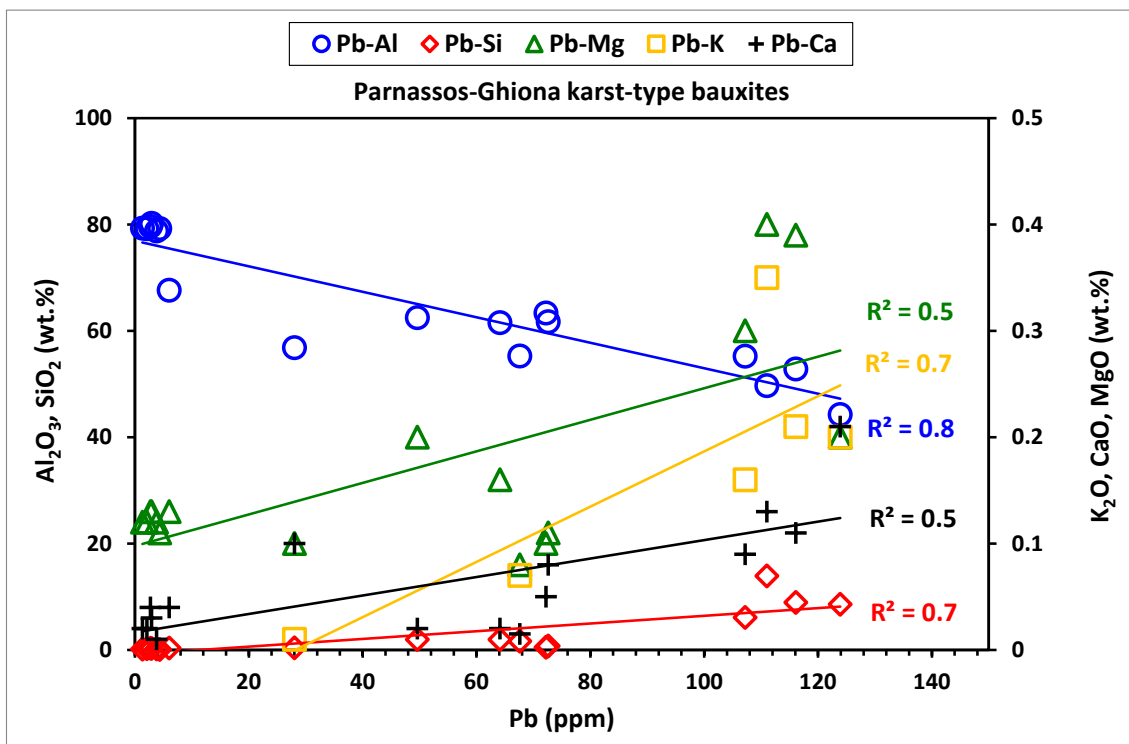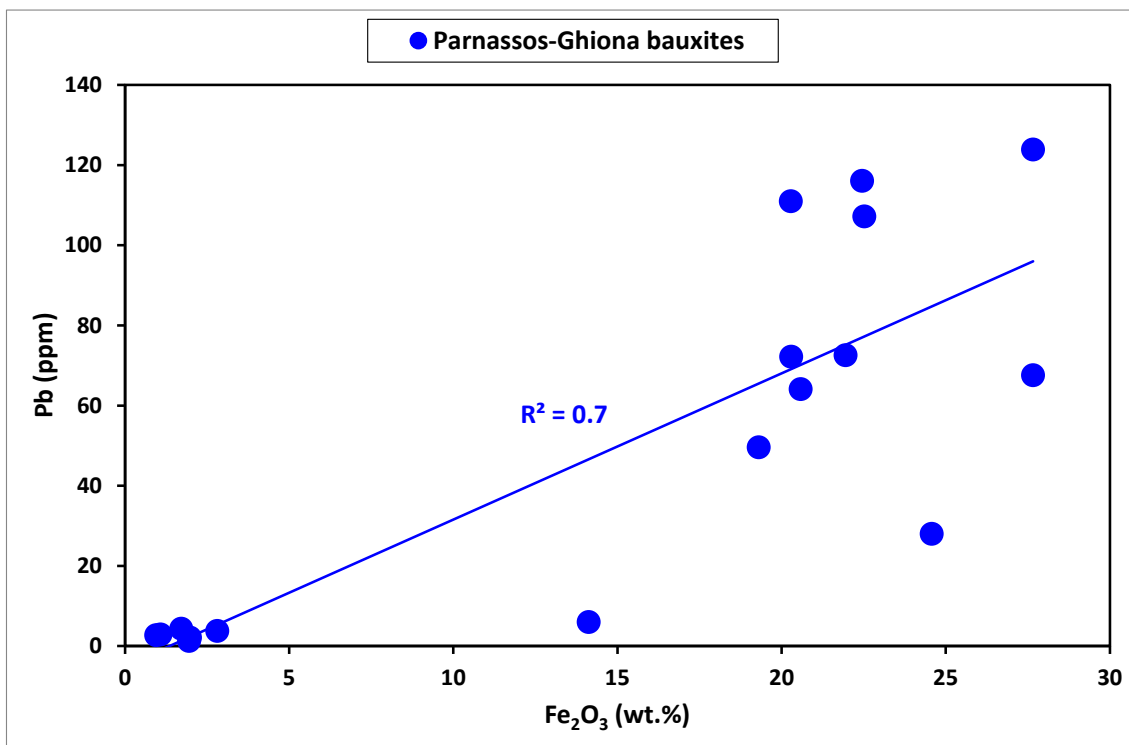
Figure S7: Binary diagram showing the bulk correlation between As and Fe for the studied Fe-rich Parnassos-Ghiona bauxites.
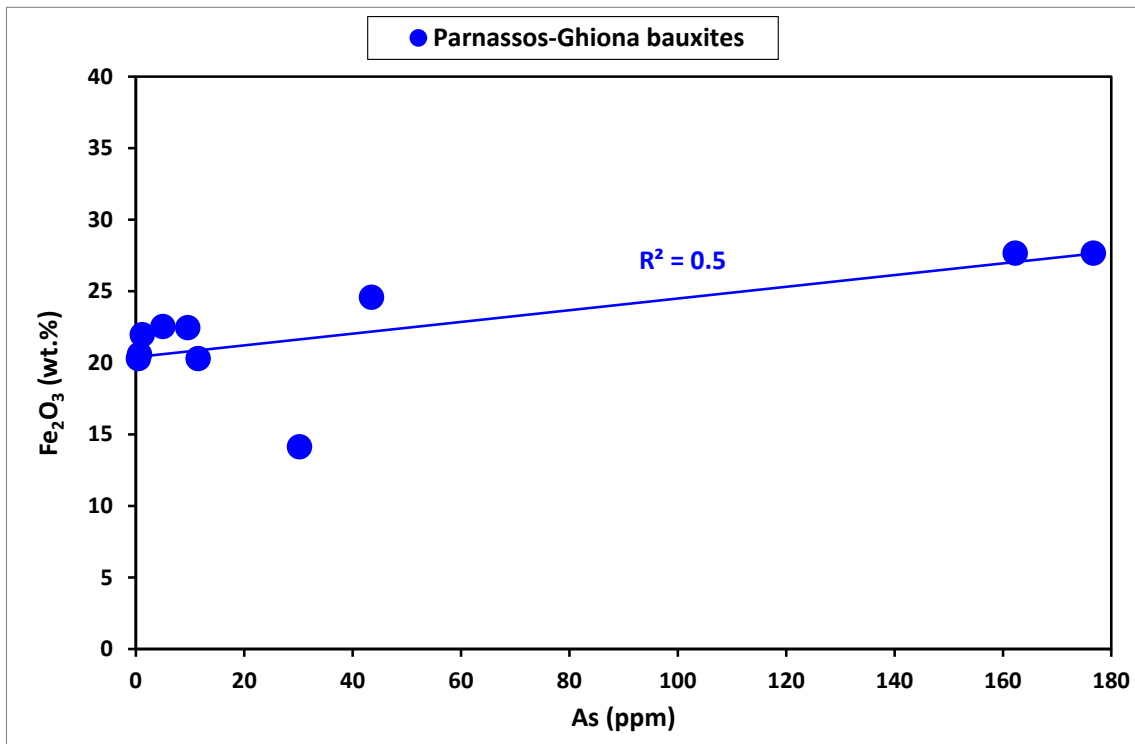
Figure S8: Binary diagram showing the bulk correlation between Co and Cu, Zn, and Mg (upper image), as well as plot of Si, K, Cs, Rb, and Ba illustrating the correlation between the more mobile LILE (lower image), for the studied Parnassos-Ghiona bauxites for the studied Parnassos-Ghiona bauxites.
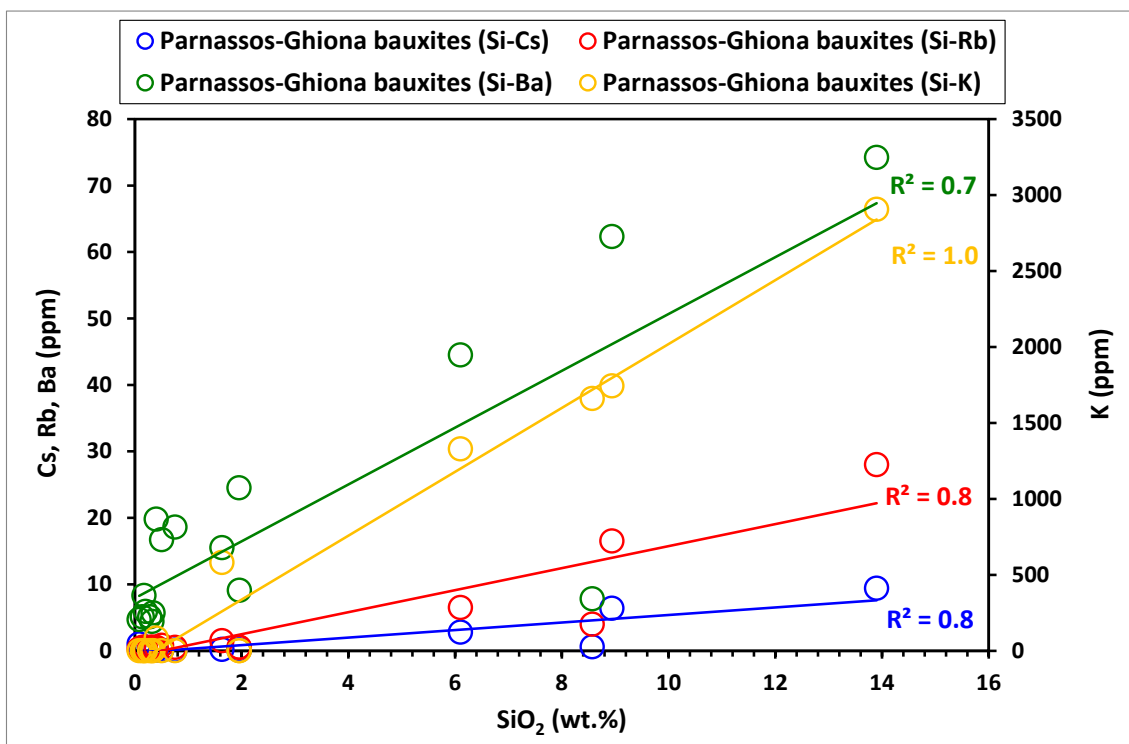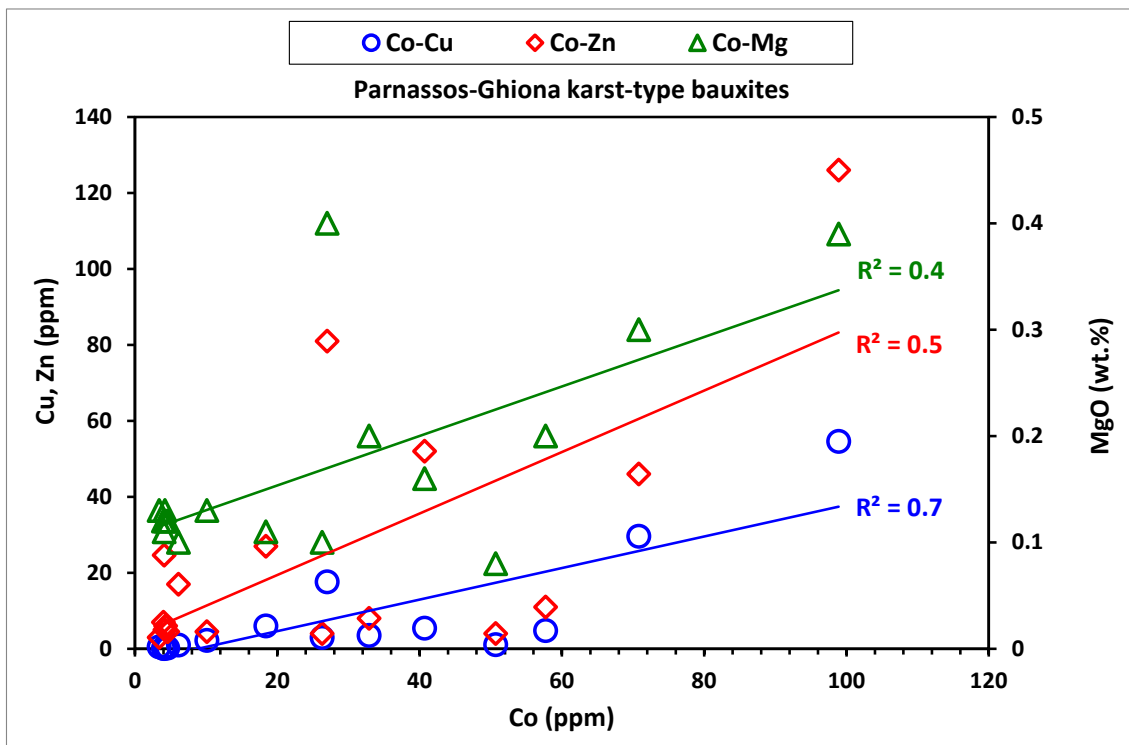
Figure S9: Synchrotron radiation (SR) μ-XRF mapping and μ-XANES data (normalized As *K*-edge XANES spectrum of the studied bauxite compared with spectra of natural minerals -annabergite, and scorodite- and with spectrum of a selected synthetic arsenite -arsenolite- used as reference materials) showing the incorporation of arsenates into Fe-Ti-Cr pisoliths in microscale for the studied Fe-rich Parnassos-Ghiona bauxites.
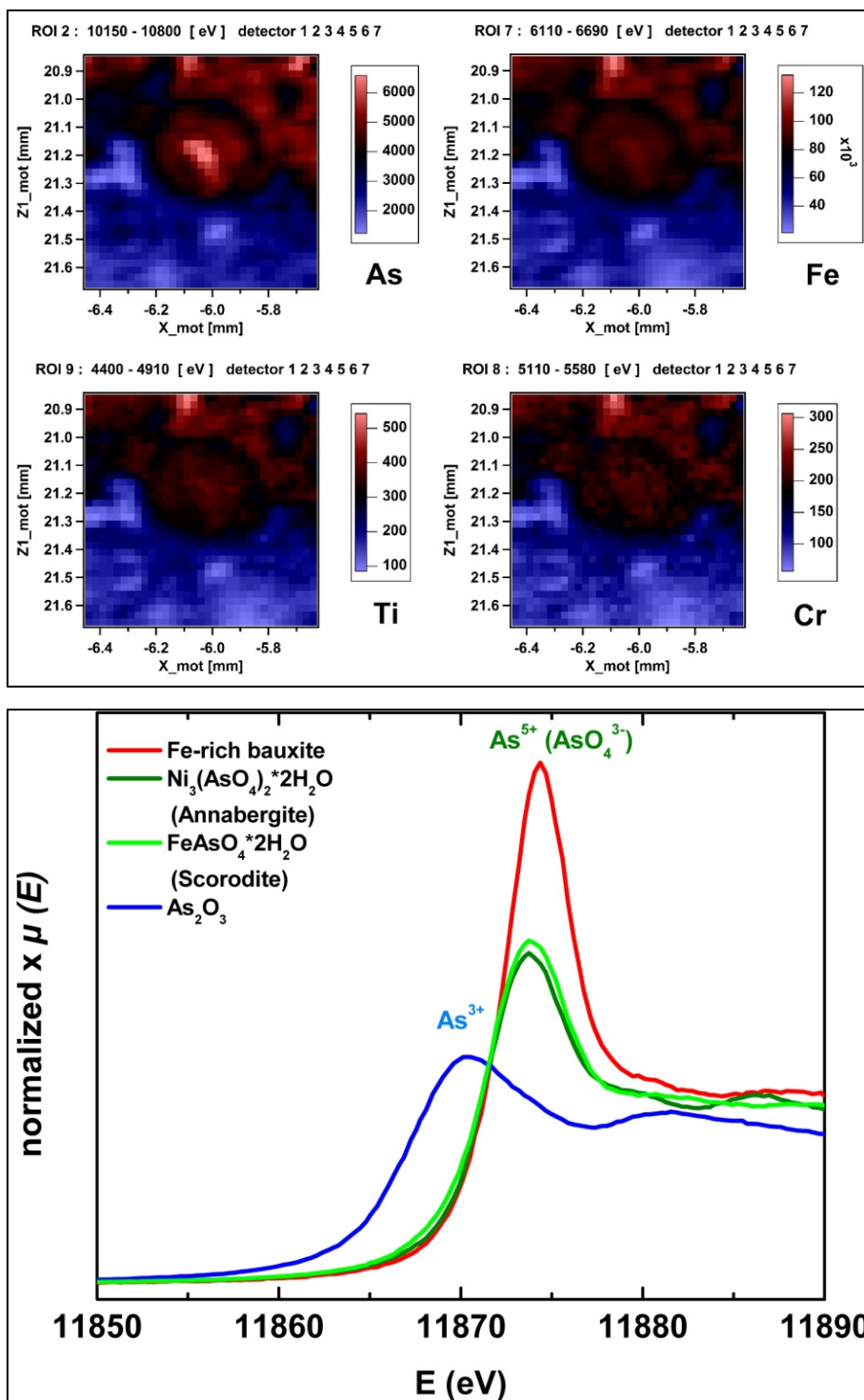
Figure S10: Mediterranean bauxite belt MED-normalized [26-41] spider diagrams for the studied Fe-rich (upper image) and Fe-depleted bauxite (lower image). Transparent light green background: depletion of average values; transparent light red background: enrichment of average values.
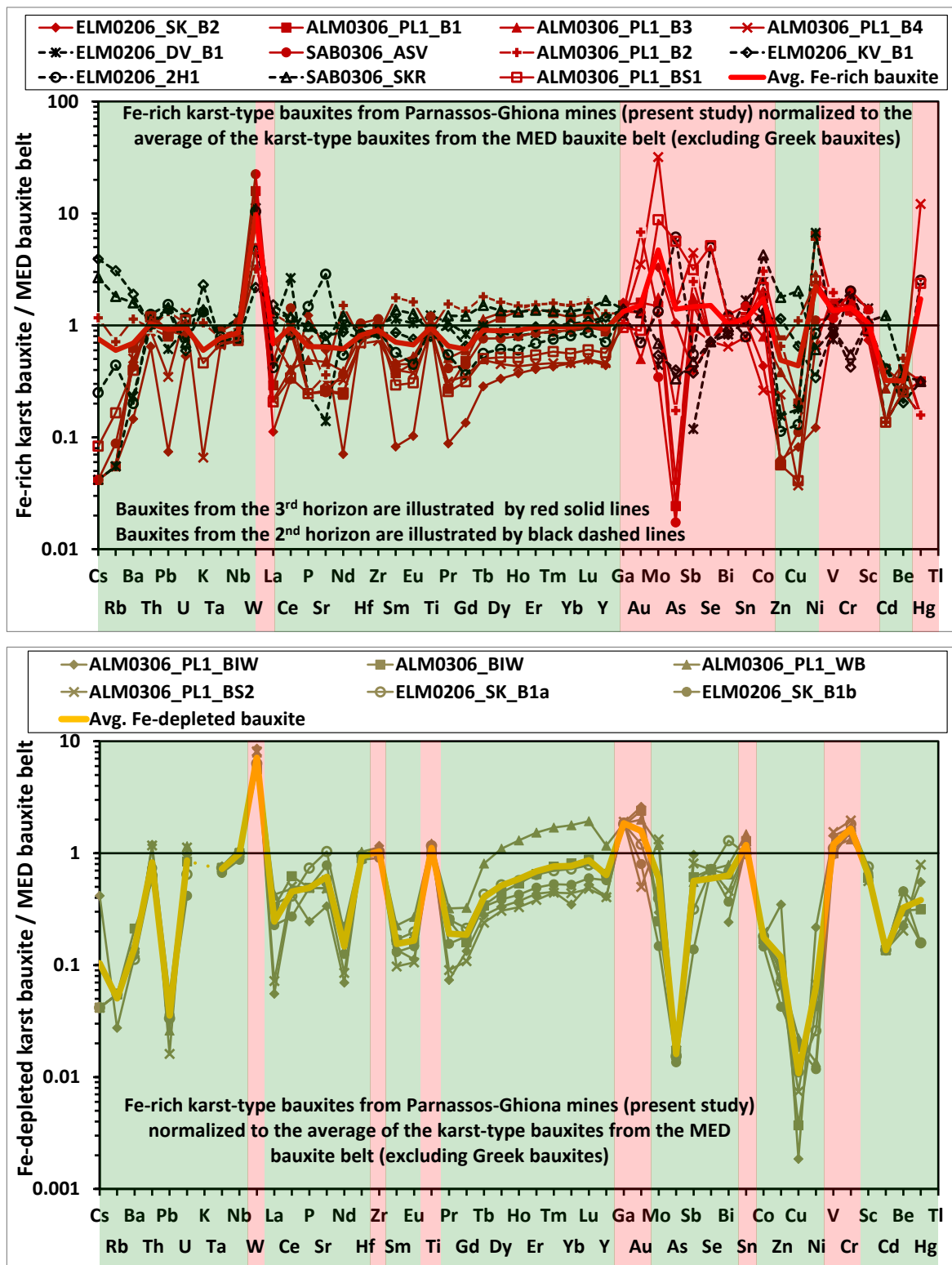
Figure S11: Binary diagram of Fe_2O_3 vs Al_2O_3 showing the correlation between Fe-Al for the studied Parnassos-Ghiona bauxites.
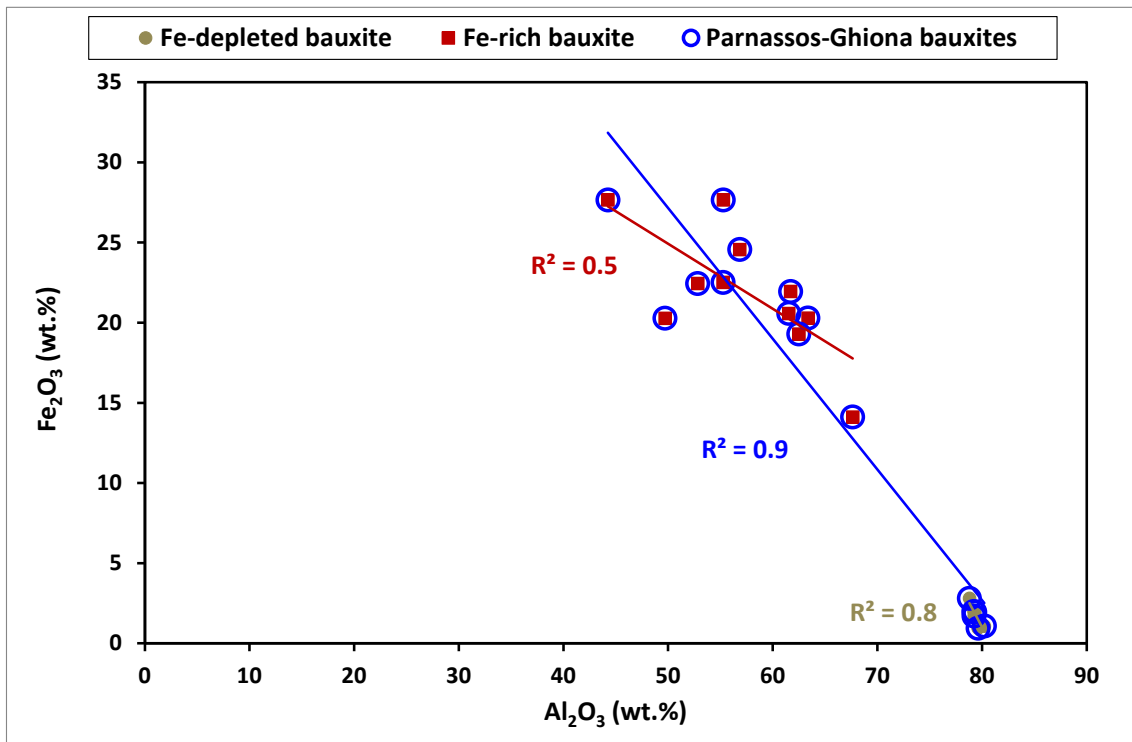
Figure S12: Binary diagram of Zr, Ti, Nb, and Hf illustrating the correlation between the less mobile lithophile High Field Strength Elements / HFSE (upper image), as well as binary plot between Ga and Al_2O_3 (lower image), illustrating their correlation for the studied Parnassos-Ghiona bauxites.
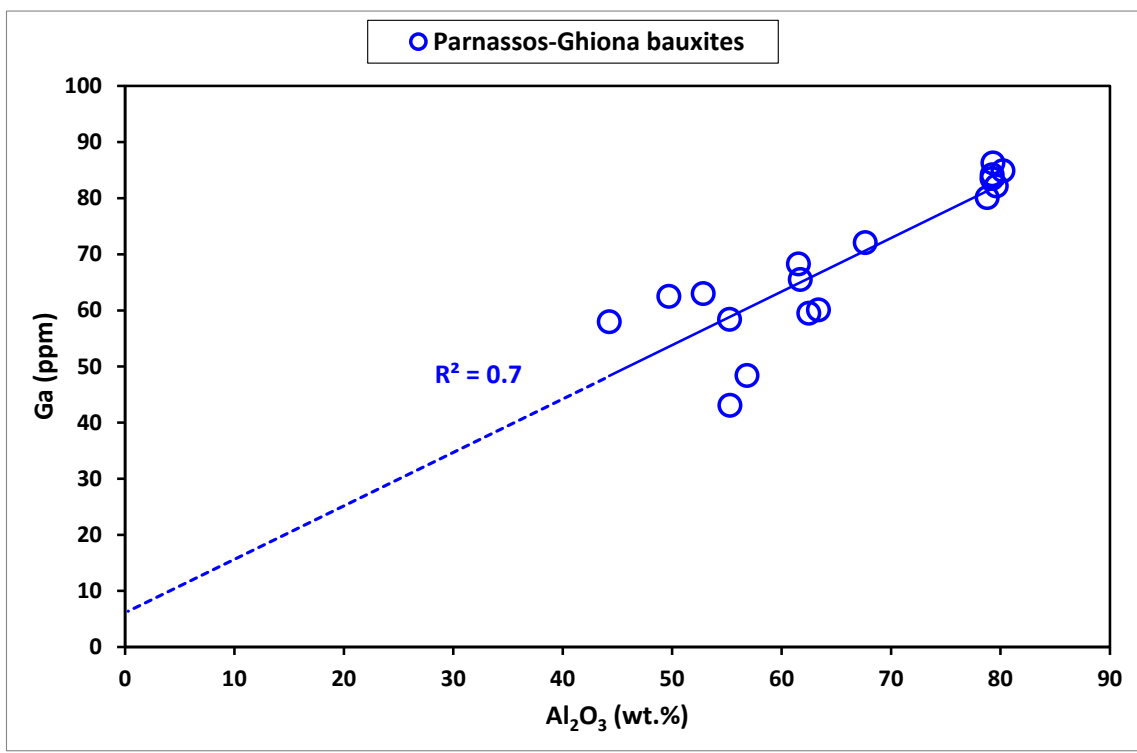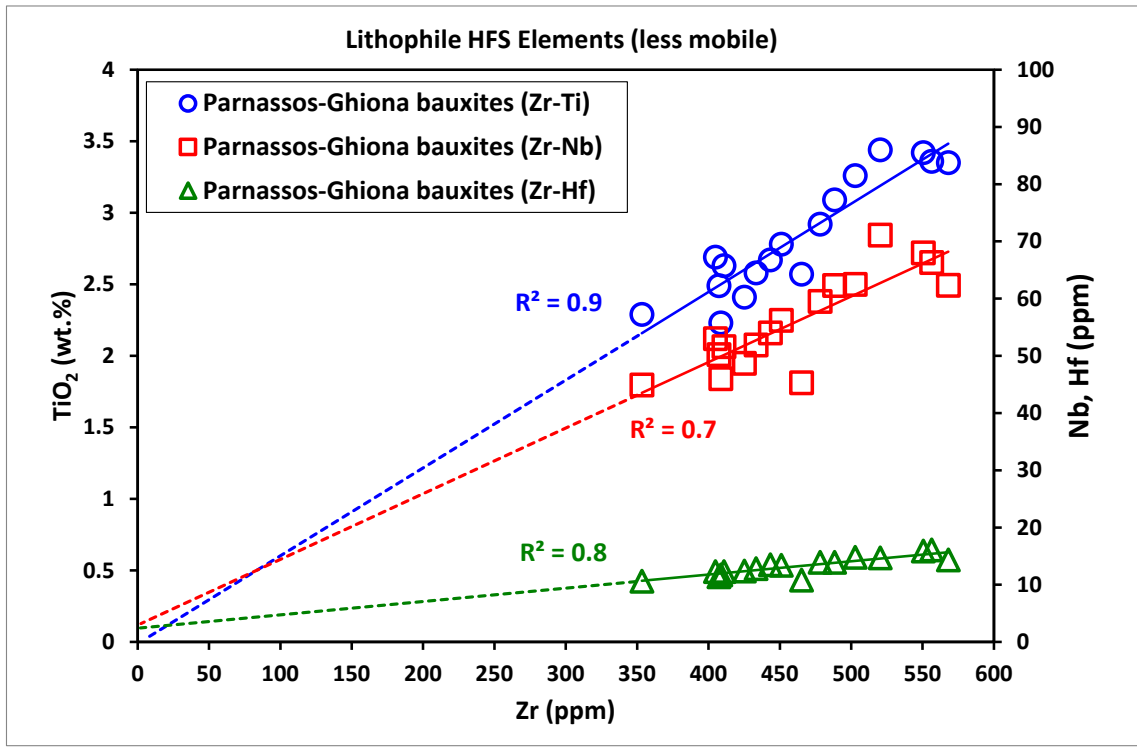
Figure S13: REE NASC-normalized [42] diagrams for the studied Fe-rich (upper image) and Fe-depleted bauxites (middle image). The averages for all chemical elements occurring in Parnassos-Ghiona bauxites are also presented (lower image; transparent light red background: Ce positive anomaly and Gd positive geochemical anomaly).
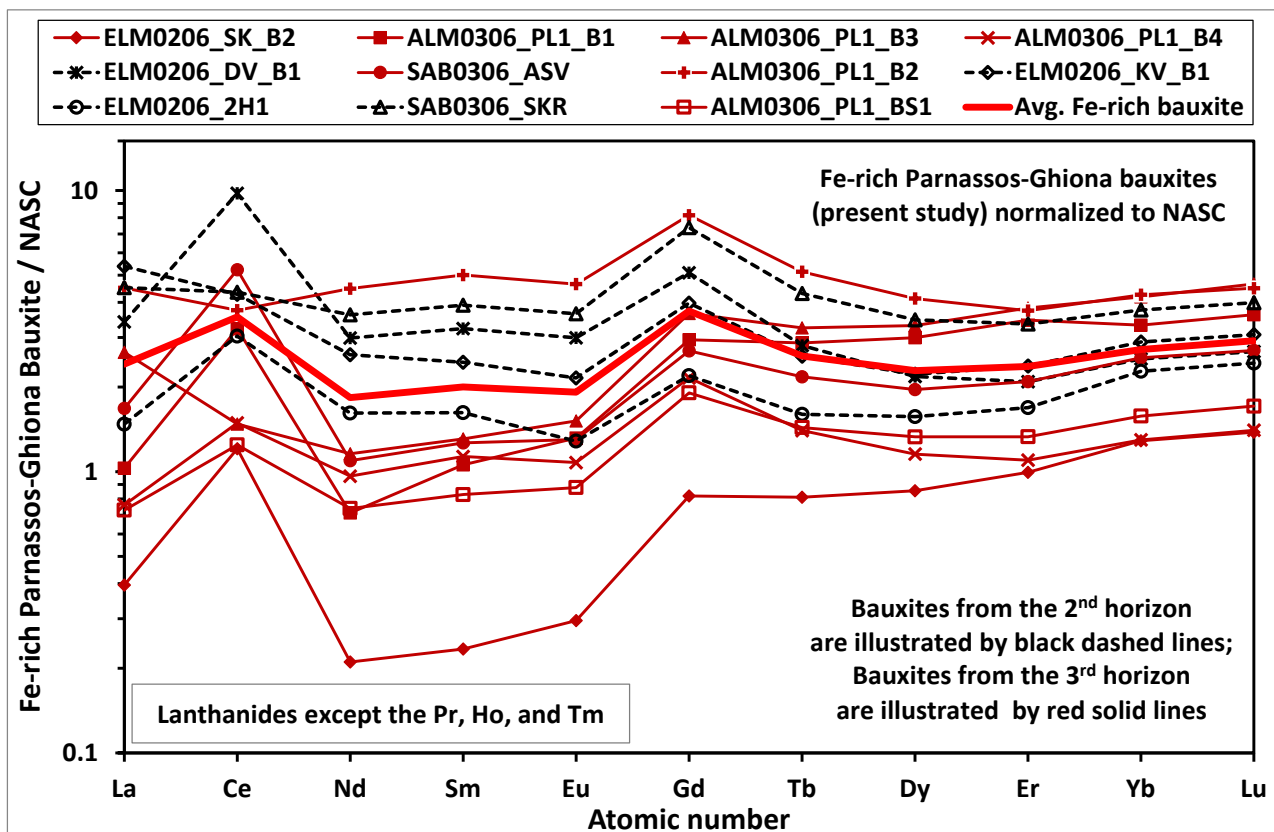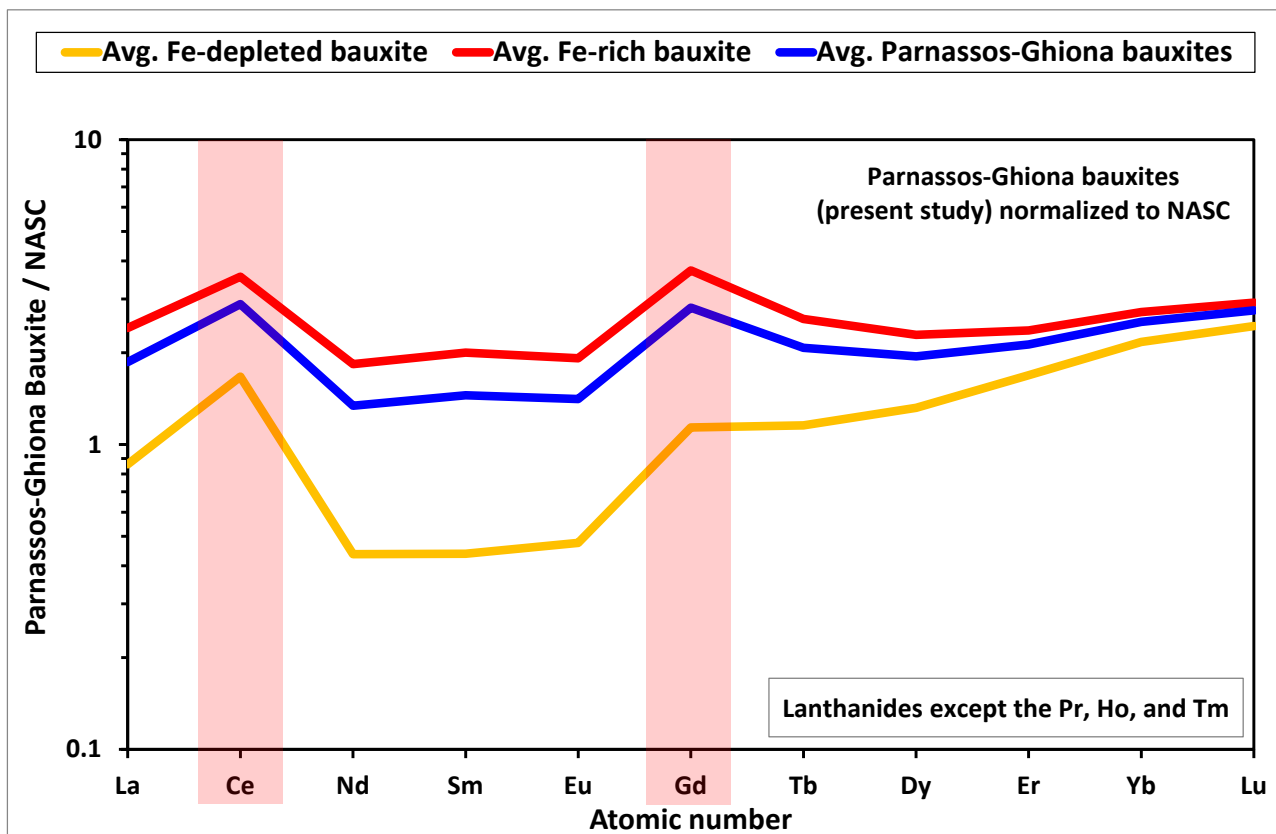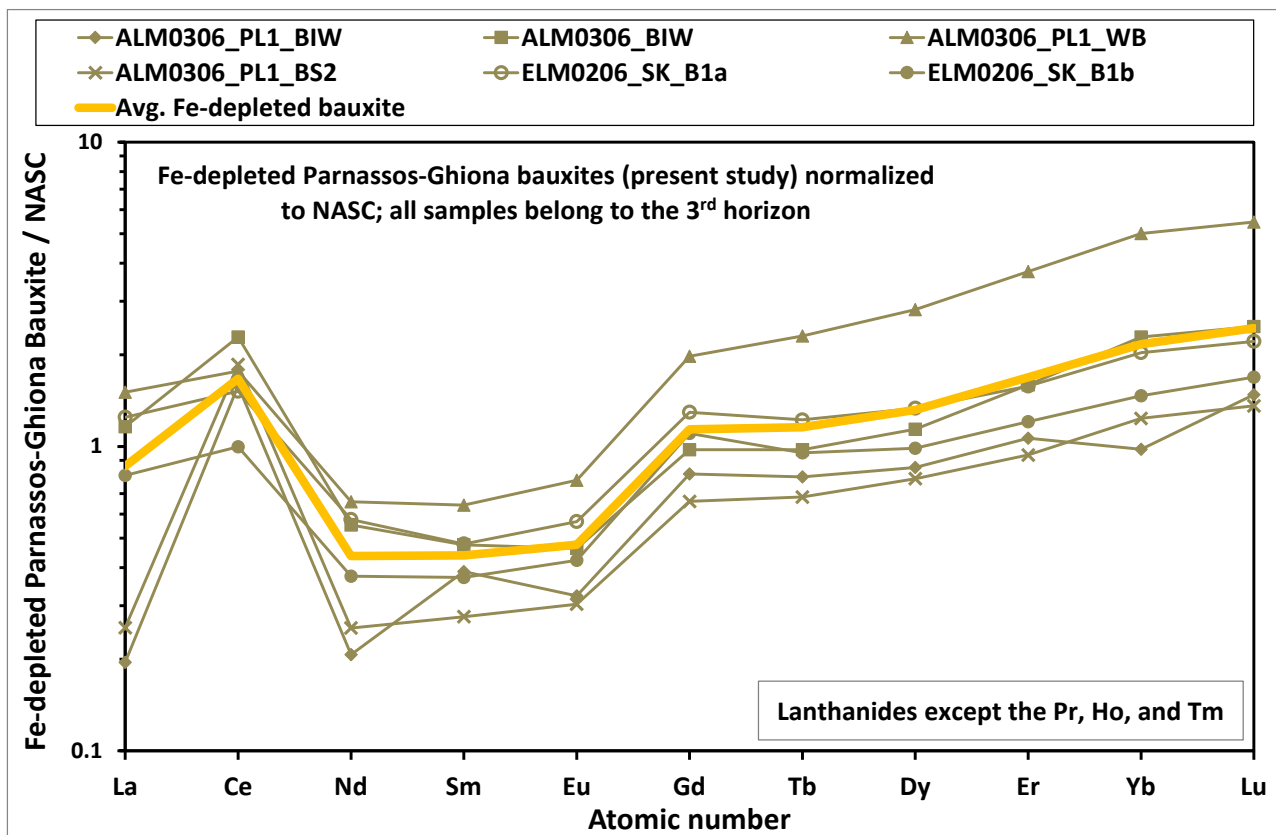
Figure S14: Comparative REE chondrite-normalized diagrams initially using all the chondrite values from literature (upper image) and finally utilizing the selected ones (lower image), according to suggestions provided by Rollinson (1993) [20] and Korotev (2010) [21].
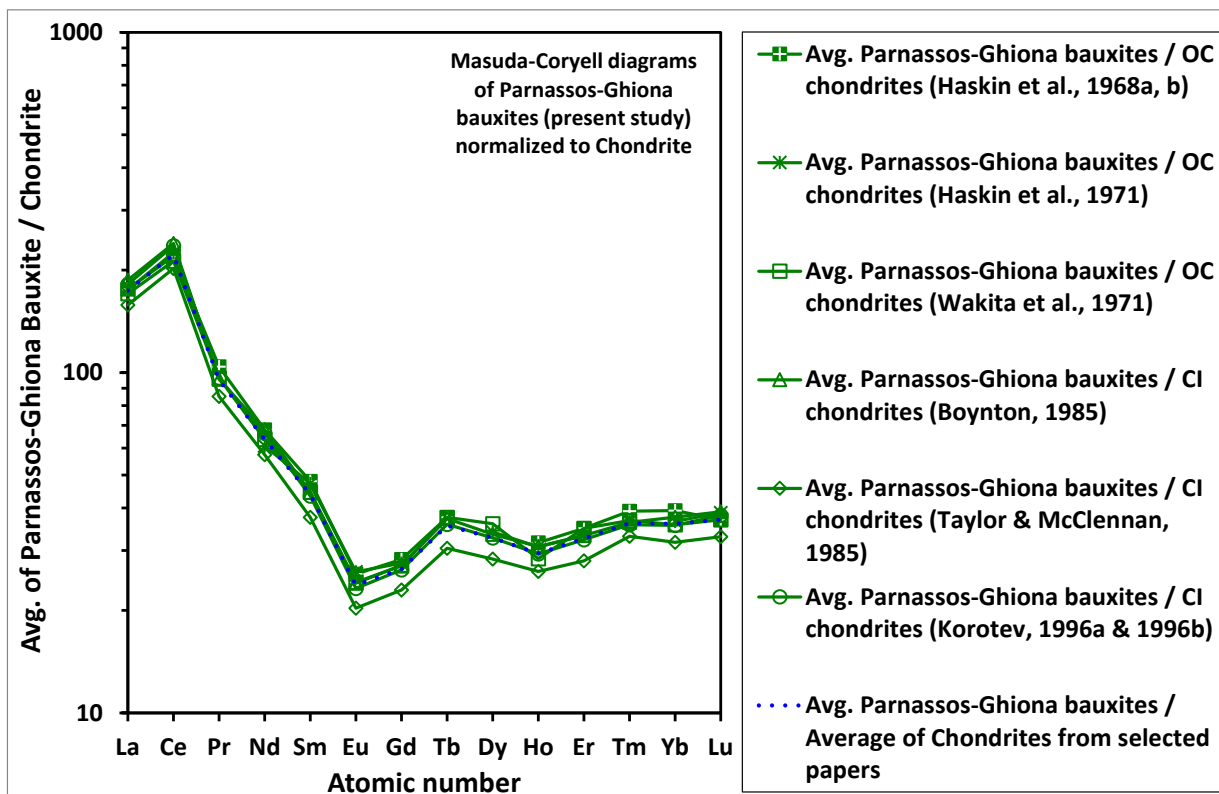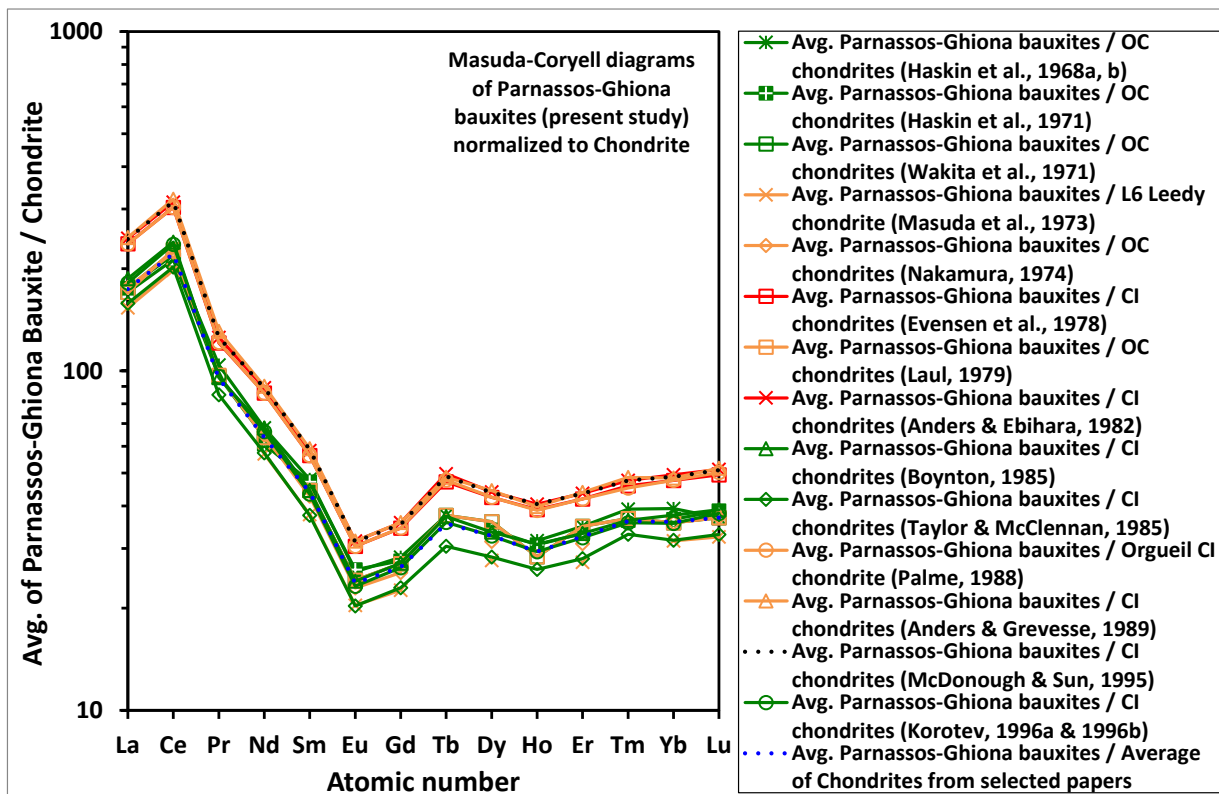
Figure S15: REE chondrite-normalized [10-17] diagrams for the studied Fe-rich (upper image) and Fe-depleted bauxites (middle image). The average for all chemical elements occurring in Parnassos-Ghiona bauxites is also presented (lower image; transparent light red background: Ce positive anomaly, and transparent light red background: Eu negative geochemical anomaly).
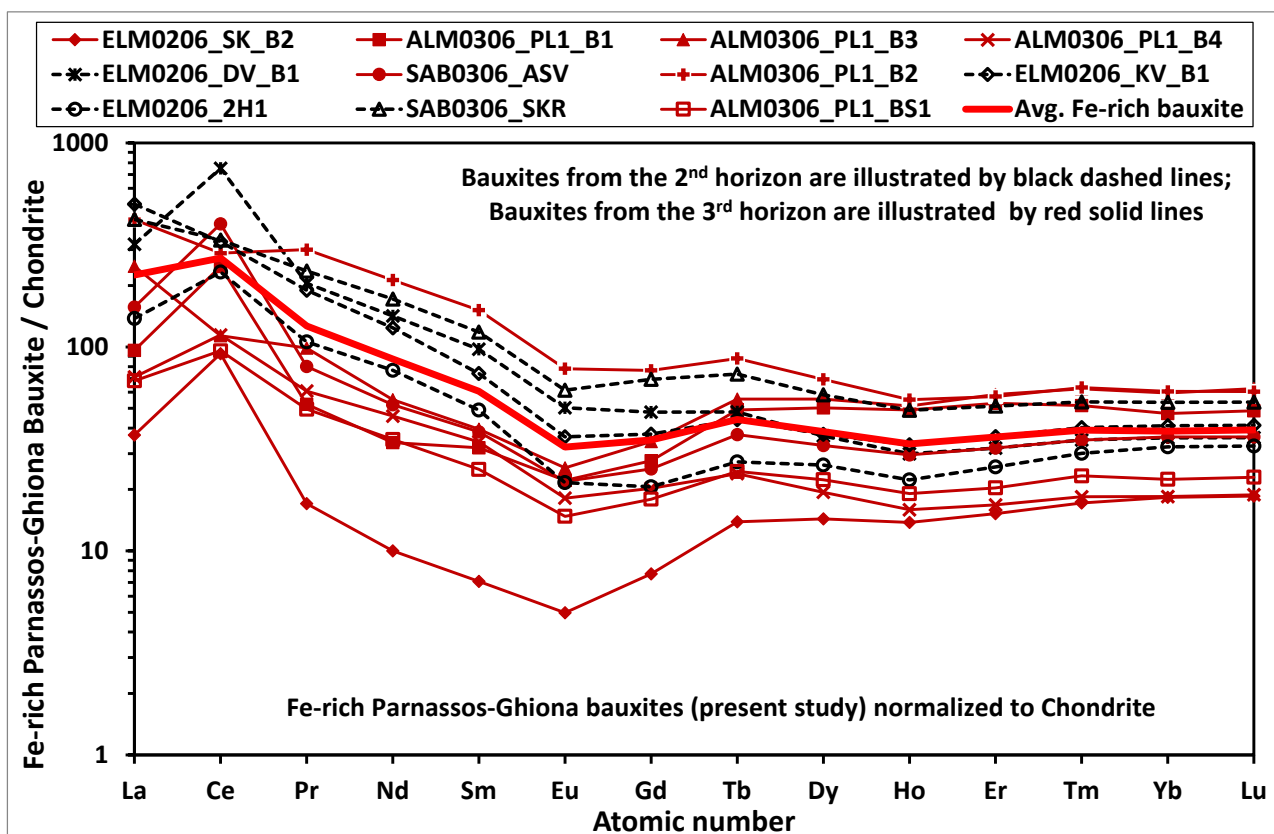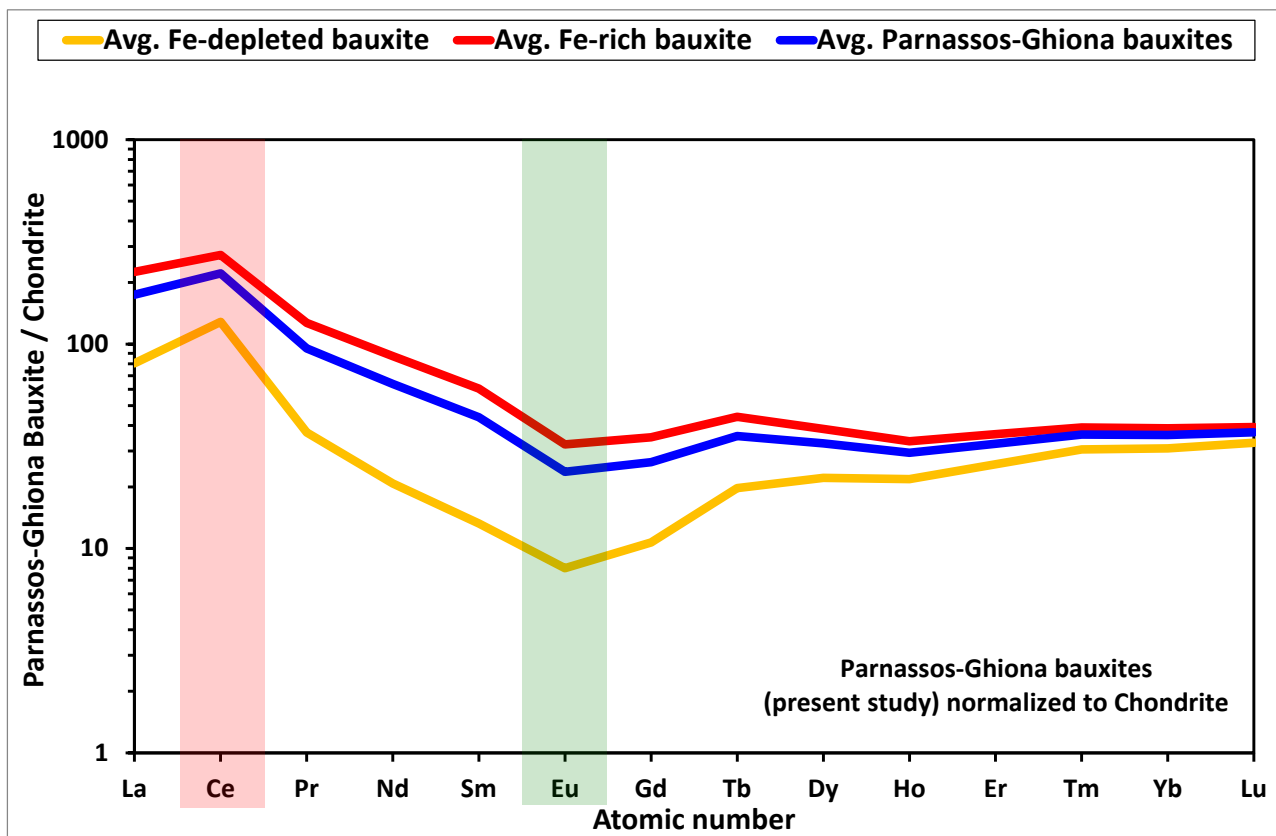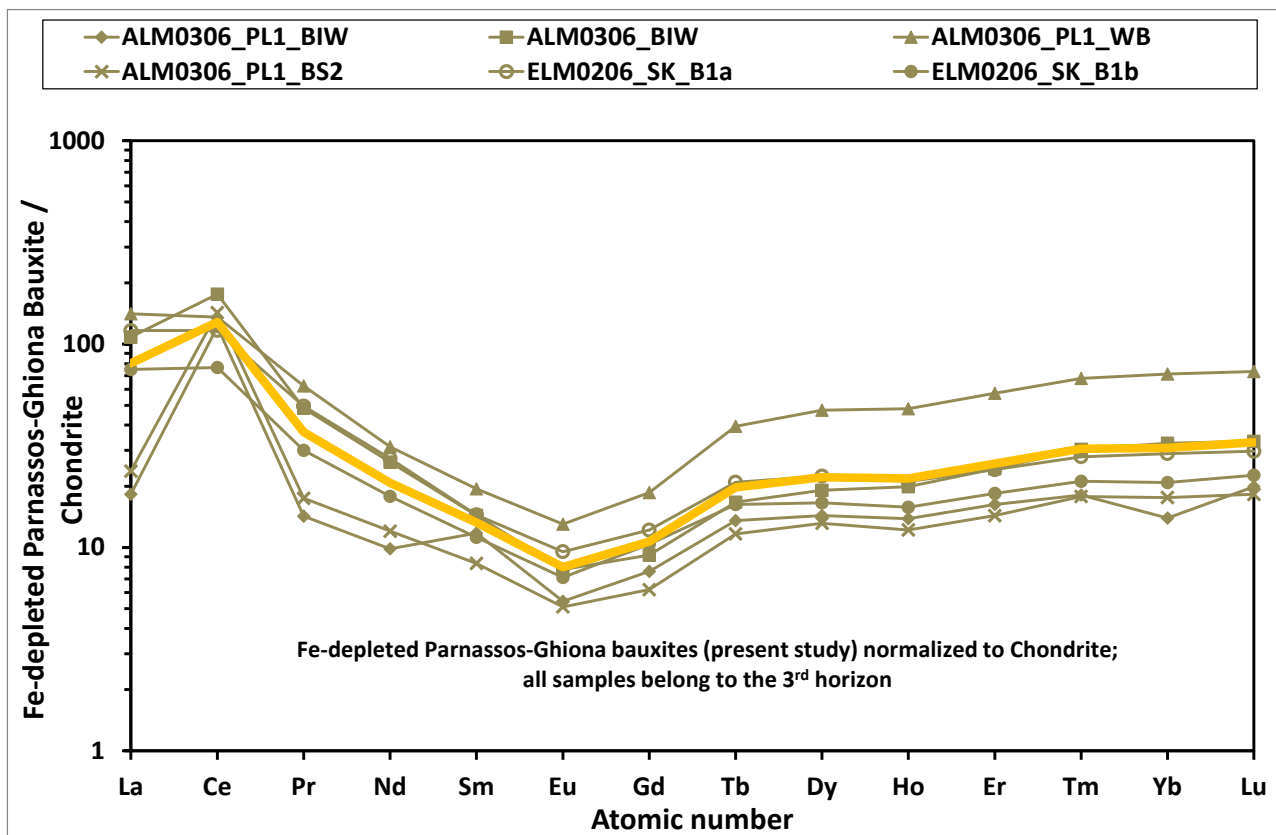
Figure S16: REE ES-normalized [43] diagrams for the studied Fe-rich (upper image) and Fe-depleted bauxites (middle image). The average for all chemical elements occurring in Parnassos-Ghiona bauxites is also presented (lower image; transparent light red background: Ce positive anomaly).

Fe-depleted Parnassos-Ghiona bauxites (present study) normalized to European Shale (ES); all samples belong to the 3rd horizon

Lanthanides except the Dy

ALM0306_PL1_BIW
ALM0306_BIW
ALM0306_PL1_WB
ALM0306_PL1_BS2
ELM0206_SK_B1a
ELM0206_SK_B1b
Avg. Fe-depleted bauxite

Parnassos-Ghiona bauxites (present study) normalized to European Shale (ES)

Lanthanides except the Dy

Avg. Fe-depleted bauxite
Avg. Fe-rich bauxite
Avg. Parnassos-Ghiona bauxites
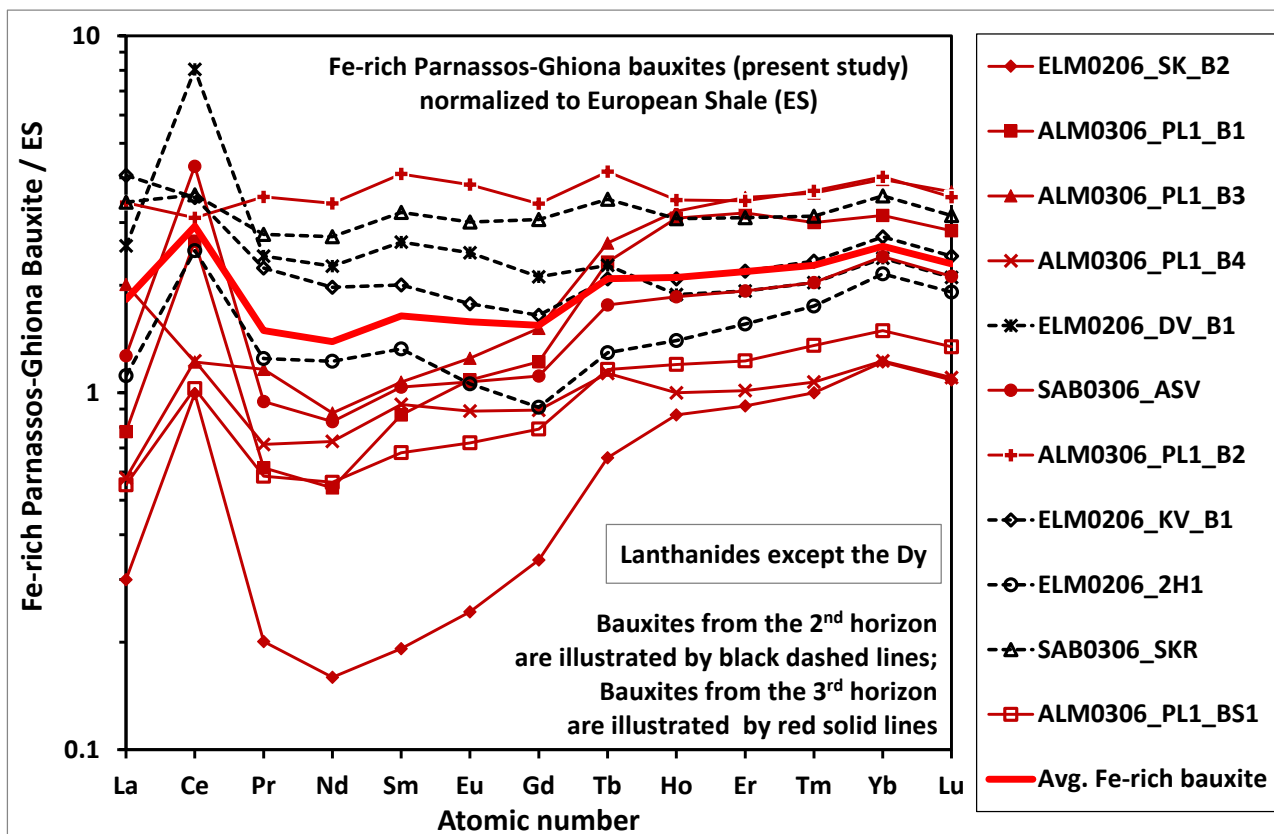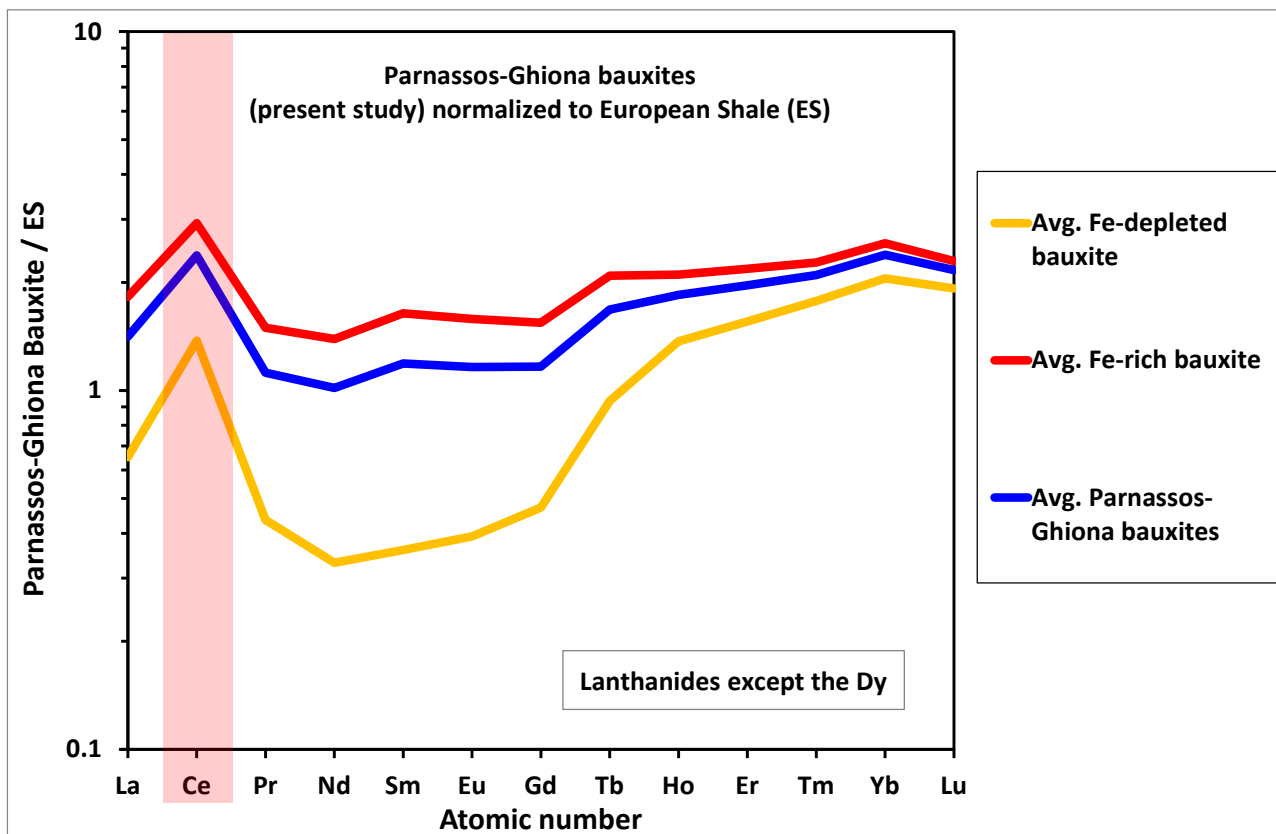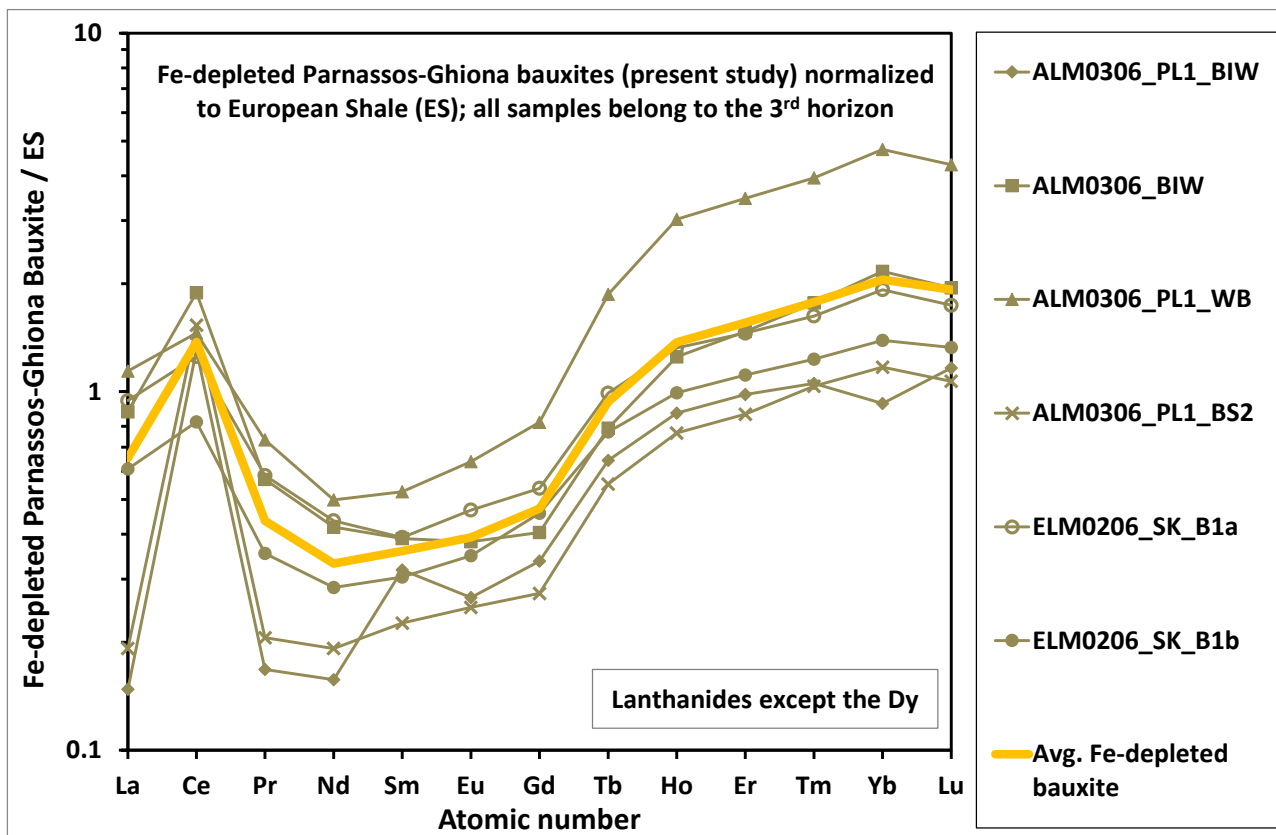
Figure S17: REE UCC-normalized [25] diagrams for the studied Fe-rich (upper image) and Fe-depleted bauxites (middle image). The average for all chemical elements occurring in Parnassos-Ghiona bauxites is also presented (lower image; transparent light red background: Ce positive anomaly).
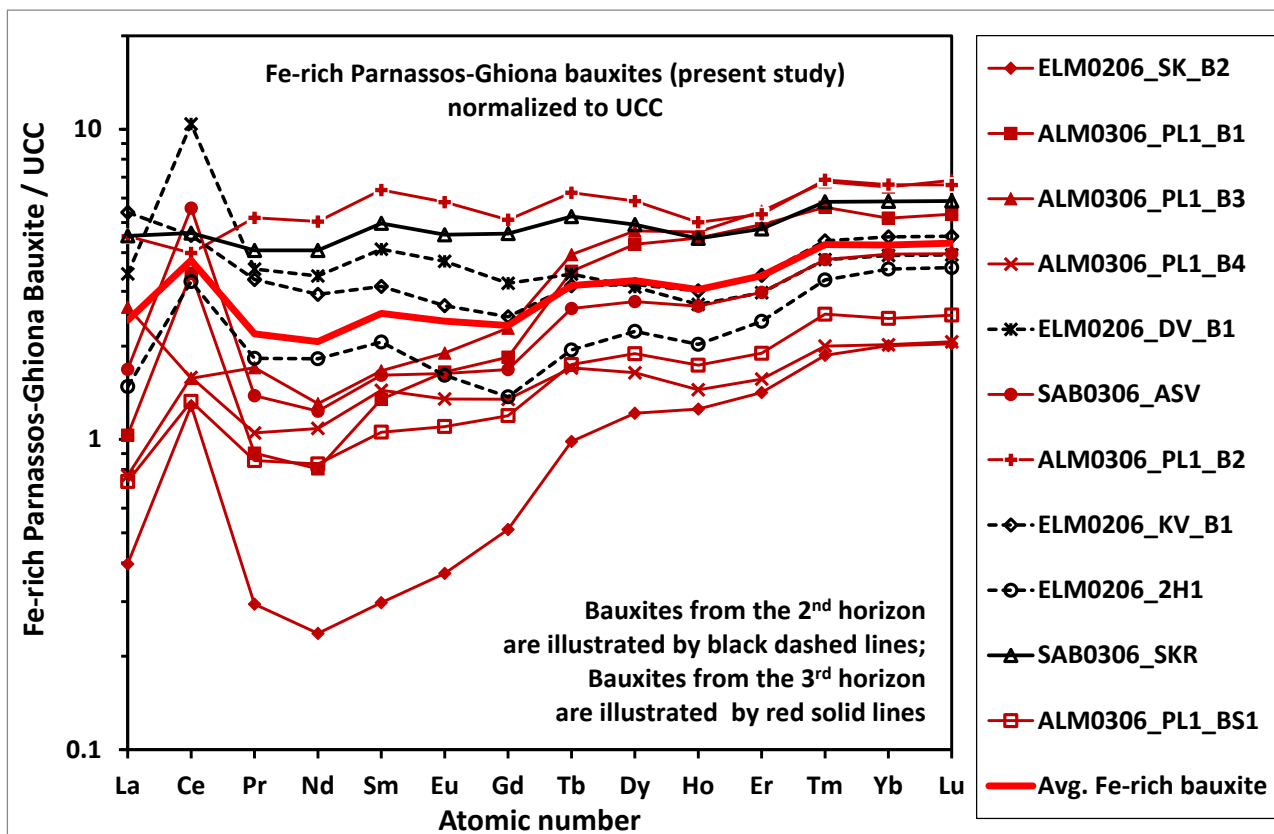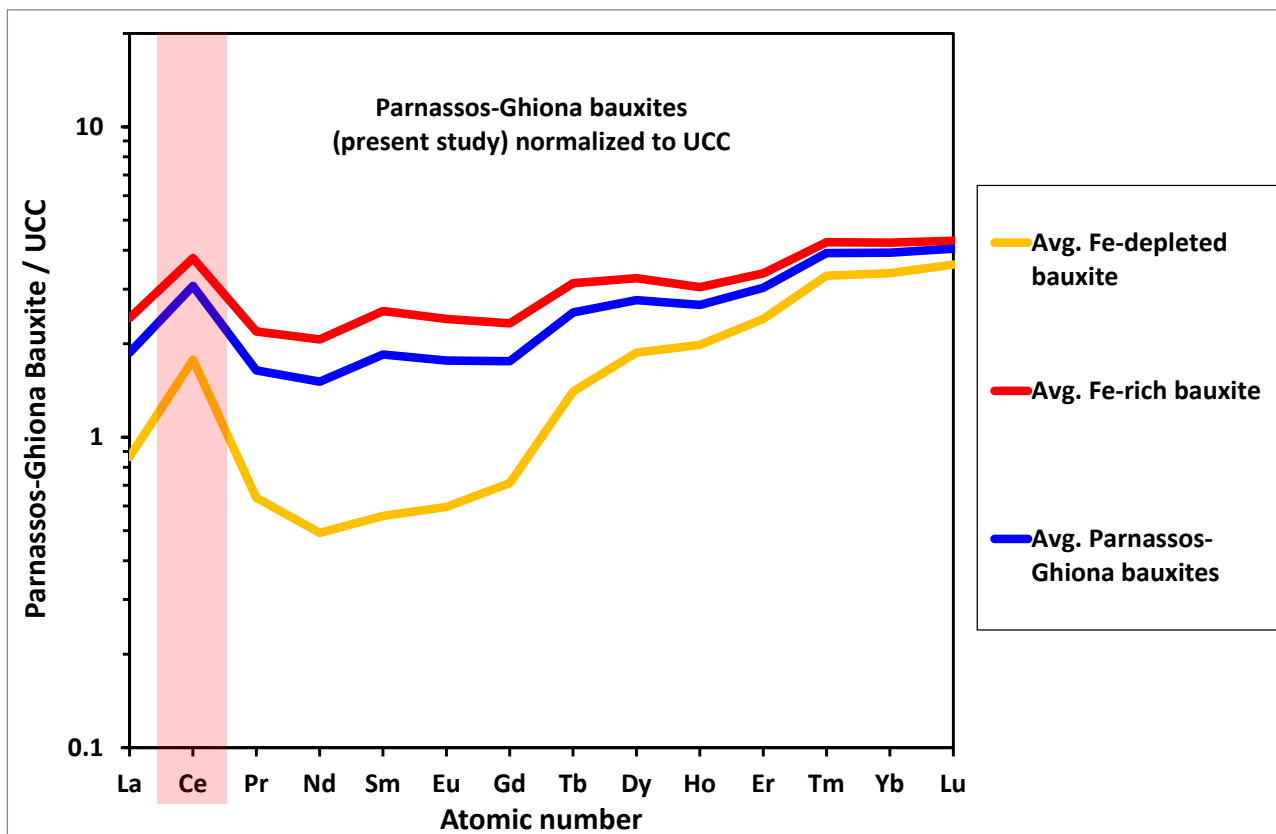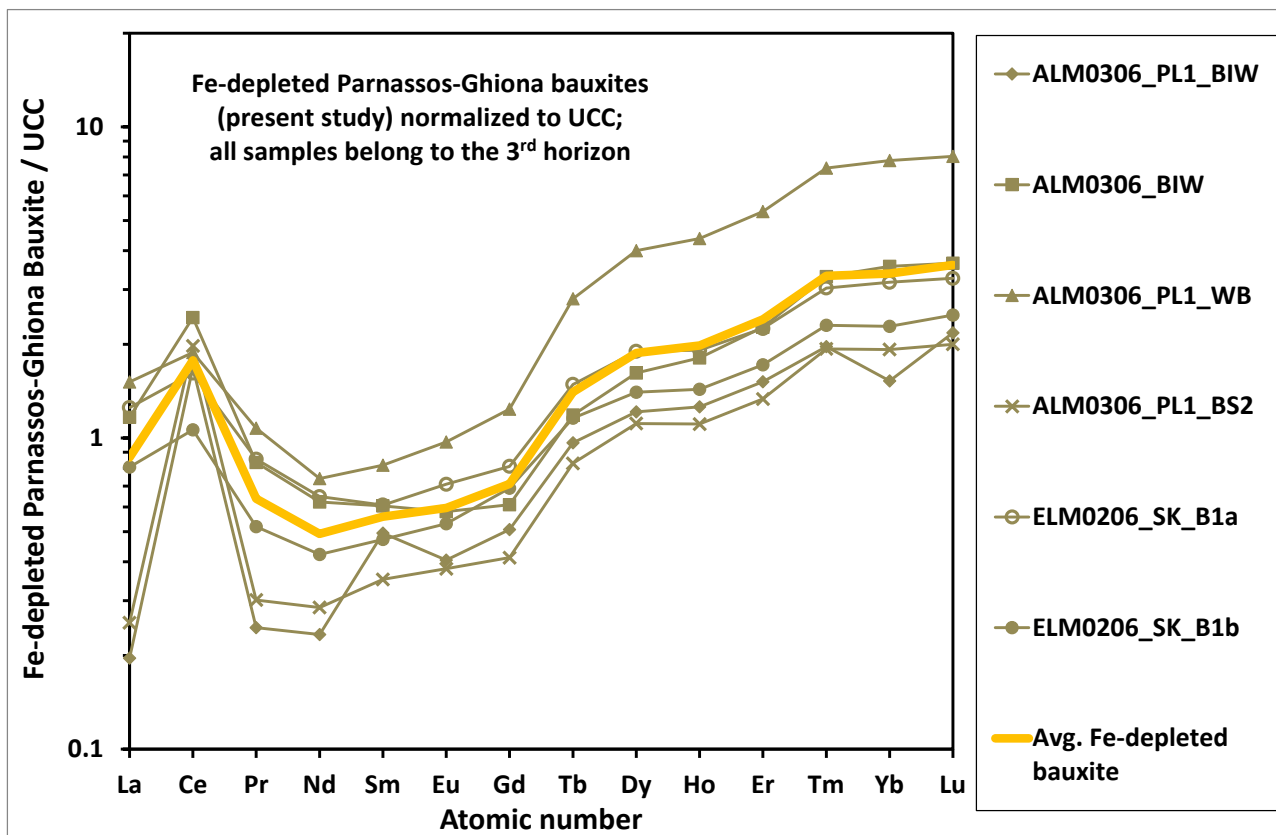
Figure S18: REE PAAS-normalized [16, 44] diagrams for the studied Fe-rich (upper image) and Fe-depleted bauxites (middle image). The average for the REE occurring in the studied bauxites is also presented (lower image; transparent light red background: Ce positive anomaly).

Figure S18: Continuing

Fe-depleted Parnassos-Ghiona bauxites (present study) normalized to Post Archaean average Australian Sedimentary rock (PAAS); all samples belong to the 3rd horizon

Legend:
- ALM0306_PL1_BIW
- ALM0306_BIW
- ALM0306_PL1_WB
- ALM0306_PL1_BS2
- ELM0206_SK_B1a
- ELM0206_SK_B1b
- Avg. Fe-depleted bauxite

Parnassos-Ghiona bauxites (present study) normalized to Post Archaean average Australian Sedimentary rock(PAAS)

Legend:
- Avg. Fe-depleted bauxite
- Avg. Fe-rich bauxite
- Avg. Parnassos-Ghiona bauxites

Figure S19: Rare earth element abundances normalized to the average of the karst-type bauxites from the Mediterranean bauxite belt MED-normalized [26-41] for the studied Fe-rich (upper image) and Fe-depleted bauxite (middle image). The average for all chemical elements occurring in Parnassos-Ghiona bauxites is also presented (lower image; transparent light red background: Ce positive anomaly).

Figure S19: Continuing

Figure S20: The coal interstratified between the bauxite ore and the black to dark bituminous hanging wall limestone, at the mining front of Pera Lakkos underground mine. The ordinary white footwall limestone and the Fe-rich/sulfide-bearing bauxite as well as the Fe-rich and the Fe-depleted bauxite are also illustrated. The lithostratigraphic column has been modified after Valeton et al., 1987 and Kalaitzidis et al., 2010 [45, 46 and references therein]
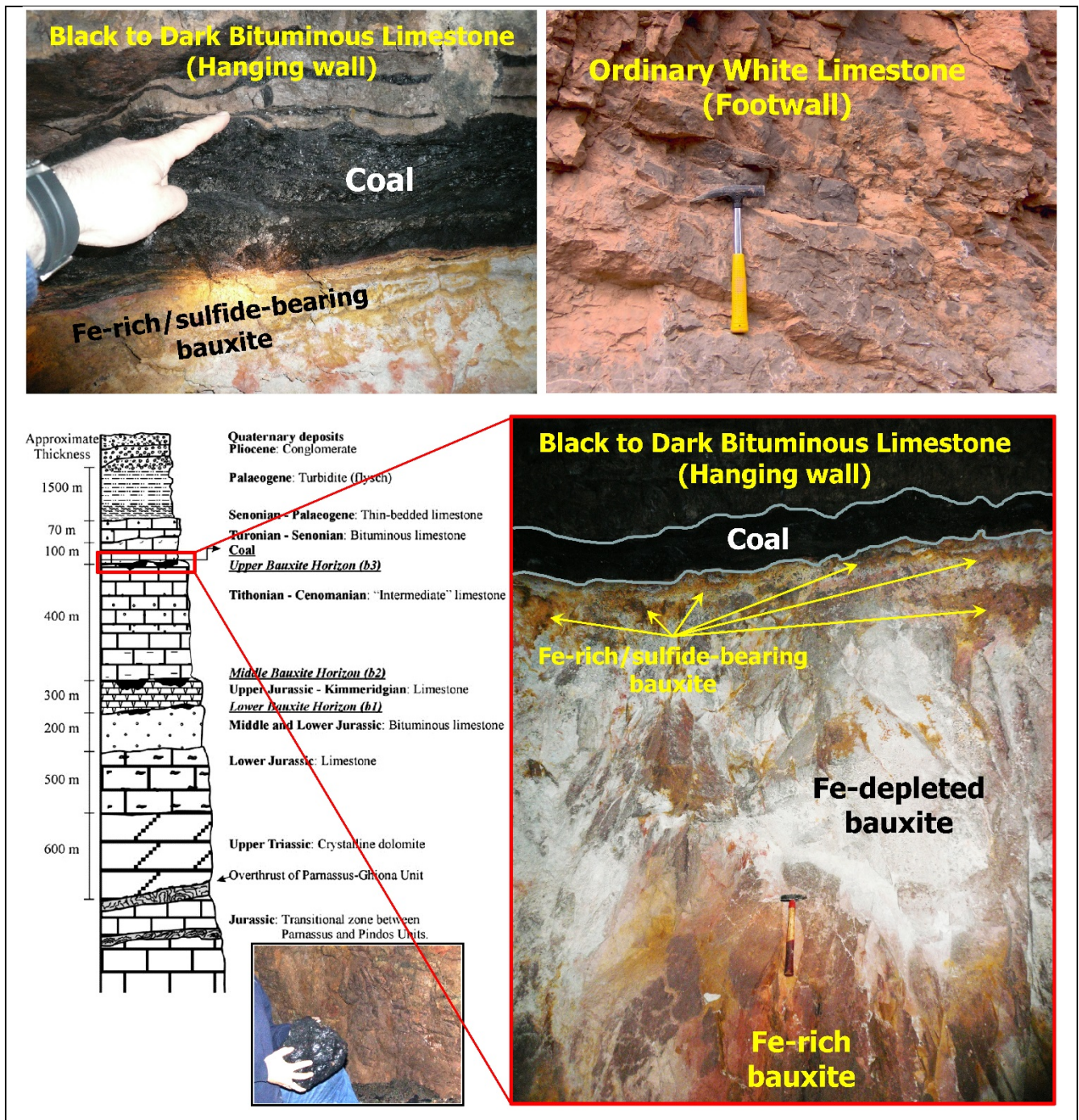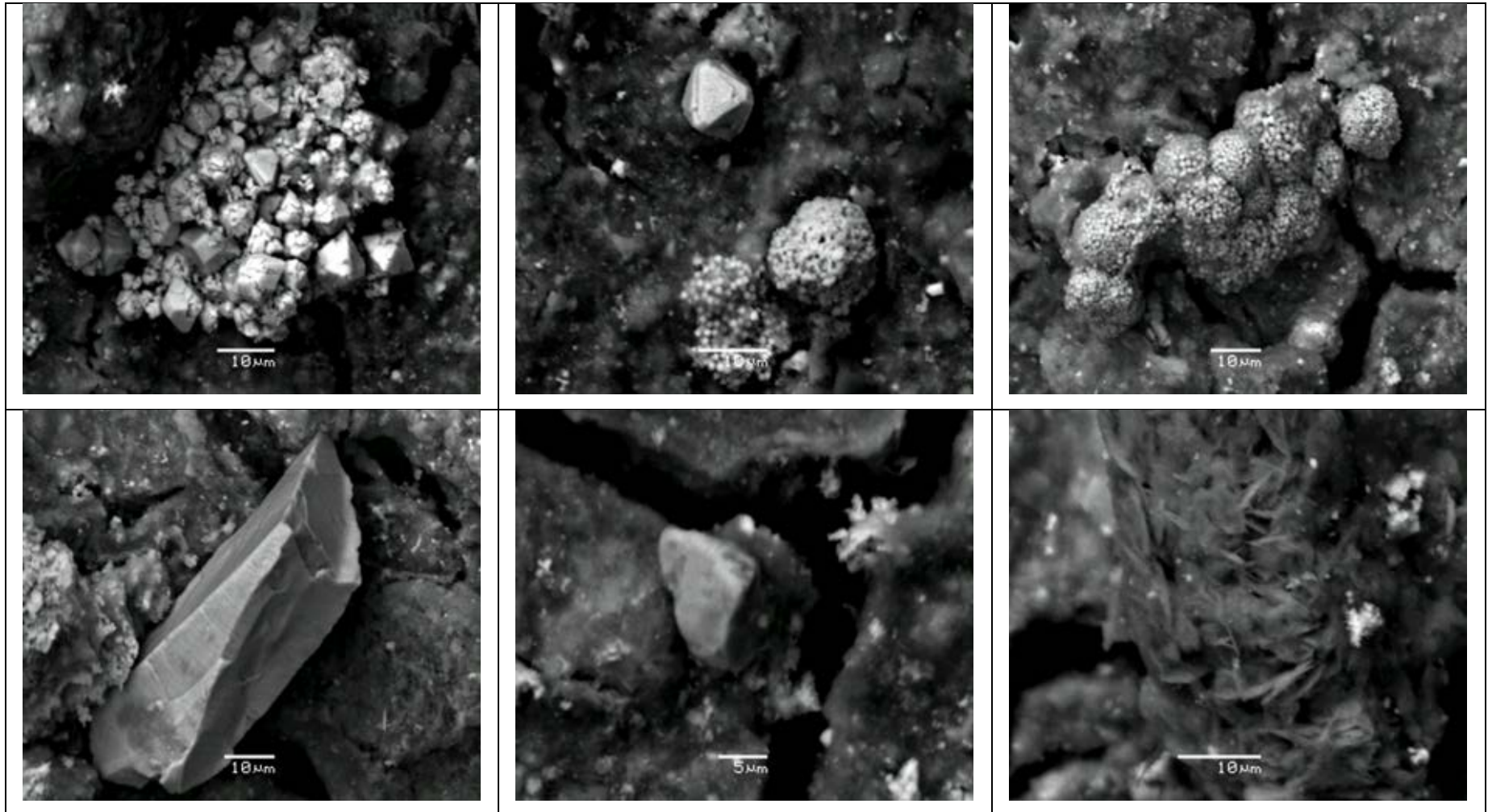
Figure S21: The UCC-normalized [25] spider diagrams for the studied dark (ALM0306_PL1_DLS2) and black (ALM0306_PL1_DLS1) hanging wall limestones, the coal layer (ALM0807_PL1_COAL), including its relevant flying ash (ALM0807_PL1_ASH), the Fe-rich/sulfide-bearing bauxite, the average of Fe-depleted bauxite (n=10), the average of Fe-rich bauxite (n=10), and the ordinary white footwall limestone (ALM0306_PL1_WLS) at the mining front of Pera Lakkos underground mine.
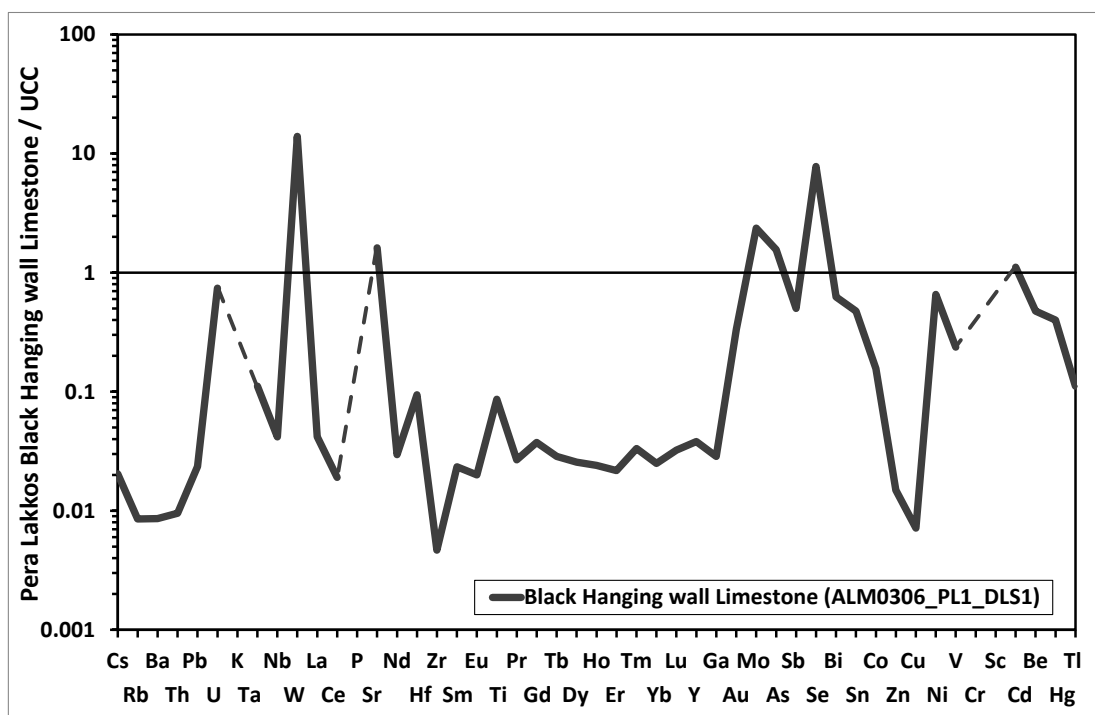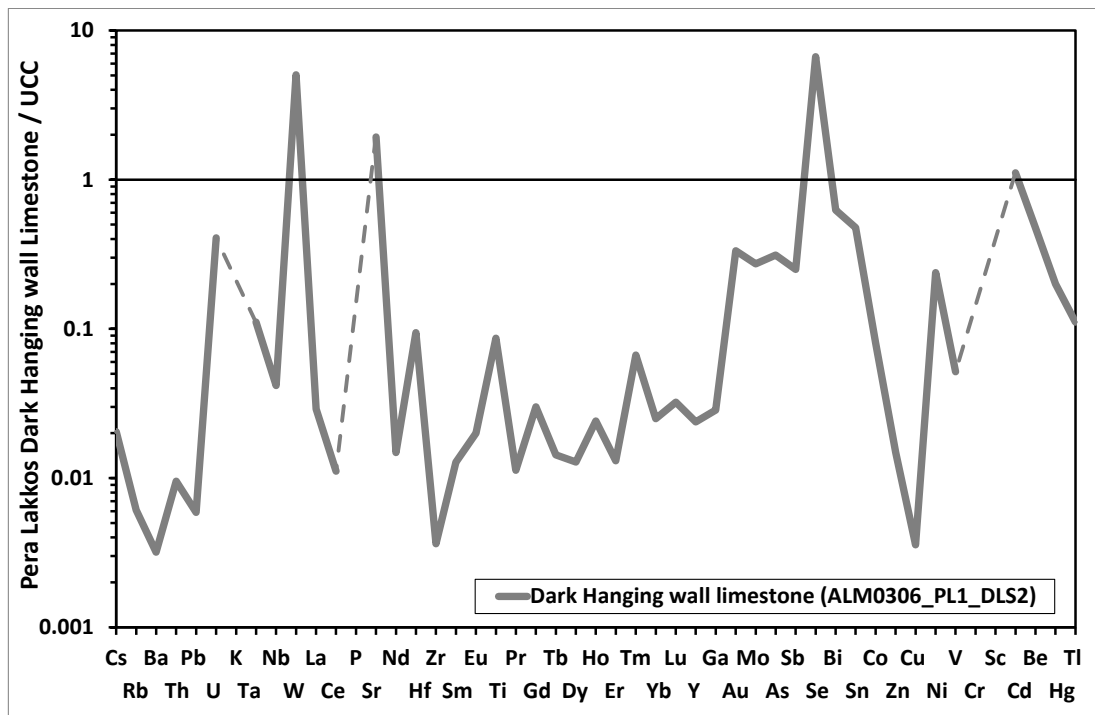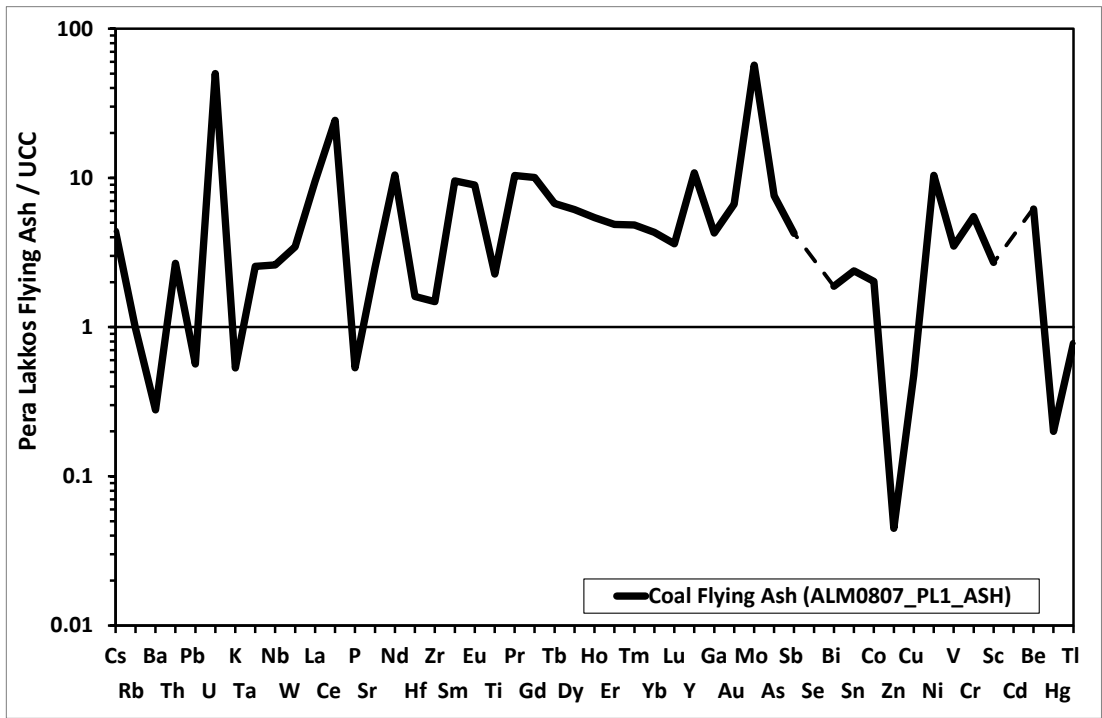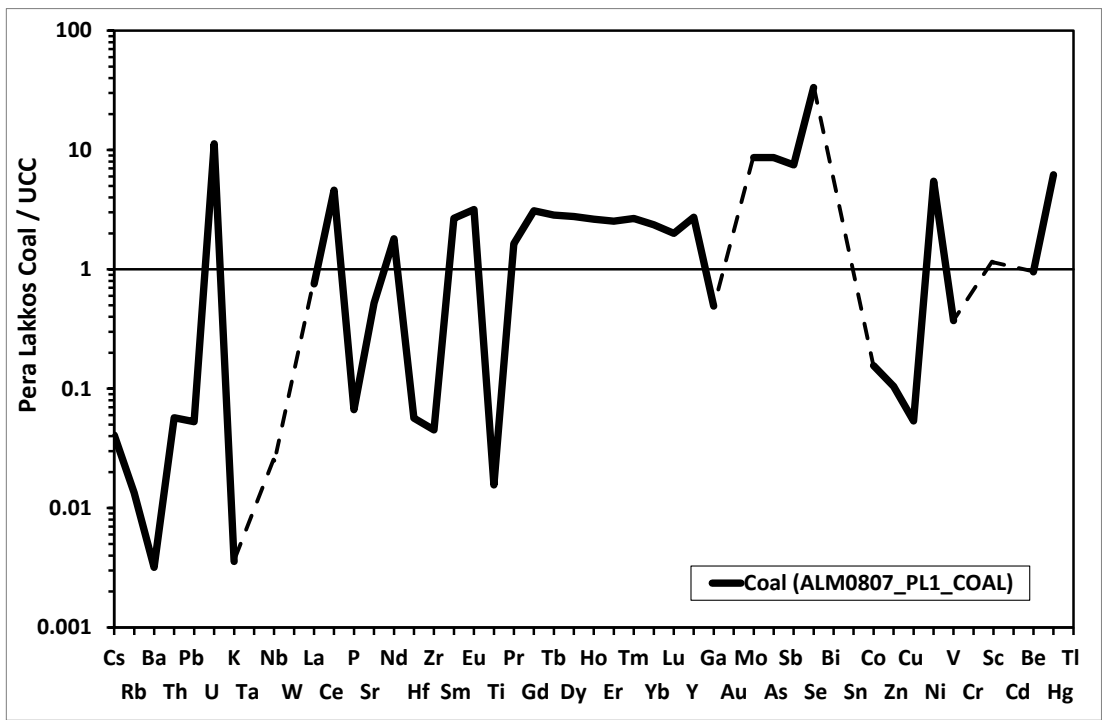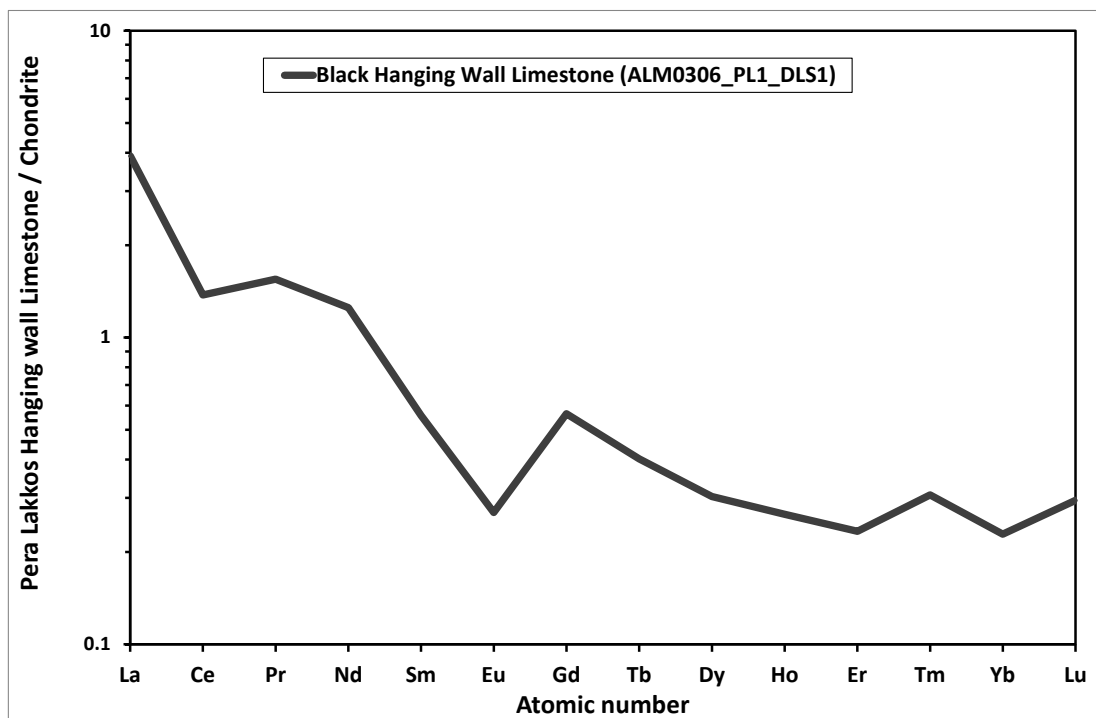
Figure 21: Continuing
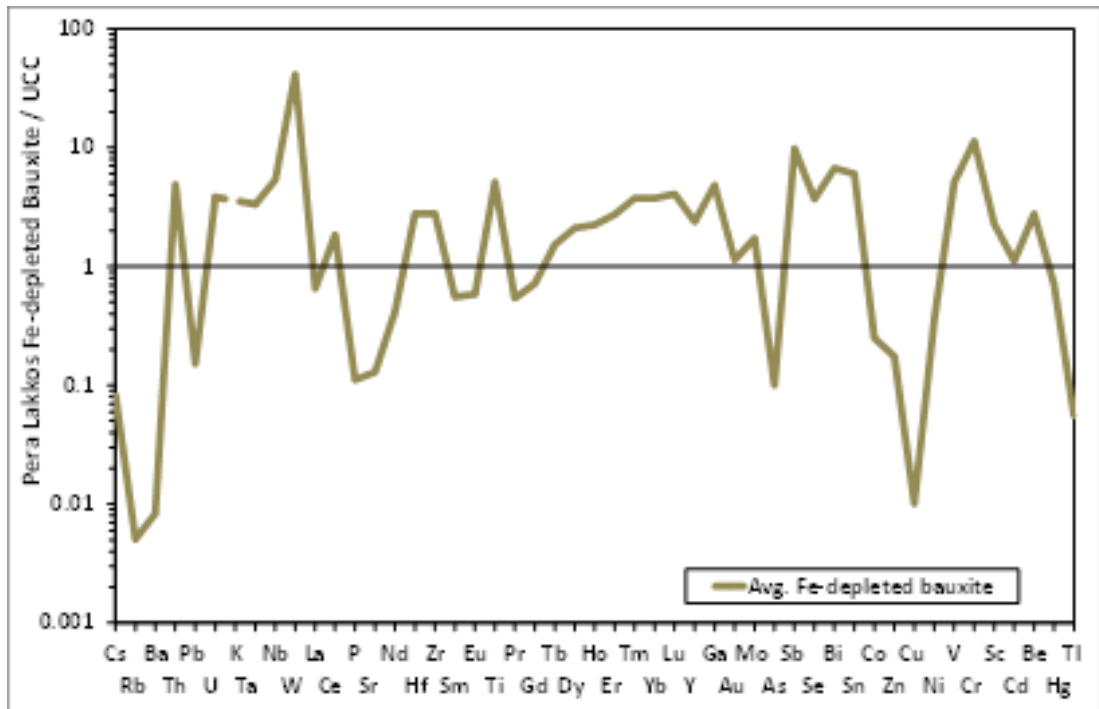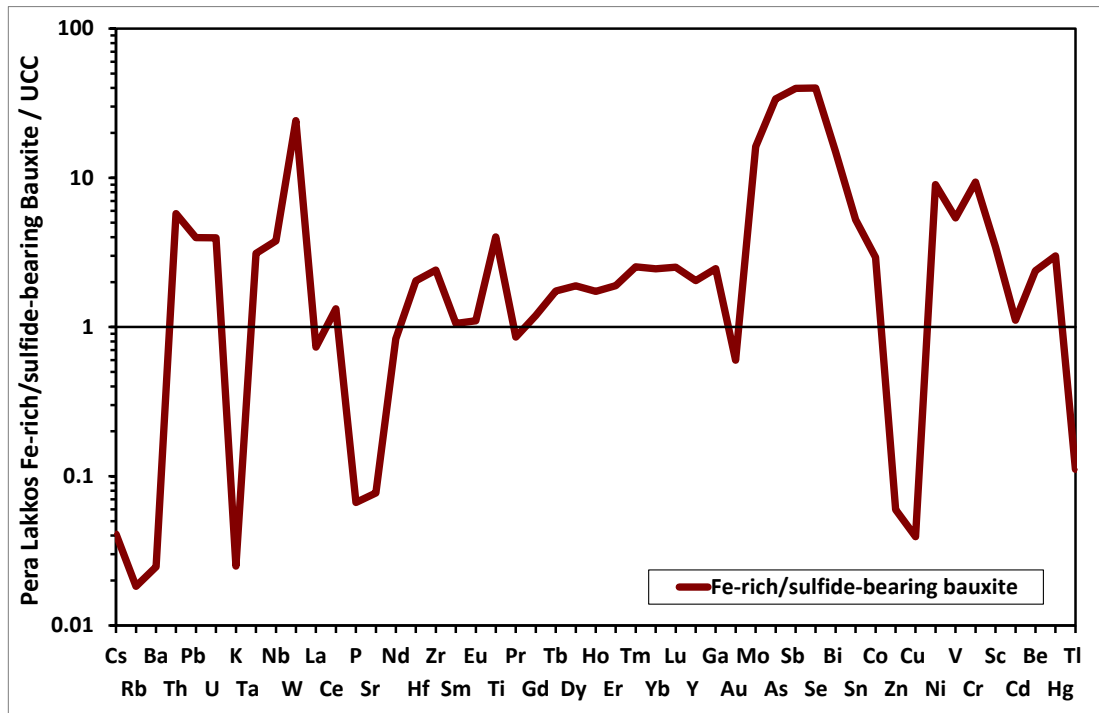
Figure 21: Continuing
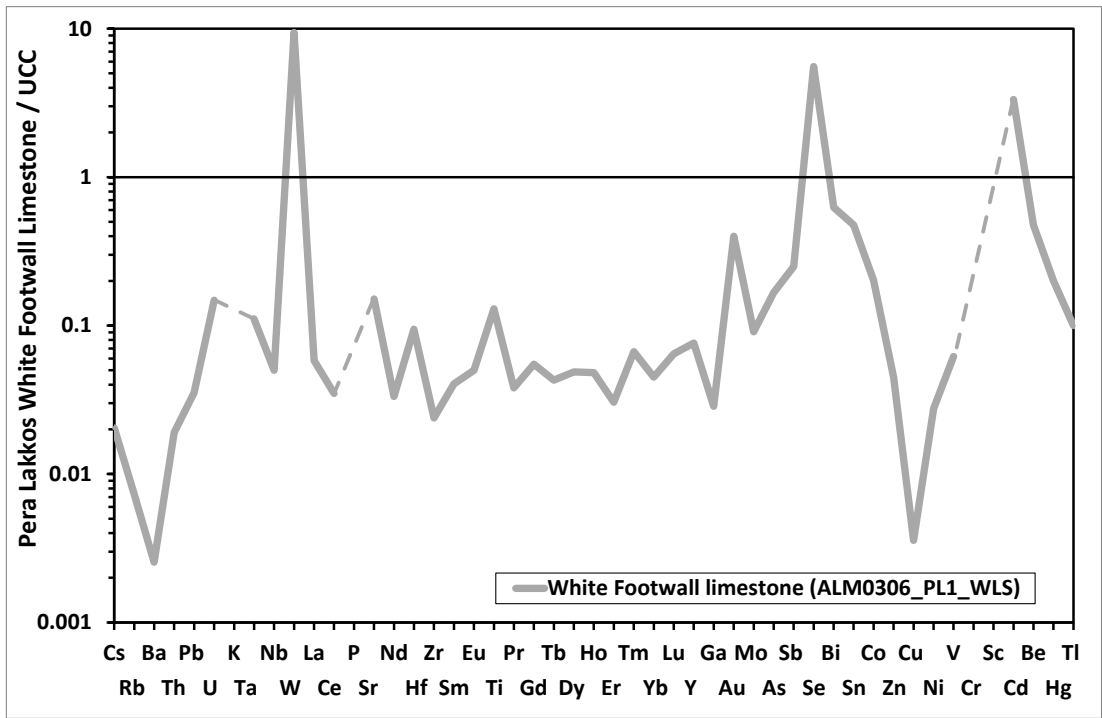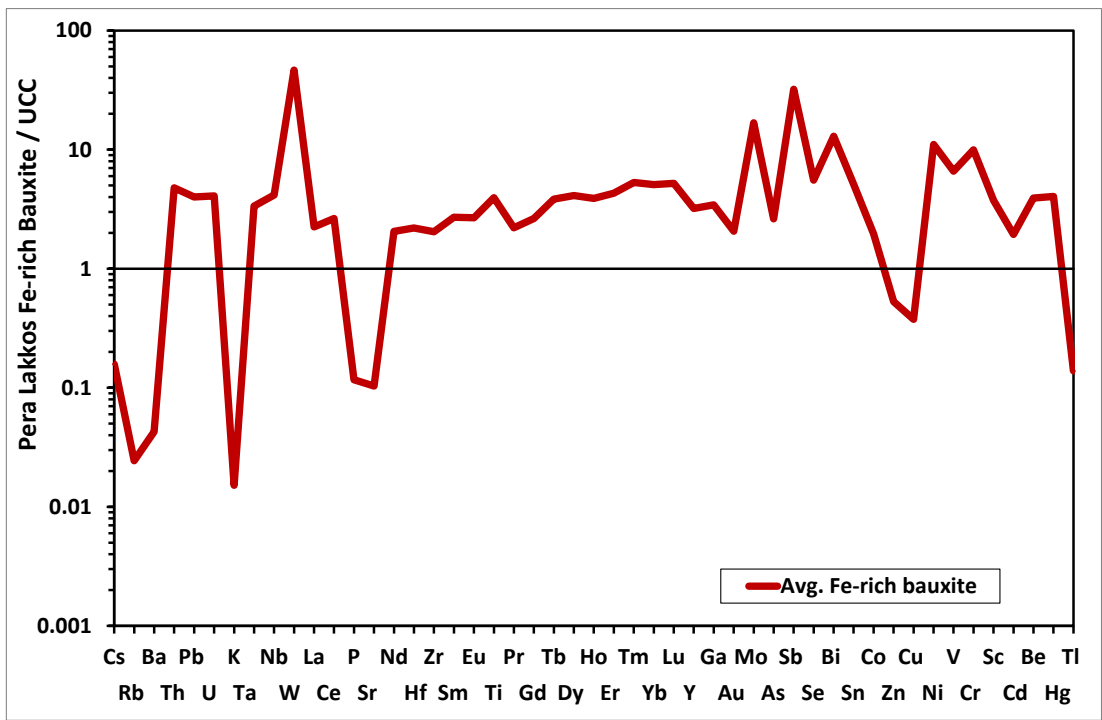
Figure S22: Detrital and authigenic crystalline phases separated, by CH$_3$COOH dissolution, from the white footwall limestones (ALM0306_PL1_WLS): chromite (left images); zircon (upper right); rutile (middle right); chromite with zircon and rutile crystal (lower right).
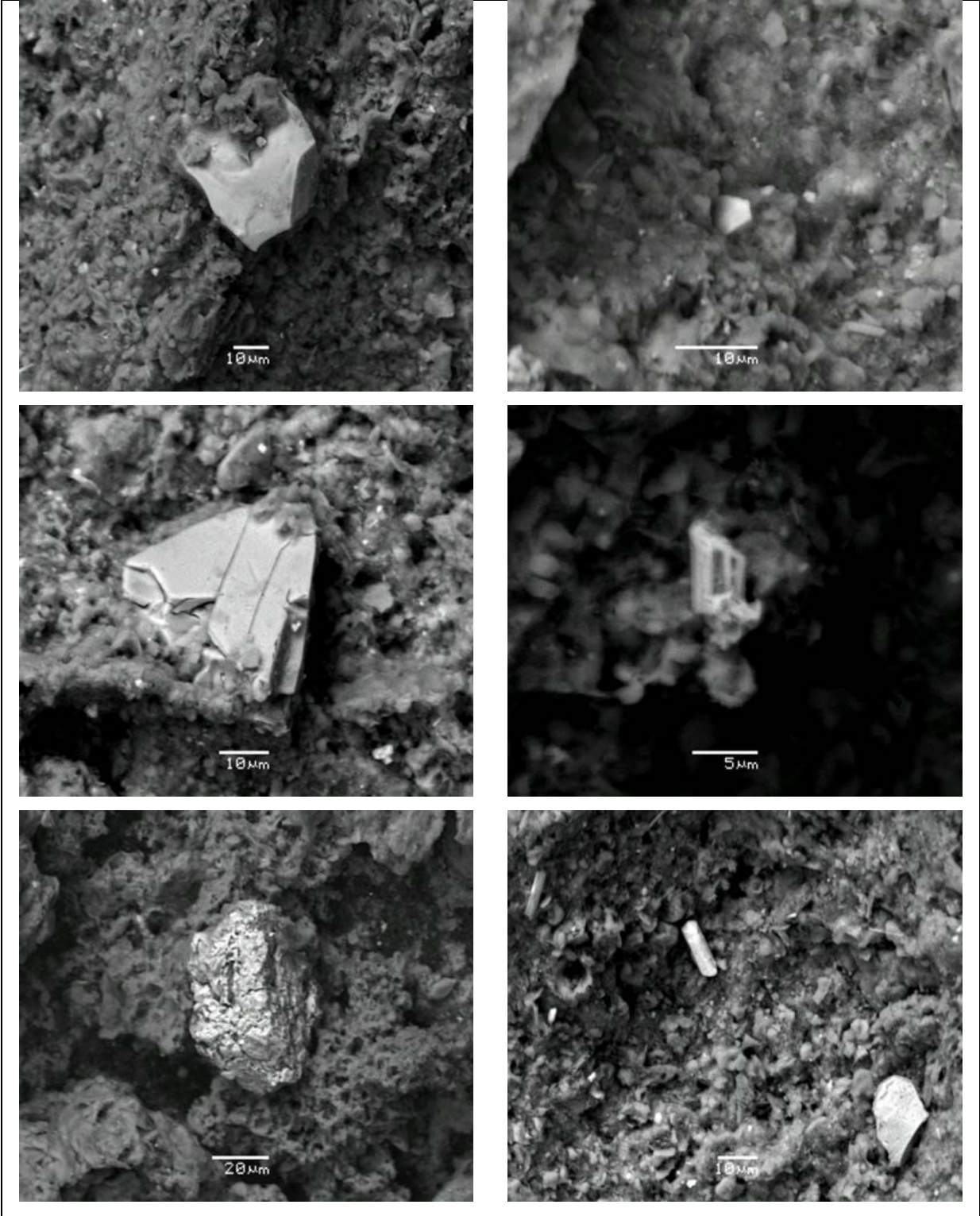
Figure S23: Detrital and authigenic crystalline phases separated, by CH₃COOH dissolution, from the dark hanging wall (ALM0306_PL1_DLS2): *Upper series images*: goethite (upper left image), its pseudomorph after pyrite (upper middle image), and pyrite (upper right image); *Middle series images*: magnetite crystals (middle left image), magnetite with framboids (middle image), and framboids (middle right image); *Lower series images*: chromite (lower left image); rutile (lower middle image); clays with REE (lower left image).
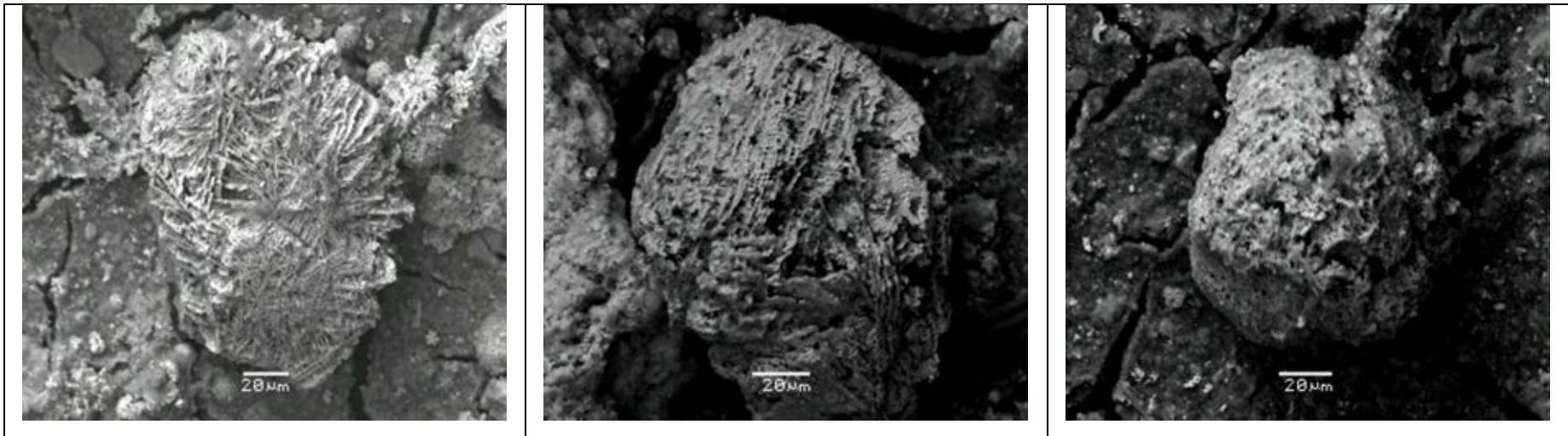
Figure 23: Continuing

Figure S24: The REE chondrite-normalized [10-17] diagrams for the studied dark (ALM0306_PL1_DLS2) and black (ALM0306_PL1_DLS1) hanging wall limestones, the coal layer (ALM0807_PL1_COAL) including its relevant flying ash (ALM0807_PL1_ASH), the Fe-rich/sulfide-bearing bauxite, the average of Fe-depleted bauxite (n=10), the average of Fe-rich bauxite (n=10), and the footwall limestone (ALM0306_PL1_WLS) at the mining front of Pera Lakkos underground mine.
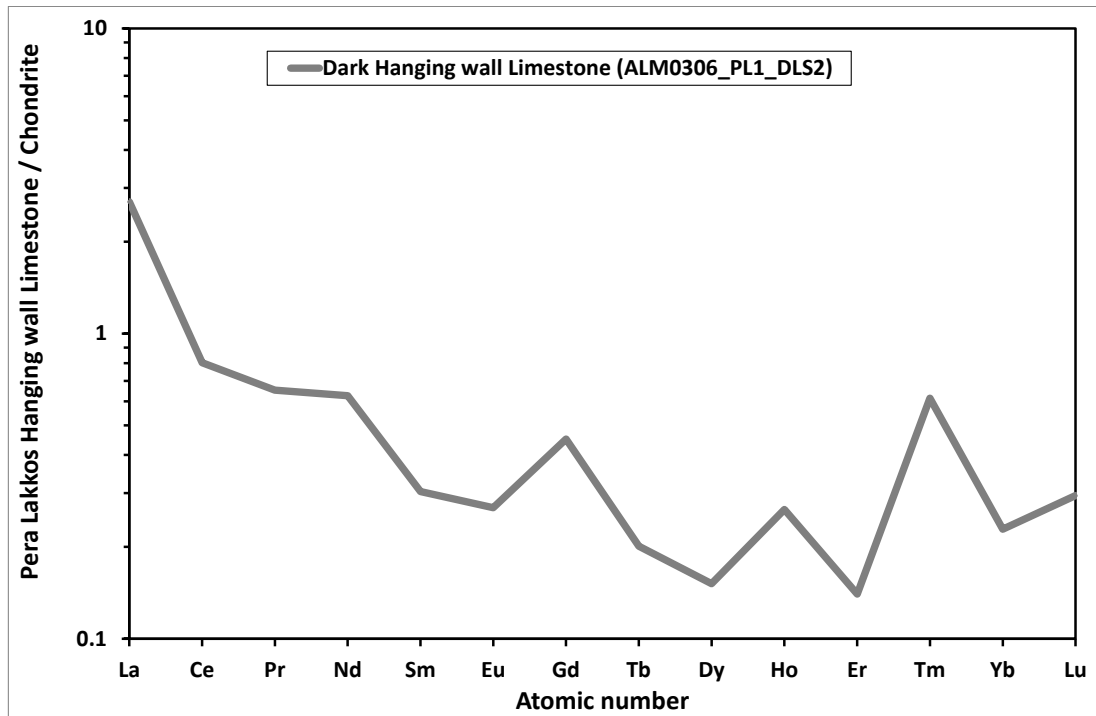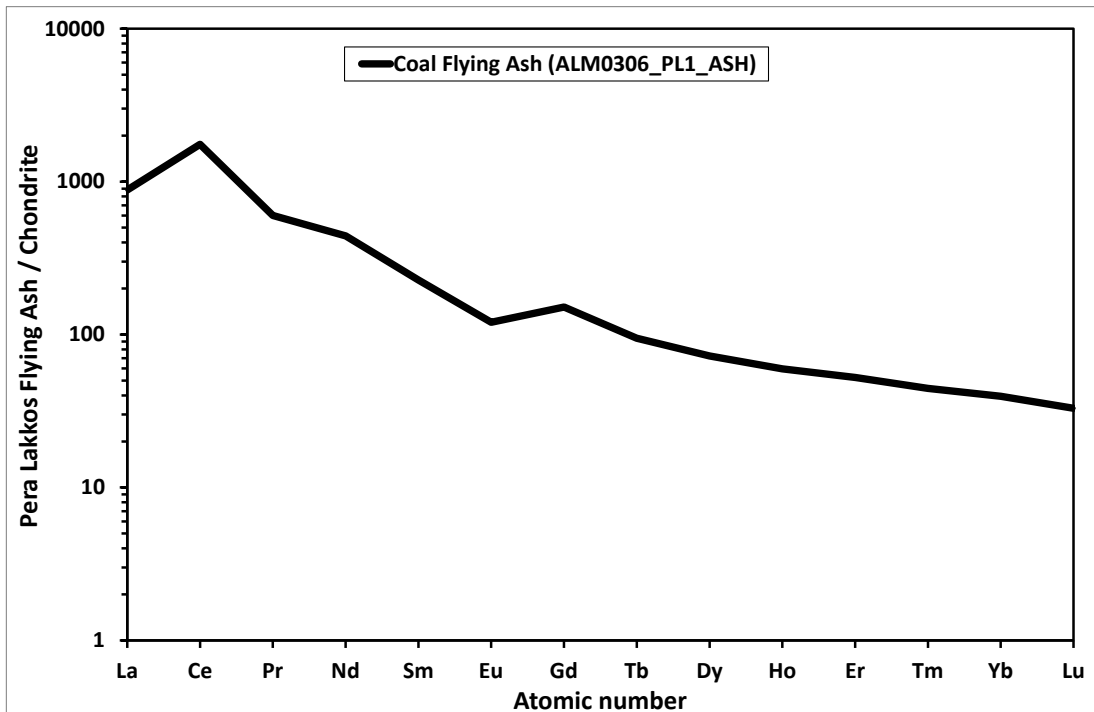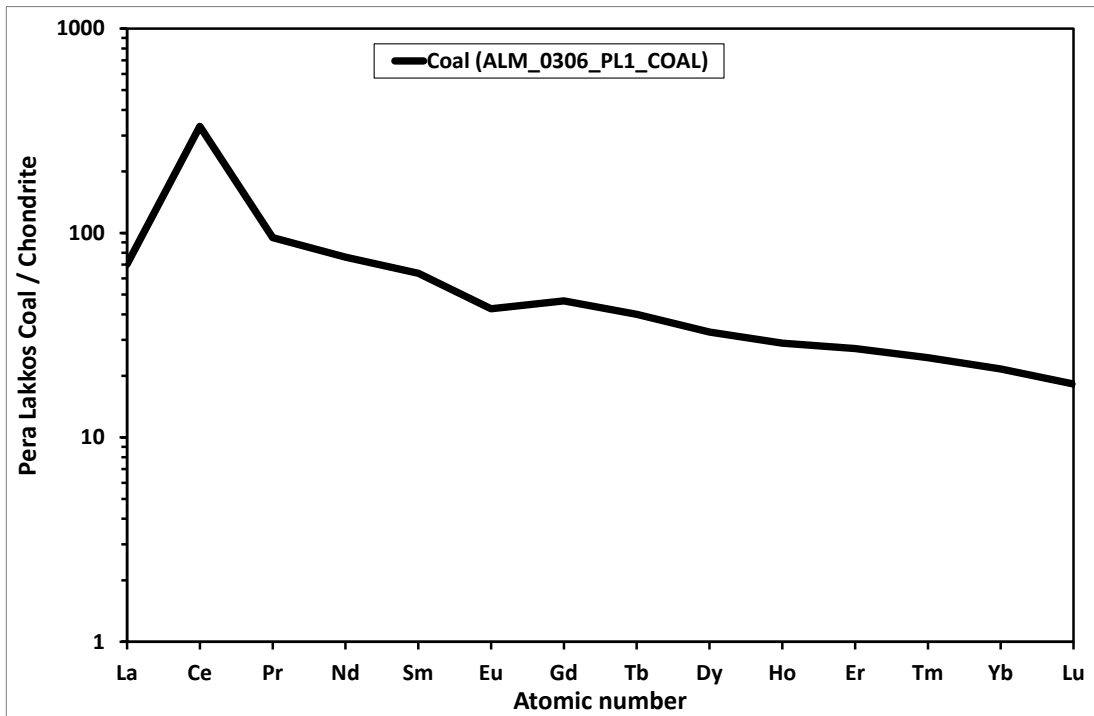
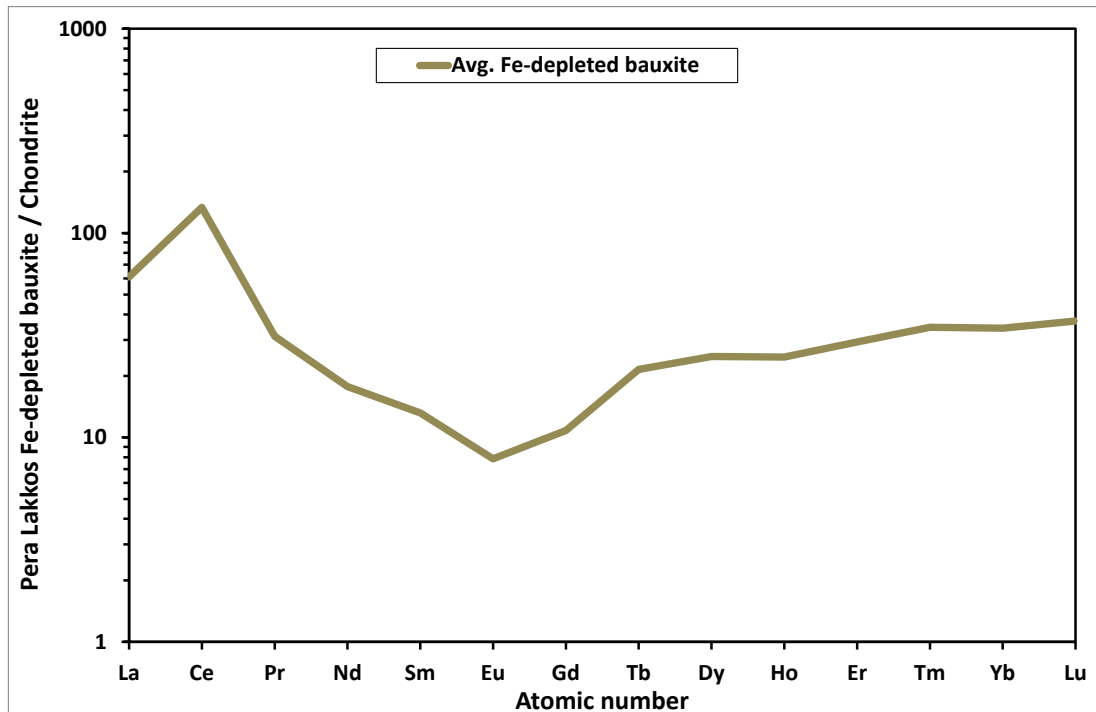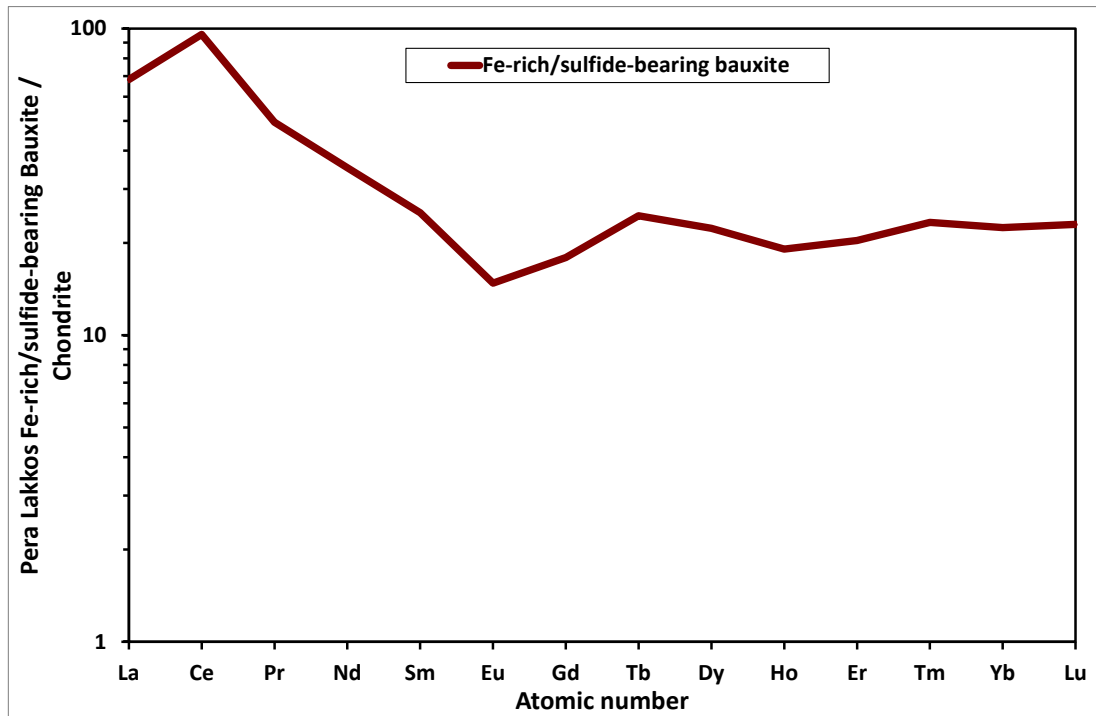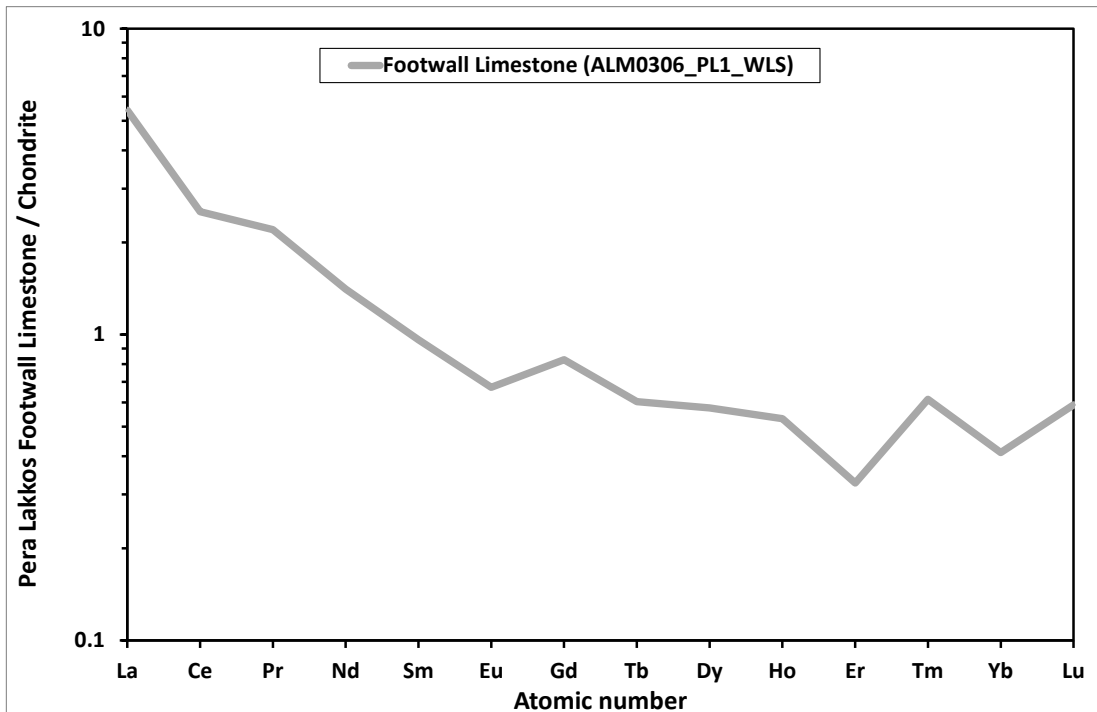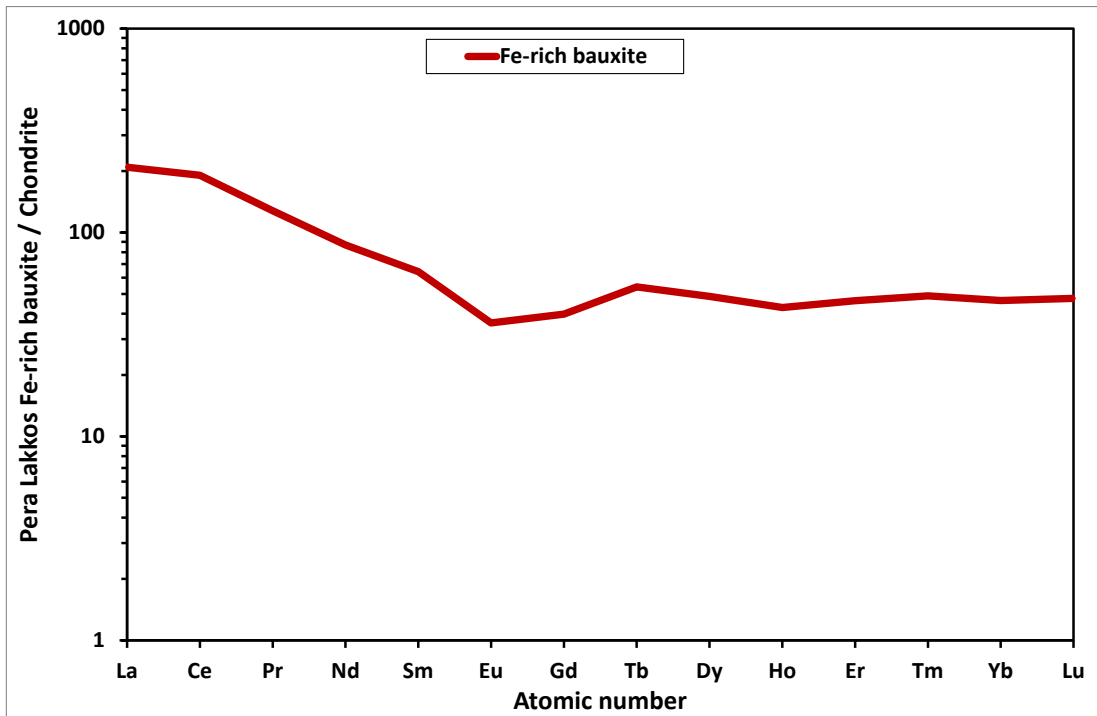**Figure 24:** Continuing

Figure 24: Continuing

Figure 24: Continuing

Supplementary References

1. Göttlicher J, Steininger R, Simon R (2006) Combination of micro X-ray techniques: the synchrotron radiation laboratory for environmental studies at ANKA. In: 12th European Conference on X-Ray Spectrometry (EXRS 2006), Paris, France, 19-23 June 2006, (abstr.).

2. Ravel B, Newville M (2005) ATHENA, ARTEMIS, HEPHAESTUS: data analysis for X-ray absorption spectroscopy using IFEFFIT. J Sync Rad 12: 537-541

3. Govindaraju K (1989) Compilation of working values and sample description for 272 geostandards. Geostandard Newslett 13: 1-113. doi:10.1111/j.1751-908X.1989.tb00476.x

4. Mariano AN, Mariano A Jr (2012) Rare earth mining and exploration in North America. Elements 8: 369-376.

5. Gambogi J (2013) Rare Earths; USGS Minerals Yearbook – 2011; U.S. Department of the Interior, U.S. Geological Survey: Washington, DC, 2013; pp 60.1-60.12.

6. Zepf V (2013) Rare earth elements: What and where they are. In Rare Earth Elements: A new approach to the nexus of supply, demand, and use: Exemplified along the use of Neodymium in permanent magnets; Zepf V, Ed.; Springer Theses; Springer-Verlag, Berlin-Heidelberg, Germany, pp. 11-39.

7. Liu X, Wang Q, Feng Y, Li Z, Cai S (2013) Genesis of the Guangou karstic bauxite deposit in western Henan, China. Ore Geol Rev 55: 162-185

8. German CR, Elderfield H (1990) Application of the Ce anomaly as a paleoredox indicator: The ground rules. Paleoceanography 5: 823-833

9. Mongelli G, Boni M, Buccione R, Sinisi R (2014) Geochemistry of the Apulian karst bauxites (southern Italy): Chemical fractionation and parental affinities. Ore Geol Rev 63: 9-21

10. Boynton WV (1985) Cosmochemistry of the rare earth elements: Meteorite studies, In: Rare earth element geochemistry, edited by Henderson P, Developments in Geochemistry 2, Elsevier, Amsterdam, pp. 115-152.

11. Haskin LA, Haskin MA, Frey FA, Wildman TR (1968a) Relative and absolute terrestrial abundances of the rare earths. In: Origin and distribution of the elements, edited by Ahrens, L.H., Pergamon, Oxford, vol. 1, pp. 889-911.

12. Haskin LA, Wildeman TR, Haskin MA (1968b) An accurate procedure for the determination of the rare earths by neutron activation. J Radioanal Chem 1: 337-348

13. Haskin LA, Helmke PA, Paster TP, Allen RO (1971) Rare earths in meteoritic, terrestrial, and lunar matter. In: Activation analysis in geochemistry and cosmochemistry, edited by Brunfelt A, Steinnes E, Proc. NATO Conf. on Activation Analysis in Geochemistry, Universitetsforlaget, Oslo, pp. 201-218.

14. Korotev RL (1996a) A self-consistent compilation of elemental concentration data for 93 geochemical reference samples. Geostandard Newslett 20: 217-245

15. Korotev RL (1996b) On the relationship between the Apollo 16 ancient regolith breccias and feldspathic fragmental breccias, and the composition of the prebasin crust in the Central Highlands of the Moon. Meteor Planet Sci 31: 403-412

16. Taylor SR, McClennan SM (1985) The continental crust: Its composition and evolution, Blackwell, Oxford, pp. 312.

17. Wakita H, Rey P, Schmitt RA (1971) Elemental abundances of major, minor, and trace elements in Apollo 11 lunar rocks, soil and core samples. Proceedings of the Apollo 11 Lunar Science Conference, pp. 1685-1717.

18. Gromet LP, Dymek RF, Haskin LA, Korotev RL (1984) The "North American shale composite": Its compilation, major and trace element characteristics. Geochim Cosmochim Acta 48: 2469-2482

19. Anders E, Grevesse N (1989) Abundances of the elements: Meteoritic and solar. Geochim Cosmochim Acta 53: 197-214

20. Rollinson H (1993) Using geochemical data; evaluation, presentation, interpretation. Pearson Education Limited, 352 pp. ISBN: 9-780582-067011.

21. Korotev RL (2010) "Rare Earth Plots" and the concentrations of rare earth elements (REE) in chondritic meteorites. Available online at: http://meteorites.wustl.edu/goodstuff/ree-chon.htm, accessed on: February, 2010.

22. Gamaletsos PN, Godelitsas A, Kasama T, Church NS, Douvalis AP, Göttlicher J, Steininger R, Boubnov A, Pontikes Y, Tzamos E, Bakas T, Filippidis A (2017) Nano-mineralogy and -geochemistry of high-grade diasporic karst-type bauxite from Parnassos-Ghiona mines, Greece. Ore Geol Rev 84: 228-244

23. Grice JD, Maisonneuve V, Leblanc M (2007) Natural and synthetic fluoride carbonates. Chem Rev 107: 114-132

24. Gamaletsos P, Godelitsas A, Mertzimekis TJ, Göttlicher J, Steininger R, Xanthos S, Berndt J, Klemme S, Kuzmin A, Bárdossy G (2011) Thorium partitioning in Greek industrial bauxite investigated by synchrotron radiation and laser-ablation techniques. Nucl Inst Methods Phys Res B 269: 3067-3073

25. Rudnick R, Gao S (2003) Composition of the continental crust. In Treatise on Geochemistry; Holland HD, Turekian KK Eds.; Elsevier - Pergamon: Oxford, 3, pp. 1-64.

26. Mongelli G, Boni M, Oggiano G, Mameli P, Sinisi R, Buccione R, Mondillo N (2017) Critical metals distribution in Tethyan karst bauxite: The cretaceous Italian ores. Ore Geol Rev 86: 526-536

27. Radusinović S, Jelenković R, Pačevski A, Simić V, Božović D, Holclajtner-Antunović I, Životić D (2017) Content and mode of occurrences of rare earth elements in the Zagrad karstic bauxite deposit (Nikšić area, Montenegro). Ore Geol Rev 80: 406-428

28. Özlü N (1983) Trace-element content of "karst bauxites" and their parent rocks in the Mediterranean belt. Miner Deposita 18: 469-476

29. Boni M, Rollinson G, Mondillo N, Balassone G, Santoro L (2013) Quantitative mineralogical characterization of karst bauxite deposits in the southern Apennines, Italy. Econ Geol 108: 813-833

30. Buccione R, Mongelli G, Sinisi R, Boni M (2016) Relationship between geometric parameters and compositional data: A new approach to karst bauxites exploration. J Geochem Explor 169: 192-201

31. MacLean WH, Bonavia FF, Sanna G (1997) Argillite debris converted to bauxite during karst weathering: evidence from immobile element geochemistry at the Olmedo Deposit, Sardinia. Mineral Deposita 32: 607-616

32. Mameli P, Mongelli G, Oggiano G, Dinelli E (2007) Geological, geochemical and mineralogical features of some bauxite deposits from Nurra (Western Sardinia, Italy): insights on conditions of formation and parental affinity. Int J Earth Sci (Geol Rundsch) 96: 887-902

33. Mondillo N, Balassone G, Boni M, Rollinson G (2011) Karst bauxites in the Campania Apennines (southern Italy): a new approach. Period Mineral 80 (3): 407-432

34. Mongelli G (1997) Ce-anomalies in the textural components of Upper Cretaceous karst bauxites from the Apulian carbonate platform (southern Italy). Chem Geol 140: 69-76

35. Mongelli G, Boni M, Buccione R, Sinisi R (2014) Geochemistry of the Apulian karst bauxites (southern Italy): Chemical fractionation and parental affinities. Ore Geol Rev 63: 9-21

36. Mongelli G, Buccione R, Sinisi P (2015) Genesis of autochthonous and allochthonous Apulian karst bauxites (Southern Italy): Climate constraints. Sediment Geol 325: 168-176

37. Mongelli G, Buccione R, Gueguen E, Langone A, Sinisi R (2016) Geochemistry of the apulian allochthonous karst bauxite, Southern Italy: Distribution of critical elements and constraints on Late Cretaceous Peri-Tethyan palaeogeography. Ore Geol Rev 77: 246-259

38. Putzolu F, Papa AP, Mondillo N, Boni M, Balassone G, Mormone A (2018) Geochemical Characterization of Bauxite Deposits from the Abruzzi Mining District (Italy). Minerals 8 (298): 1-24

39. Hanilçi N (2013) Geological and geochemical evolution of the Bolkardaği bauxite deposits, Karaman, Turkey: Transformation from shale to bauxite. J Geochem Explor 133: 118-137

40. Karadağ MM, Küpeli Ş, Arýk F, Ayhan A, Zedef V, Döyen A (2009) Rare earth element (REE) geochemistry and genetic implications of the Mortaş bauxite deposit (Seydişehir/Konya – southern Turkey). Chemie Erde 69: 143-159

41. Öztürk H, Hein JR, Hanilçi N (2002) Genesis of the Doğankuzu and Mortaş bauxite deposits, Taurides, Turkey: Separation of Al, Fe, and Mn and implications for passive margin metallogeny. Econ Geol 97: 1063-1077

42. Gromet LP, Dymek RF, Haskin LA, Korotev RL (1984) The "North American shale composite": Its compilation, major and trace element characteristics. Geochim Cosmochim Acta 48: 2469-2482

43. Haskin MA, Haskin LA (1966) Rare earths in European shales: a redetermination. Science 154: 507-509

44. McClennan SM (1989) Rare earth elements in sedimentary rocks: influence of provenance and sedimentary processes. In: Geochemistry and mineralogy of rare earth elements, edited by Lipin BR, McKay GA, Reviews in Mineralogy 21: 169-200

45. Kalaitzidis S, Siavalas G, Skarpelis N, Araujo CV, Christanis K (2010) Late Cretaceous coal overlying karstic bauxite deposits in the Parnassus-Ghiona unit, Central Greece: Coal characteristics and depositional environment. Int J Coal Geol 81: 211-226

46. Valeton I, Biermann M, Reche R, Rosenberg F (1987) Genesis of nickel laterites and bauxites in Greece during the Jurassic and the Cretaceous and their relation to ultrabasic rocks. Ore Geol Rev 2: 359-404